

## GAMMA ABOVE THE NEUTRON THRESHOLD EXPERIMENTS AT ELI-NP

F. CAMERA<sup>1,2</sup>, H. UTSUNOMIYA<sup>3,4</sup>, V. VARLAMOV<sup>5</sup>, D. FILIPESCU<sup>6,\*</sup>, V. BARAN<sup>7</sup>,  
A. BRACCO<sup>1,2</sup>, G. COLO<sup>1,2</sup>, I. GHEORGHE<sup>6,7</sup>, T. GLODARIU<sup>8</sup>, C. MATEI<sup>6</sup>, O. WIELAND<sup>1,2</sup>

<sup>1</sup>University of Milano, Department of Physics, Via Celoria 16, Milano 1-20133, Italy

<sup>2</sup>INFN section of Milano Via Celoria 16, Milano 20133, Italy

<sup>3</sup>Department of Physics, Konan University, Okamoto 8-9-1, Kobe 659-8501, Japan

<sup>4</sup>Center for Nuclear Study, University of Tokyo, 2-1 Hirosawa, Wako, Saitama 351-0198, Japan

<sup>5</sup>Lomonosov Moscow State University, Skobeltsyn Institute of Nuclear Physics, Leninskie gory, 1(2),  
119991, Moscow, Russia

<sup>6</sup>Extreme Light Infrastructure - Nuclear Physics (ELI-NP) / Horia Hulubei National Institute for R&D  
in Physics and Nuclear Engineering (IFIN-HH), Bucharest-Magurele, RO-077125, Romania

<sup>7</sup>University of Bucharest, Post Office Box MG-11, 077125 Bucharest-Magurele, Romania

<sup>8</sup>Horia Hulubei National Institute for R&D in Physics and Nuclear Engineering (IFIN-HH),  
Bucharest-Magurele, RO-077125, Romania

\*Corresponding author *Email*: dan.filipescu@eli-np.ro

*Abstract.* This Technical Design Report describes the physics cases and instrumentation proposed by the ELI-NP Working Group “Gamma Above Neutron Threshold” (hereafter ELIGANT). Extremely high-intensity and monochromatic  $\gamma$ -ray beams available at the ELI-NP allow us to enter a precision era of investigating electromagnetic responses of atomic nuclei. The ELIGANT group addresses the following 4 physics cases related to:  $p$ -process nucleosynthesis, Nuclear structure of Giant Dipole Resonance (GDR), New Compilation of total and partial photoneutron cross sections, Nuclear structure of Pygmy Dipole Resonance (PDR) and spin-flip Magnetic Dipole Resonance (MDR). For the  $p$ -process nucleosynthesis we measure photoneutron cross sections for rare isotopes (the  $p$ -process nuclei) near neutron threshold ( $S_n$ ). For nuclear structure of GDR by neutron decay, we measure  $(\gamma, xn)$  cross sections with  $x = 1-2$  for a new compilation of total and partial photoneutron cross sections to be pursued as a Coordinated Research Project (CRP) of the International Atomic Energy Agency (IAEA) and to measure exclusive neutron decays of GDR to the ground state and excited states in residual nuclei. For nuclear structure of GDR and PDR by gamma decay, we measure direct gamma decays of GDR to the ground state with branching ratios of the order of 1%. For nuclear structure of PDR and spin-flip MDR, we detect PDR and MDR in nuclei around neutron magic numbers with special emphasis on odd-N nuclei above  $S_n$  which is as low as 6 MeV. This will produce, together with data from nuclear resonance fluorescence (NRF) measurements, a complete study of the PDR and MDR. The TDRs of both “NRF” and “Gamma Above Neutron Threshold” will focus on PDR-MDR studies but in different energy range, nuclei and with different instrumentation. Both TDR will benefit from the synergic use of each other instrumentations.

*Key words:* Laser Compton scattered gamma-ray beams, photoneutron reactions, GDR, PDR, M1 spin-flip resonance.

## 1. INTRODUCTION

Photon-induced nuclear reactions with energies higher than the particle binding energy mainly excite collective states like the Isovector Giant Dipole Resonance (IVGDR or simply GDR) which was discovered in 1947 [1] as the strongest E1 response of nuclei representing an out-of-phase dipole oscillation between protons and neutrons. Such nuclear excited states decay by emission of particles or photons or alternatively is damped into a dense spectrum of more complex states toward a compound nucleus. The former process is characterized by the escape width, while the damping is characterized by the spreading width. The photon decay of GDR to the ground state and excited states provides information on the electromagnetic decay strength of GDR with multipole selectivity and the coupling of GDR to low-frequency collective modes. In addition to GDR built on the ground state, the strongest E1 response appears on excited states as well [2, 3].

The Lawrence Livermore National Laboratory (LLNL) and Saclay made major contributions to establishing the systematic of GDR built on the ground state through 1950s to 1980s, using the best  $\gamma$ -ray beam at the time produced by the positron annihilation in flight. The Atlas of photoneutron cross sections was published in 1988 [4] followed by the compilation IAEA-TECDOC-1178 published in 2000 as a Coordinated Research Project (CRP) of the International Atomic Energy Agency (IAEA) [5]. However, innovative analyses with the transitional multiplicity function have revealed large discrepancies in partial  $(\gamma, xn)$  cross sections between the Livermore and Saclay data that cannot be resolved in any systematic way [6]. Thus, there is a growing interest of constructing a new compilation of total and partial photoneutron cross sections as a CRP of IAEA [7].

The Pygmy Dipole Resonance (PDR) was discovered at the turn of the 21<sup>st</sup> century in the low-energy tail of GDR. The PDR which shows up in the energy region 6–12 MeV may represent a new collective excitation mode of a dipole oscillation of neutron-skin against a core nucleus [8]. Understanding the PDR is important to clarify the entire E1 response of nuclei. Besides, the PDR may be a good probe of the nuclear symmetry energy in the equation of state (EOS) for nuclear matter [9], which is of direct relevance to the formation of neutron stars in the type II supernova explosion.

Magnetic dipole resonance (MDR) of spin-flip type coexists with PDR around neutron threshold in the tail of GDR. MDR together with PDR constitute extra strengths of the low-energy  $\gamma$ -ray strength function (GSF) which is a nuclear statistical quantity common to  $(\gamma, n)$ ,  $(\gamma, \gamma)$  and  $(n, \gamma)$  reactions. Recently, the gamma-strength function method has been devised to indirectly determine radiative neutron capture cross sections for radioactive nuclei relevant to the *s*-process nucleosynthesis and nuclear transmutation [10,11]. In this regard, it is important to

provide MDR strength data above neutron threshold which is scarcer than PDR data.

There are 35 nuclides classified as the  $p$ -process nuclides ranging from  $^{74}\text{Se}$  to  $^{196}\text{Hg}$  that are produced by re-processing the pre-existing seed nuclei produced in the  $s$ - and  $r$ -processes, where photodisintegration plays a primary role [12]. As a natural result of this reprocessing, the  $p$ -process nuclides are neutron-deficient and rare in natural abundance typically less than 1% [13]. Measurements of  $(\gamma, n)$  cross sections for the  $p$ -process nuclei, known as the destruction cross section, have never been measured because of their rareness in natural abundance. Among the 35  $p$ -process nuclei, two odd-odd nuclei  $^{180}\text{Ta}$  and  $^{138}\text{La}$  draw highest attention. Obviously the measurement is feasible only with an extremely intense  $\gamma$ -ray beam.

Extremely intense and monochromatic  $\gamma$ -ray beams offered by the ELI-NP will open up a new era of experimental photonuclear reaction study. Physics cases addressed by the ELI-NP Working Group “Gamma Above Neutron Threshold” (ELIGANT) are listed in Table 1 along with *Day 1* experiments and the instrumentation.

In the  $p$ -process nucleosynthesis, we measure  $(\gamma, n)$  cross sections near neutron threshold for rare isotopes known as the  $p$ -process nuclei. Emphasis is placed on measurements for two odd-odd nuclei  $^{180}\text{Ta}$  and  $^{138}\text{La}$  as a *Day 1* experiment. Note the unique character of  $^{180}\text{Ta}$ , being the rarest nuclide and only naturally-occurring isomer. The physics case of nuclear structure of GDR is twofold, being related to *a*) exclusive gamma decays of GDR, and *b*) two step decay of GDR. A new compilation of total and partial photoneutron cross sections is recently proposed as CRP F41032 of IAEA [7]. Among many nuclei exhibiting serious discrepancies in  $(\gamma, xn)$  cross sections between the Livermore and Saclay data, emphasis is placed on  $^{159}\text{Tb}$  as a *Day 1* experiment. For nuclear structure of GDR by gamma decay, we measure gamma decays of GDR in nuclei with gamma branching ratios of approximately 1% among which emphasis is placed on  $^{208}\text{Pb}$  with a possible branching ratio 2% as a *Day 1* experiment. For nuclear structure of PDR and MDR, we detect PDR and MDR by exclusively measuring their neutron decays to the ground state and excited states in residual nuclei. Gamma tagging is needed to identify excited states populated in neutron and/or gamma decays of GDR, PDR and MDR. Measurements of exclusive neutron decays of GDR, PDR and MDR with gamma tagging are highly challenging and therefore follow *Day 1* experiments.

The four physics cases are described in detail in Section 2 (Physics Cases) indicated in the parenthesis in Table 1.

We propose two different detection systems, one (ELIGANT-TN) for Thermal Neutron measurements and the other (ELIGANT-GN) for Gamma and fast Neutron measurements (coincidence measurements are also foreseen). The detection system ELIGANT-TN is further classified into two different geometries

(using the same detectors), ELIGANT-TNH and ELIGANT-TNF representing High- and Flat-efficiency  $4\pi$  neutron detectors, respectively. The ELIGANT-GN consists of  $\text{LaBr}_3\text{:Ce}$  and  $\text{CeBr}_3$  scintillation detectors for detection of gamma rays and BC501A liquid and GS20  $^6\text{Li}$  glass scintillators for detection of neutrons. Both liquid and  $^6\text{Li}$  glass scintillators are necessary to detect high- and low-energy neutrons, respectively, at an energy boundary around 1 MeV. The energy range below 1 MeV is important because rich strengths of PDR and MDR are observed from neutron threshold up to the first excited states in residual nuclei in the measurement with the threshold neutron technique [14].

Table 1

List of physics cases addressed by the ELIGANT group. Given in the parenthesis is the section in which the corresponding subject of Physics Cases and Technical Proposal is presented.

Physics cases	<i>Day 1</i> experiments	Instrumentation
<i>p</i> -process nucleosynthesis	$^{180}\text{Ta}(\gamma, n)^{179}\text{Ta}$ $^{138}\text{La}(\gamma, n)^{137}\text{La}$	ELIGANT-TNH
Nuclear structure of GDR	$^{208}\text{Pb}(\gamma, \gamma_0)^{208}\text{Pb}$ : ground-state gamma decay of GDR in $^{208}\text{Pb}$ :	ELIGANT-GN
New compilation	$^{159}\text{Tb}(\gamma, xn)$ ( $x=1-2$ )	ELIGANT-TNF
Nuclear structure of PDR and MDR		ELIGANT-GN

The instrumentation is described in detail in Section 3 (Technical Proposal) indicated in the parenthesis in Table 1. We examine experimental feasibility for the ground-state gamma decay of GDR in  $^{208}\text{Pb}$  with a smallest branching ratio based on Monte Carlo simulations of physical- and background-event rates with the GEANT4 code [15] in Section 5 (Estimate of Count Rates).

We believe that the instrumentation proposed in the present TDR has a wide versatility of fulfilling experimental requirements for detection of gamma rays and neutrons by potential users of the ELI-NP facility.

## 2. PHYSICS CASES

### 2.1 *P*-process nucleosynthesis

The majority of nuclides heavier than iron are synthesized by the slow (*s*) and rapid (*r*) neutron captures with nearly equal (about 50%) shares of nucleosynthesis, which proceed along the line of  $\beta$ -stability and in the neutron-rich region of the chart of nuclei, respectively. On top of them, there are thirty-five

nuclei referred to as the  $p$ -nuclei with the proton number ranging from 34 (Se) to 80 (Hg) though five of them can also be produced to some extent by the  $s$ -process. All  $p$ -nuclei can be produced by the reprocessing the pre-existing seed nuclei of the  $s$ - and  $r$ -type by a combination of  $(p,\gamma)$  captures and  $(\gamma,n)$ ,  $(\gamma,p)$  or  $(\gamma,\alpha)$  photoreactions complemented by  $\beta^+$  decay, electron captures, and  $(n,\gamma)$  reactions. As a natural result of the re-processing, the  $p$ -process nuclides are neutron-deficient and rare in natural abundance (0.01 to 1 %, exceptionally of the order of 10% in the  $A\sim 90$  region).

Photodisintegrations play the leading role in the  $p$ -process, whereas the  $(p,\gamma)$  reactions appear to contribute only and probably marginally, to the production of the lightest  $p$ -nuclei. Temperatures larger than about  $T_9=1.5$  ( $T_9=T/10^9$  K, where  $T$  is the temperature in Kelvin) are required for photodisintegrations to take place on time scales comparable to stellar evolutionary ones, and may not exceed  $T_9=3.5$  in order to avoid the photoerosion of all the heavy nuclei to more stable nuclei in the “iron peak”. It is also necessary to freeze-out the photodisintegrations on a short enough time scale, typically of the order of one second. Those constraints are nicely met in the deep O-Ne layers of massive stars exploding as type II supernovae (SNe-II). The SNe-II is undoubtedly the most studied and the most successful scenario for the  $p$ -process [16,17,18]. Other plausible sites for the  $p$ -process, like pre-supernova burning phases of massive stars or the explosion of type-Ia supernovae, have been explored [12].

The significance of photonuclear reactions has revived in the context of the  $p$ -process nucleosynthesis, which was triggered and has been enhanced by the emergence of the laser Compton-scattering (LCS)  $\gamma$ -ray beam [13]. There are two facets of the production and destruction in photodisintegrations for the  $p$ -process nucleosynthesis. Photoneutron cross sections relevant to the production of the  $p$ -process nuclides can be measured with the LCS  $\gamma$ -ray beams at the existing facilities like HIGS [19] and NewSUBARU [20]. An important issue left in the future is the measurement of  $(\gamma,n)$  cross sections relevant to the destruction of the  $p$ -nuclides that are experimentally unknown. Since the natural abundance of the  $p$ -nuclides is small, the measurement requires  $\gamma$ -ray beams with intensity higher by three orders of magnitude than that available at the existing facilities, provided that typically 1 mg samples of  $p$ -nuclides are available commercially. Among the 35  $p$ -nuclei, especially two odd-odd  $p$ -nuclides,  $^{180}\text{Ta}$  and  $^{138}\text{La}$  await an experimental challenge to measurements of the  $^{180}\text{Ta}(\gamma,n)^{179}\text{Ta}$  and  $^{138}\text{La}(\gamma,n)^{137}\text{La}$  reactions [12,13].

Photoneutron cross section measurements for the  $p$ -process nucleosynthesis are carried out with a high-efficiency  $4\pi$  neutron detector which is proposed in Technical Proposal 3.2. Measurements of the  $^{180}\text{Ta}(\gamma,n)^{179}\text{Ta}$  and  $^{138}\text{La}(\gamma,n)^{137}\text{La}$  cross sections are a *Day 1* experiment.

The odd–odd nuclide  $^{180}\text{Ta}$  has the remarkable property of having a short-lived ( $T_{1/2} = 8.15$  h)  $J^\pi = 1^+$  ground state ( $^{180}\text{Ta}^g$ ) and a very long-lived ( $T_{1/2} > 1.2 \times 10^{15}$  yr)  $J^\pi = 9^-$  isomeric state ( $^{180}\text{Ta}^m$ ). As a result, only  $^{180}\text{Ta}^m$  is present in the solar system. Its minute abundance ( $^{180}\text{Ta}^m/^{181}\text{Ta} \approx 10^{-4}$ ) is enough to give it the status of the only naturally occurring isomer and the rarest element in nature. The study of the  $^{180}\text{Ta}^m$  production raises the specific problem of the possibility of thermalization of  $^{180}\text{Ta}^g$  and  $^{180}\text{Ta}^m$  in stars. This question is of substantial interest for evaluating the effective decay lifetime, and thus the probability of survival, of  $^{180}\text{Ta}$  in those conditions.

As in the case of nuclear reactions, it is obtained in thermal equilibrium conditions as a sum over the decay rates of the ground and excited states weighted with their Maxwell–Boltzmann populations. As a result, the  $^{180}\text{Ta}^m$  effective decay lifetime may be dramatically reduced in stars with respect to the value measured in the laboratory. The question of the stellar thermalization of  $^{180}\text{Ta}^g$  and  $^{180}\text{Ta}^m$  has been investigated many times over the years.

Besides the question of the thermalization, the predicted  $^{180}\text{Ta}^m$  yields suffer from nuclear uncertainties. Among them are the ones concerning the rates of the  $^{181}\text{Ta}(\gamma, n)^{180}\text{Ta}$  and  $^{180}\text{Ta}(\gamma, n)^{179}\text{Ta}$  photodisintegrations which most directly influence the  $^{180}\text{Ta}^m$  production and destruction.

The  $^{180}\text{Ta}(\gamma, n)^{179}\text{Ta}$  cross section cannot be estimated from experimental data using the reciprocity theorem, the radiative neutron capture cross section on the unstable  $^{179}\text{Ta}$  being unmeasured.

The  $^{181}\text{Ta}(\gamma, n)^{180}\text{Ta}$  reaction has been measured directly [21], the relative production by this reaction of the ground and isomeric states of  $^{180}\text{Ta}$  being obtained experimentally as well [22,23]. On the one hand, the  $^{180}\text{Ta}^m(n, \gamma)^{181}\text{Ta}$  cross section has been measured by [24]. This experimental information can enter the calculation of the rate of the reverse photodisintegration of direct interest through the application of the reciprocity theorem.

Of course, the stellar photodisintegration rate of  $^{181}\text{Ta}$  can differ significantly from the laboratory value due to the contribution of its thermally excited states. Even so, such measurements strongly constrain the nuclear input, and in particular the E1-strength function, and thus help reducing the uncertainties affecting the stellar rate predictions.

Therefore, the measurement of the rate of  $^{180}\text{Ta}(\gamma, n)^{179}\text{Ta}$  is a highly necessary complement to the already measured one on  $^{181}\text{Ta}$  in order to correctly predict the  $^{180}\text{Ta}^m$  yield.

The odd–odd neutron deficient heavy nuclides  $^{138}\text{La}$  and isomeric  $^{180}\text{Ta}^m$  are among the rarest solar system species. In spite of its very small abundance ( $^{138}\text{La}/^{139}\text{La}$  has a value of about  $10^{-3}$ ),  $^{138}\text{La}$  is underproduced in all  $p$ -process calculations performed so far. This results from an unfavorable balance between its main production by  $^{139}\text{La}(\gamma, n)^{138}\text{La}$  and its main destruction by  $^{138}\text{La}(\gamma, n)^{137}\text{La}$ , even in the  $p$ -process layers which are the most favorable to the  $^{138}\text{La}$  production.

These zones are the O-Ne layers of the considered massive stars explosively heated to peak temperatures around  $T_9=2.4$ . While the  $(\gamma,n)$  cross section has been measured for  $^{139}\text{La}$  [25], that for  $^{138}\text{La}$  has long been out of experimental reach. It is also noted that the two measurements of the  $\beta^-$  spectra of  $^{138}\text{La}$  suffer from a significant disagreement with the standard theory [26,27].

In view of the low  $^{138}\text{La}$  abundance, it has been attempted to explain its production by non-thermonuclear processes involving either stellar energetic particles [28,29] or neutral current neutrino-induced transmutations [30]. The former mechanism is predicted not to be efficient enough, except under ad-hoc assumptions, while the latter is found to be able to overproduce the solar  $^{138}\text{La}/^{139}\text{La}$  ratio by a factor of about 50 [30].

The thermonuclear inability to produce  $^{138}\text{La}$  in large enough quantities might result from inadequate nuclear physics inputs. A main source of uncertainty is given by fact that  $^{138}\text{La}$  yield predictions rely entirely on theoretical nuclear reaction rates. One is thus entitled to wonder about the sensitivity of the computed  $^{138}\text{La}$  underproduction to the nuclear uncertainties that affect the production and destruction channels.

The nuclear reaction input adopted for the  $p$ -process calculations concerning the  $^{138,139}\text{La}$  photodisintegration rates of direct relevance to the question of the production of  $^{138}\text{La}$  is represented by the reverse  $(n,\gamma)$  reaction rates. Using these values, the  $(\gamma,n)$  rates are evaluated by the application of the reciprocity theorem. More specifically, [31] examine the extent to which the rate of  $^{137}\text{La}(n,\gamma)^{138}\text{La}$  has to be decreased and the one of  $^{138}\text{La}(n,\gamma)^{139}\text{La}$  increased in order to bring the  $^{138}\text{La}$  overproduction at levels comparable with those of the neighboring  $p$ -nuclides.

A direct measurement of the photodisintegration of  $^{138}\text{La}$  would be highly valuable for the  $p$ -process calculations concerning the nucleo-synthesis of  $^{138}\text{La}$ . Due to the scarcity of  $^{138}\text{La}$ , the high intensity gamma beam provided by ELI-NP is the perfect tool to induce measurable  $(\gamma,n)$  on this isotope.

## 2.2 Nuclear structure of GDR

The study of the particle and gamma decay of the Giant Dipole Resonance and more generally of the electric dipole response from the region around the binding energy to the region of the centroid of the Giant Dipole Resonance is of major importance.

Giant Resonances (GR) are collective vibrations of the nucleus that are made up with the coherent contribution of many particle-hole (p-h) excitations and exhaust a large fraction of the corresponding sum rules. They can be classified depending on their multipolarity and their isovector or isoscalar nature. In a

macroscopic model the IsoVector Giant Dipole Resonance (IVGDR) is a dipole collective vibration of the neutrons against the protons. It substantially exhausts the nuclear photo-absorption cross section and it is the nuclear collective mode naturally excited with polarized monochromatic  $\gamma$ -ray beams such as those provided by ELI-NP. In fact, when high energy photons impinge on a nucleus, the protons feel the effect of an electromagnetic field that is oscillating in time but it is essentially uniform over the nuclear volume ( $\lambda = hc/E \approx 10^2 \text{fm} \gg$  nuclear radius) and thus they undergo oscillations with respect to the neutrons in the nuclear center-of-mass system. The neutron-proton interaction acts as the restoring force. Therefore, the GDR and other collective dipole states, if any, naturally bring information about the proton-neutron effective interaction and the asymmetry part of the nuclear equation of state.

One very important aspect of giant resonances rather poorly known is the properties of their particle and gamma decays. In fact, gamma decay measurements are extremely difficult as the nucleus has an excitation energy higher than the particle binding energy. Therefore high intensities and efficient detector systems are mandatory. The measurement of the neutron decay requires either an accurate measurement of the neutron kinetic energy or, alternatively, an extremely precise knowledge of the excitation energy of the nucleus. Also in this case an extremely intense beam with a very small bandwidth and an efficient detector system are mandatory.

The decay of the GDR is a spectacular example which shows how a well-ordered collective excitation dissolves into a disordered motion of internal degrees of freedom. The width of the resonance consists in two contributions: the one associated to the direct  $\gamma$  or particle emission from the initial  $1p-1h$  excitations expressed by an escape width  $\Gamma^\uparrow$  and the second is related to the coupling to the more complex  $2p-2h$ ,  $np-nh$  states leading to a spreading width  $\Gamma^\downarrow$  due to internal mixing. The internal mixing occurs through a hierarchy of couplings towards more and more complex degrees of freedom. The basic idea is that collective motion is preferentially damped by  $2p-2h$  components of the many-body wave function. Measuring particle and gamma-decay of the GDR could allow testing microscopic models in great detail. At present, the integral properties of this state (mean excitation energy, fraction of strength) can be reproduced within different frameworks; exclusive properties are expected to provide stringent and challenging tests for theories and lead to better understanding and improvements.

Exclusive measurements of the decay of giant resonances providing the values of the electromagnetic and particle decay widths are presently very few and much demanded. One of the main issues is whether we know with enough confidence the most appropriate effective interaction to be used in the isovector channel, e.g., in models like the Random Phase Approximation (RPA). For instance, in non-relativistic calculations based on the Skyrme effective interactions, the dipole spectrum is fragmented in several states. These states acquire a width if

the coupling with more complex 2 particle-2 hole (2p-2h) configurations is taken into account; however, a fine structure, already observed in the excitation (see Ref. [32,33,34,35,36]), remains. Such fine structure in excitation and their counterpart in decay are both important to be measured. Experiments such as the one performed using the Gran Raiden spectrometer in Osaka, where a beam of polarized protons of 200–400 MeV was focused on a  $^{208}\text{Pb}$  target [33], provide the excitation cross section of the GDR but do not give any information on the GDR decay to ground or high lying states through gamma or neutron emission.

The search for experimental evidence of scales associated with the coupling between collective states and internal and external degrees of freedom is a long-standing problem. Namely, the question whether or not the whole hierarchy of couplings (2p-2h, 3p-3h etc.) manifests itself by giving evidence of finer structures in the line shape as the experimental resolution increases, is not fully solved. The fine structure measurement of the giant resonances decay may carry relevant information on the dominant damping mechanism and coupling scale, through the comparison between GDR excitation cross section and the measurement of the GDR gamma decay direct to the ground state or low lying states.

Last but not least, the decay measurements are probably a unique way to understand the nature of the pygmy resonance that has been discussed above. At present, several experiments show the existence of such extra strength below the GDR region [37, 2] but they are not capable to pin down its microscopic structure. Theoretically, while some models predict only single-particle (that is, non-collective) excitations in that region, other models show the emergence of collective states that have, however, rather complicated structure (mixed isoscalar/isovector nature, possibly compressional and/or toroidal character). It may be expected that the decay measurements shed light on such questions. Tuning theories so that they are capable to reproduce the PDR features is important also for astrophysical reasons. The PDR plays also a role for the  $r$ -process nucleosynthesis (see for example Ref. [38,39]). Without some robust understanding it is hard to assess the reliability of theories that are employed to make simulations of the  $r$ -process based on some PDR systematic.

Theoretical calculations of the  $\gamma$ -decay of the GDR-PDR with the same formulation as in [40] are underway. The preliminary results for  $^{208}\text{Pb}$  predict for the ground state decay of the GDR a gamma decay width of approximately 40 keV. This theoretical value (using 4 MeV for the GDR total width) gives approximately 1% of gamma ground state decay branching ratio.

It is important to remember, however, that ELI-NP will permit the unique opportunity to scan the branching ratio in a large excitation energy window. If we get close to the particle binding energy we expect that the gamma decay width will become more important as compared to the neutron decay width and we envisage a microscopic calculation for the ratio of the gamma and neutron decay width.

### 2.2.1 Gamma decay of GDR in $^{208}\text{Pb}$

This experiment is focused to the measurement of the gamma decay to the ground state of the collective excited state Giant Dipole Resonance or Pygmy Dipole Resonance in  $^{208}\text{Pb}$ . The dipole response of this nucleus was widely studied theoretically and the excitation photo-absorption cross section was recently accurately measured in Osaka [33]. Only few data on gamma decay (for  $E^*$  larger than the particle binding energy) with large uncertainty on the excitation energy are available and will be used as a calibration [41]. These data provide a branching ratio in the energy interval 9.5–25 MeV of  $0.019 \pm 0.002$ .

We have classified this experiment a *Day 1* experiment as it can be considered, at the same time, a commissioning and a new experiment. It can be considered a commissioning experiment as some observables (as for example GDR excitation cross section) could be compared with the precise data already present in literature. The cross check with already measured data is a critical first step to identify possible systematic errors, in addition such check will support any new results. Indeed it can be considered a new experiment as it allows to measure, for the first time, the GDR decay to the ground state and to excited states as a function of excitation energy in the region around and above the particle binding energy.

The ELI-NP beam will excite the GDR-PDR on the target nuclei. The excitation energy is accurately known because of the unique small bandwidth provided by the beam (0.2% sigma).

The reaction mechanism is purely electromagnetic and we can easily assume that the main excited states are dipole states because of the  $0^+$  ground state. The excitation energy dependence of the branching ratio of the decay to the ground state and to low lying excited states is not known experimentally and this will be the first outcome of this experiment. It is also important to stress that the electric or magnetic type of the emitted radiation can be experimentally extracted because of the polarization of the ELI-NP beam and this provides, in very detail, the nature of the dipole excitation.

Some of the important outcome of the proposed experiment can be summarized as:

- 1) The experiment provides a clean measurement of the absolute value of GDR ground state  $\gamma$ -decay
- 2) As the ground state decay should scale as  $E^3$  times the  $B(E1)$  the experiment provides a measurements of the energy dependence of the  $B(E1)$
- 3) The measurement of both  $\sigma(\gamma,\gamma)$  (which is sensitive to the  $B(E1)$ ), and  $\sigma(\gamma,n)$  (which is sensitive to the wave function) is an important and challenging point for the theory.

Figure 1 shows in a schematic way the proposed experiment, namely the measurement of the branching ratio of the gamma decay in  $^{208}\text{Pb}$  to the ground state in an energy interval between 7 to 12 MeV.

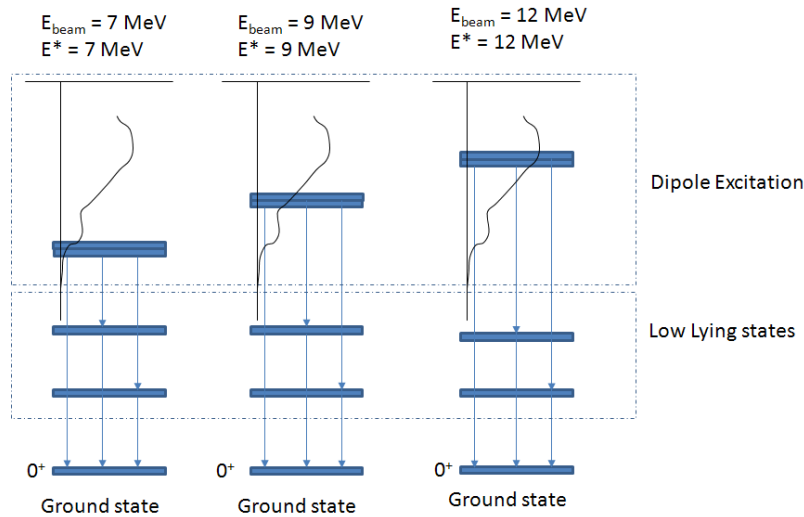


Fig. 1 - Scheme of the gamma decay of dipole excitations in  $^{208}\text{Pb}$  to the ground and excited states. For the excitation energy of about 12.5 MeV a branching ratio of about 1% is obtained for GDR by calculation (see text).

The highly disputed question on the collective character of the PDR can be solved in this mass region comparing the results of similar measurements in nearby stable nuclei as for example  $^{209}\text{Bi}$  and  $^{204}\text{Hg}$  (see Figure 2). In the case the PDR wave function extracted from the data-analysis is similar in all the three nuclei there is a very strong indication of the collective character of these states; alternatively there is a very strong indication on the fact that microscopically the PDR state has a strong dependence on the details of the nuclear structure. This provides evidence of the non-collective nature of the excited state. The comparison of the ground state branching ratio between  $^{208}\text{Pb}$  and  $^{207}\text{Pb}$  or  $^{209}\text{Bi}$  will provide a quantitative measurement on the role the hole ( $^{207}\text{Pb}$ ) or the proton ( $^{209}\text{Bi}$ ) have in the structure of the nucleus. Any experimental measurement for  $^{207}\text{Pb}$  and  $^{209}\text{Bi}$  which deviates from those of  $^{208}\text{Pb}$  is a clear indication of the fact that the proton or the hole cannot be considered simply as spectators, and can help to pin down for example the coupling of the particle or hole with the core vibrations.

An additional outcome of the experiment is the measurement of the two step gamma decay, namely, the decay of the PDR to a low lying excited state and

the subsequent decay of this state to the ground state (see a scheme in Figures 1 and 2). The feasibility of this measurement strongly depends on the gamma decay branching ratio and on the efficiency of the experimental array. Therefore one can expect to sum the data taken for several beam energies to increase statistics. This additional information (which will be already inside the dataset and therefore no dedicated experiment is necessary) will complete the reconstruction of the PDR wave function and can provide a strong selection on the effective forces used in theoretical calculations.

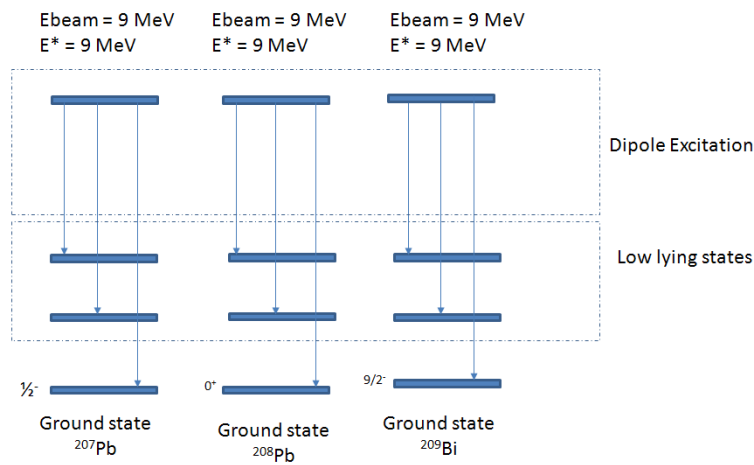


Fig. 2 - Scheme of the ground state decay for  $^{208}\text{Pb}$ ,  $^{207}\text{Pb}$  and  $^{209}\text{Bi}$ . The comparison of the branching ratio in the three nuclei can provide a solution of the highly disputed question on the collective character of the PDR.

It is important to stress again that all the now available measurements which provide high resolution information on the PDR-GDR at excitation energies higher than the particle binding energy are limited to excitation only. There are no high resolution measurements of the gamma decay from these states even though the fine structure of the dipole modes contains information on wavefunction structure, level densities [42] and on its characteristic scales [43] giving insight into their dominant damping mechanisms.

In the experiment we plan to measure, in steps of approximately 100 keV the energy interval starting from a little below the particle binding energy up to the maximum available ELI beam energy (7–12 MeV), the ground state decay of the GDR-PDR. A total of approximately 50 different beam energies are planned.

## 2.2.2 Neutron decay of GDR

Figure 3 depicts complex branchings of the neutron decay of GDR in a nucleus. The best monochromatic  $\gamma$ -ray beam of ELI-NP is featured with 0.2% energy resolution in  $1\sigma$  which is 0.5% in the full width at half maximum (FWHM). When GDR is excited below  $S_{2n}$  in the small energy bin (50 keV in FWHM at 10 MeV) by the monochromatic  $\gamma$ -ray beam, it undergoes neutron decays to the ground state and excited states in a residual nucleus in the  $1n$  channel. When the photoexcitation exceeds  $S_{2n}$ , decays of GDR become more complex leading to excited states as well as the ground state in either of the  $1n$  and  $2n$  channels.

Minute experimental data of such exclusive decays of GDR provide invaluable information on nuclear structure of GDR. Neutrons can be measured using liquid scintillation detectors with the time-of-flight (TOF) technique of measuring neutron kinetic energies with energy resolution of the order of 10%. However, it is not possible to pin down individual exclusive decays of GDR in heavy nuclei solely by neutron detection because of the limited energy resolution and dense level schemes of residual nuclei. Thus, to unambiguously identify all the branchings in the neutron decay of GDR requires neutron ( $n$ ) – gamma ( $\gamma$ ) or  $n$ - $\gamma$ - $\gamma$  coincidences with liquid and  ${}^6\text{Li}$  glass scintillation detectors for neutrons and  $\text{LaBr}_3:\text{Ce}$  detectors for gammas. We propose an array of liquid and  ${}^6\text{Li}$  glass scintillation detectors in Technical Proposal 3.4 and an array of  $\text{LaBr}_3:\text{Ce}$  and  $\text{CeBr}_3$  detectors in Technical Proposal 3.3.

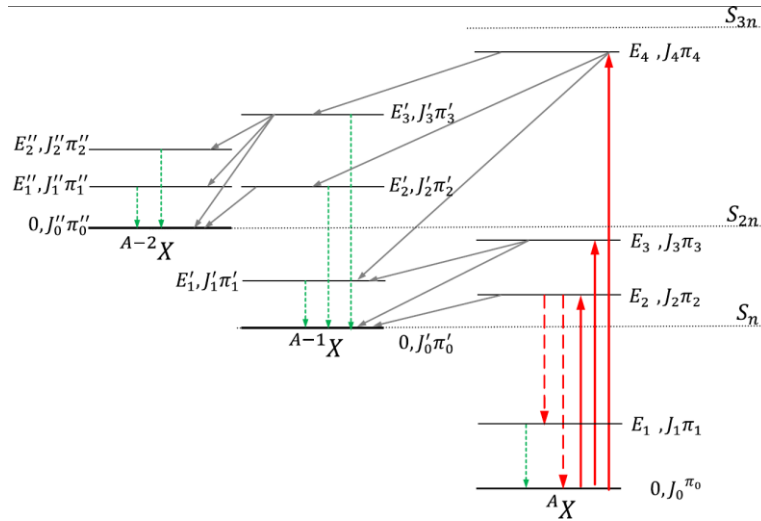


Fig. 3 - Complex neutron decays of GDR.

### 2.3 New compilation of total and partial Photoneutron cross sections for GDR

Reliable information on cross sections for total and partial photoneutron reactions is extensively used in basic and applied investigations. This information is required to study the relations between direct and statistical processes in the formation and decay of highly excited nuclear states and to determine the role of various components in the formation of the isospin splitting of GDR, the competition between various-type transitions forming the components of the configuration splitting of GDR, and so on. Moreover, data on cross sections for partial photoneutron reactions are widely used in various realms of science and technologies (nuclear physics and nuclear power engineering; radiation chemistry, geology, and medicine; materials science; ecology; and many other fields).

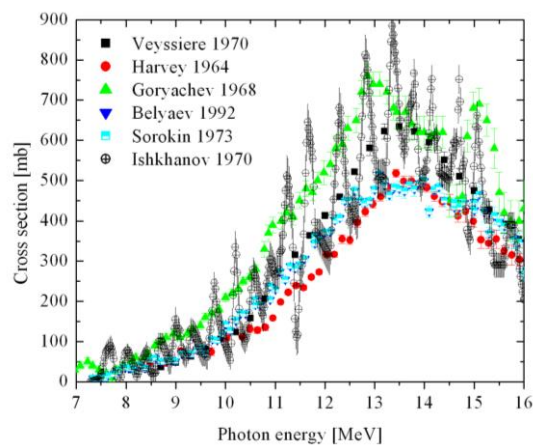


Fig. 4 - Experimental cross sections for the  $^{208}\text{Pb}(\gamma,Sn)$  reaction.

Many pieces of data were obtained using bremsstrahlung [44]. The directly measured quantity was the neutron yield cross section  $\sigma(\gamma,Sn) = \sigma[(\gamma,1n) + 2(\gamma,2n) + 3(\gamma,3n) + \dots]$ . The contribution of the single-neutron reaction cross section  $\sigma(\gamma,1n)$  was obtained using statistical theory and those of  $\sigma(\gamma,2n)$ ,  $\sigma(\gamma,3n)$  and of higher order, using corresponding procedures. It is clear now that such partial reaction have to be reinvestigated.

The majority of partial and total photoneutron cross sections were obtained using quasimonoenergetic photon beams produced in positron annihilation in flight at the two major facilities of the Lawrence Livermore National Laboratory (USA) and Centre d'Etudes Nucleaires de Saclay (France) during 1950s through 1980s toward a systematic understanding of the IVGDR [45]. The ATLAS of photoneutron cross sections was published for stable nuclei across the chart of

nuclides, giving integrated cross sections and the Lorentz parameters for the centroid energy and width [46,44].

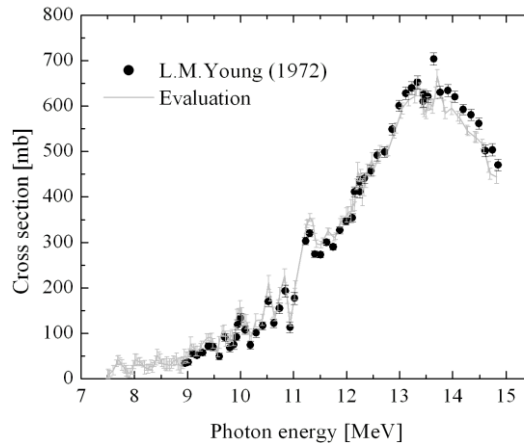


Fig. 5 - Evaluated cross sections for the  $^{208}\text{Pb}(\gamma,\text{Sn})$  reaction [47].

Both laboratories employed similar methods to identify reactions with different neutron multiplicities assuming that neutron spectra of  $(\gamma,1n)$  and  $(\gamma,2n)$  reactions are quite different. However the methods for determining neutron kinetic energy for neutron multiplicity sorting were different. As a result, large discrepancies (about 60%) in partial photoneutron reaction cross sections are well-recognized [48,49]: in many cases for the same nuclei the  $(\gamma,1n)$  reaction cross sections are noticeably larger at Saclay, but the  $(\gamma,2n)$  cross sections vice versa are larger at Livermore. Figures 4, 5 and 6 show typical discrepancies of photoneutron cross sections for  $^{208}\text{Pb}$  and  $^{181}\text{Ta}$  demonstrated in the IAEA-TECDOC [5]. Significant discrepancies are reported not only for these two nuclei but also for  $^{\text{nat}}\text{Rb}$ ,  $^{\text{nat}}\text{Sr}$ ,  $^{89}\text{Y}$ ,  $^{90}\text{Zr}$ ,  $^{93}\text{Nb}$ ,  $^{127}\text{I}$ , and  $^{197}\text{Au}$  by a factor of 0.80–0.93 [46]. Recent systematic measurements of  $(\gamma,n)$  cross sections for seven samarium isotopes and five neodymium isotopes show that overestimates of the Saclay data amounts to 20–37% for  $^{144,148,150}\text{Sm}$  [50] and 20–30% for  $^{143,144,145}\text{Nd}$  [51].

Many efforts were made to resolve those discrepancies with contradictory recommendations. It was clear that an objective criterion of investigating the reliability of experimental data is needed. After investigation of taking sums, differences, ratios of various cross sections such objective criterion was found out [52] as the transitional multiplicity function  $F_x = \sigma(\gamma, xn) / \sigma(\gamma, Sn)$  – the ratios of a partial reaction cross section  $\sigma(\gamma, xn)$  to the neutron yield cross section  $\sigma(\gamma, Sn) = \sigma[(\gamma, 1n) + (\gamma, 2n) + (\gamma, 3n) + \dots]$ .

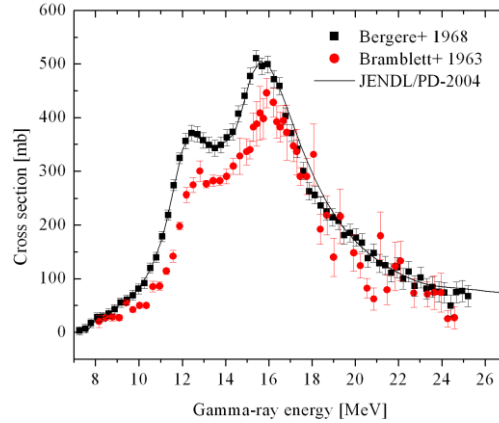


Fig. 6 - Experimental cross sections for the  $^{181}\text{Ta}(\gamma,\text{Sn})$  reaction in comparison with the JENDL/PD-2004 evaluation.

For example, according to the definition  $F_2$  cannot exceed 0.50 in magnitude under any conditions: its value above this absolute limit would mean a physically-incorrect determination of cross sections for both  $(\gamma,2n)$  and of  $(\gamma,1n)$  reactions. Physically unreliable values  $F_2$  greater than 0.50 (too large  $(\gamma,2n)$  reaction cross sections) correlate with unreliable (too small) values in the  $(\gamma,1n)$  reaction cross section. Correspondingly  $F_1$  should be smaller than 1.00. The absolute limit is 0.33 for  $F_3$ , 0.25 for  $F_4$ , 0.20 for  $F_5$ , 0.17 for  $F_6$ , 0.14 for  $F_7$  and so on. If these functions (ratios) exceed absolute limits mentioned above, that means that neutron multiplicity sorting was erroneous. Investigations of many ( $^{90,91,94}\text{Zr}$ ,  $^{115}\text{In}$ ,  $^{112,114,116,117,118,119,120,122,124}\text{Sn}$ ,  $^{159}\text{Tb}$ ,  $^{165}\text{Ho}$ ,  $^{181}\text{Ta}$ ,  $^{188,189,190,192}\text{Os}$ ,  $^{197}\text{Au}$  and  $^{208}\text{Pb}$ ) experimental data show that they do not satisfy the proposed criteria for data reliability.

A new method of evaluation that satisfies the introduced criterion was proposed based on the well-tested theoretical model of photonuclear reactions. The initial data are experimental neutron yield cross sections  $(\gamma,\text{Sn})$  and neutron multiplicity sorting is calculated in the model:  $\sigma^{eval}(\gamma, xn) = F_x^{theor} \times \sigma^{exp}(\gamma, \text{Sn})$ . That means that the competition of partial cross sections  $(\gamma,1n)$ ,  $(\gamma,2n)$  and  $(\gamma,3n)$  is in accordance with the model and the sum of evaluated partial cross sections –  $\sigma^{eval}(\gamma, \text{Sn}) = \sigma^{eval}(\gamma, 1n) + 2\sigma^{eval}(\gamma, 2n) + 3\sigma^{eval}(\gamma, 3n)$  – is equal to the experimental cross section  $\sigma^{exp}(\gamma, \text{Sn})$ .

Data evaluated by using such approach noticeably disagree with both the Saclay and Livermore data obtained by neutron multiplicity sorting, but agree with data obtained using an activation method of identifying final nuclei produced in partial reactions.

Moreover newly evaluated data noticeably disagree with the data evaluated in the frame of the IAEA Coordinated Research Project (CRP) on Compilation and Evaluation of Photonuclear Data for Applications [5] – 164 isotopes of 48 elements (from  $^2\text{H}$  to  $^{241}\text{Pu}$ ). Although the CRP played an important role in the fundamental research and applications of photonuclear reactions (systematics, evaluations, digital data library, etc.), the IAEA-TECDOC [5] has definitely shortcomings. Therefore re-measurements of partial (primarily,  $(\gamma,1n)$  and  $(\gamma,2n)$ ) photoneutron cross sections taking full advantage of gamma beams of the ELI-NP project is of great interest. Nuclei to be measured with the first priority are  $^{159}\text{Tb}$ ,  $^{181}\text{Ta}$ ,  $^{116}\text{Sn}$ ,  $^{208}\text{Pb}$ ,  $^{115}\text{In}$ , and  $^{91,94}\text{Zr}$ .

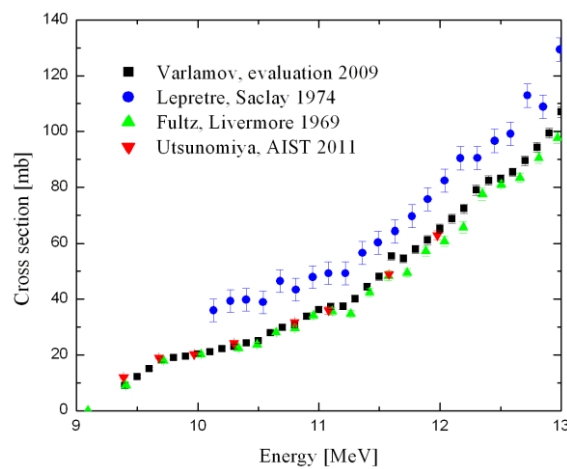


Fig. 7 - Comparison of the experimental data of single-photoneutron cross sections for  $^{118}\text{Sn}$  with the evaluation. The following symbols represent result of: V.V. Varlamov *et al.*, MSU SINP Preprint–3/847, 2009, Bull. Rus. Acad. Sci. 74, 833, 2010 (black squares), A. Lepretre *et al.*, Nucl.Phys. A219, 39, 1974, (blue dots), S.C. Fultz *et al.*, Phys.Rev. 186, 1255, 1969 (green triangles) and H. Utsunomiya *et al.*, Phys.Rev. C84, 055805, 2011 (red triangles). Evaluated data near  $S_n$  are in good agreement with the modern data obtained using laser Compton-backscattering  $\gamma$ -rays at AIST.

It is also important to point out that  $(\gamma,1n)$  cross sections below two-neutron threshold obtained in various experiments are not in good agreement. It was found out [6] that some persistent discrepancies exist among data obtained with different experimental methods or the same method at different laboratories; the reasons for that are different effective photon spectra used and additionally energy dependent systematic errors in the data calibration and normalization. It was shown that the total photoneutron reaction cross sections, which is equal to single-neutron reaction cross section below two-neutron threshold, obtained at Livermore

with the positron-annihilation  $\gamma$ -ray beam are generally smaller than those obtained at Saclay with the same kind of photon beam or with bremsstrahlung at various laboratories; disagreement amounts to factors of 1.06 – 1.25, depending on nuclei studied. According to our analysis, the best factor representing those disagreements would be 1.12. Therefore, measurements of  $(\gamma, 1n)$  cross sections are of great interest. Figure 7 compares evaluated single-photon neutron cross sections for  $^{118}\text{Sn}$  [53] with experimental cross sections obtained with the positron annihilation photon beam at Saclay [54] and Livermore [55] and the laser Compton scattered (LCS) photon beam at the National Institute for Advanced Industrial Science and Technology (AIST) [56]. One can see that the data taken with the LCS photon beam at AIST [56] are consistent with the evaluation. In contrast, the Saclay data are consistently larger than the evaluation, while the Livermore data are somewhat smaller than the evaluation at higher energies.

Gamma-ray beams are produced by laser Compton scattering in the ELI-NP project. Besides the brilliance, a great feature of the gamma beam offered by the ELI-NP project is the monochromaticity. The quasi-monoenergetic  $\gamma$ -ray beam produced at Livermore and Saclay was accompanied by the positron bremsstrahlung which could not be subtracted completely [57]. As a result, the cross sections are over-smoothed, where the energy resolution is noticeably worse than the width of positron-annihilation line. In contrast, it is noted that cross sections are obtained in bremsstrahlung experiments with finite energy resolution in the well-organized unfolding methods [5]. It is rather surprising that resonances attributable to pygmy or M1 resonances are often detected in single-neutron reaction cross section near threshold in bremsstrahlung experiments rather than quasimonoenergetic annihilation photon experiments. Therefore direct measurements of single-neutron cross sections near threshold with the monochromatic  $\gamma$ -ray beam of the ELI-NP are of great interest.

For the discrepancies between the Livermore and Saclay data which cannot be resolved in any systematic way [48,49], there is a growing interest in an improvement of the IAEA-TECDOC-1178 [5] based on such research activities as acquisition of new data and evaluation of the new data. We devote our experimental efforts to partial and total photon neutron cross section measurements for GDR. The maximum  $\gamma$ -ray energy is 19 MeV at ELI-NP so that the maximum neutron multiplicity is limited to 2. A novel technique of sorting the neutron multiplicity is required to address the serious discrepancy in  $(\gamma, 1n)$  and  $(\gamma, 2n)$  cross sections between the Livermore and Saclay data [48,49]. We have successfully developed a flat-efficiency neutron detector for neutron multiplicity sorting details of which are discussed in the Technical Proposal.

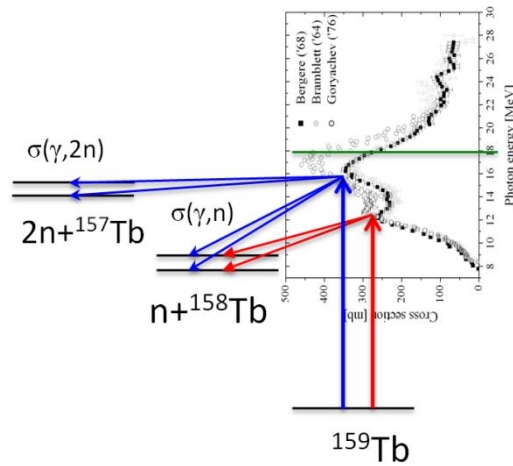


Fig. 8 - Partial photoneutron cross section measurements for  $^{159}\text{Tb}$ .

Currently, the new CRP F41032 "Updating the Photonuclear Data Library and generating a reference database for Photon Strength Functions" is being started at IAEA [7]. The new CRP will coordinate the efforts of experimentalists, theorists, and evaluators. It is very important to combine results of direct neutron multiplicity measurements carried out by using a flat-efficiency neutron detector with results of alternative activation experiments featured with a capability of separating multi-particle reactions with outgoing particles up to 6 – 7. The most promising experimental facilities which could contribute to a new CRP are the NewSUBARU (Japan) and Institute of Nuclear Physics of Moscow State University (Russia) and ELI-NP (Romania) which is currently under construction. Because of the outstanding parameters of the brilliant mono-energetic laser Compton-backscattering  $\gamma$ -ray beam, the ELI-NP will be a research center that provides experimental data for a new compilation.

Partial photoneutron cross section measurements for  $^{159}\text{Tb}$  shown in Figure 8 is a *Day 1* experiment.

## 2.4 Nuclear structure of Pygmy Dipole and M1 resonance

The electric dipole (E1) response of nuclei represents the most fundamental property of the finite many-body system. Giant dipole resonance (GDR) was discovered to be the strongest E1 response in 1947 [1], where nuclei undergo an out-of-phase dipole oscillation between protons and neutrons. The Lawrence Livermore National Laboratory and the Saclay, both of which had the

best  $\gamma$ -ray beam at the time produced by the positron annihilation in flight, took the initiatives in establishing the systematics of GDR through 1950s to 1980s [45]. The GDR study was one of the highlights in the research history of nuclear physics in the 20<sup>th</sup> century. Pygmy dipole resonance (PDR) was discovered in the 21<sup>st</sup> century in the low-energy tail region of GDR as a new excitation mode related to the dipole oscillation of a neutron skin against a core nucleus [8] though there may be a different interpretation like low-energy E1 strength that fails to participate in the GDR excitation. Besides the GDR, understanding the PDR is important to clarify the entire E1 response of nuclei.

M1 resonance of spin-flip nature also emerges near neutron threshold in the tail of GDR typically in nuclei with the shell gaps starting from the magic number larger or equal to 28. PDR and M1 resonance were reported in the nuclear resonance fluorescence [58, 35, 59, 60, 61, 62, 63, 64, 65], (p,p') reactions [66, 67, 68, 69, 70], ( $\gamma$ ,n) reactions [71, 72], Coulomb dissociation [37] and the ( $^3\text{He}$ ,  $^3\text{He}'\gamma$ ) reaction [73]. The extra E1 strength exhausts a small fraction of the Thomas-Reiche-Kuhn (TRK) sum rule, typically below 1% for the stable N=82 isotones [58], a few percent for  $^{117}\text{Sn}$  [73], 7(3)% for  $^{130}\text{Sn}$ , and 4(3)% for  $^{132}\text{Sn}$  [37].

The Brink hypothesis [74] linking photo-deexcitation process to photoabsorption tells that the  $\gamma$ -ray strength function of the low-energy tail of GDR governs the radiative neutron capture cross section. Since they constitute extra strength of the low energy tail of GDR, experimental information on the strength and resonance energy of PDR and M1 resonance is indispensable for a comprehensive understanding of the  $\gamma$ -ray strength function. Indeed, it is shown that the PDR increases reaction rates of photodisintegration in the *p*-process nucleosynthesis [21] and radiative neutron capture on nuclei along the line of  $\beta$ -stability in the *s*-process nucleosynthesis [75]. The increase of the neutron capture rate occurs even more drastically on neutron-rich nuclei in the *r*-process nucleosynthesis [38,39,76].

It is important to investigate the isoscalar and isovector nature of PDR from the point of view of nuclear structure. Recent investigations by ( $\alpha$ , $\alpha'\gamma$ ) reactions in comparison with those by ( $\gamma$ , $\gamma'$ ) reactions have shown that these two excitation modes of PDR are present in well-separated energy regions. From the comparison of ( $\alpha$ , $\alpha'\gamma$ ) cross sections for  $^{140}\text{Ce}$  [34] with B(E1) strength derived from ( $\gamma$ , $\gamma'$ ) reactions, one can see a strength over 5 – 7 MeV that is excited by both ( $\alpha$ , $\alpha'\gamma$ ) and ( $\gamma$ , $\gamma'$ ) reactions and a strength over 7 – 9 MeV that is excited only by ( $\gamma$ , $\gamma'$ ) reactions. According to the theoretical interpretation [77] based on the relativistic time blocking approximation [78] and quasi-particle phonon model [79], the low-energy strength is consistent with the isoscalar mode, while the high-energy strength with the isovector mode. Note that the isoscalar mode of PDR can be interpreted as neutron-skin oscillation, while the isovector mode of PDR is consistent with the picture of low-energy E1 strength that fails to participate in the

GDR excitation. Investigations by  $(\alpha, \alpha'\gamma)$  reactions are extended to  $^{138}\text{Ba}$  and  $^{124}\text{Sn}$ , showing similar excitation patterns of PDR [80,81].

Recently, inelastic proton scattering at intermediate energies has revealed PDR and M1 resonance in  $^{208}\text{Pb}$  [82] and  $^{90}\text{Zr}$  [36] and thus has drawn refreshed attention as a good probe of PDR and M1 resonance as well as GDR. In the  $(p, p')$  experiment, the E1 component is singled out as Coulomb excitation which dominates at very forward angles near  $0^\circ$ . In contrast, the determination of the M1 strength is rather indirect because it relies on the multipole-decomposition analysis of the proton angular distribution. Furthermore, the M1 excitation is induced strongly by nuclear interactions in the  $(p, p')$  reaction. Therefore, the M1 strength observed in the  $(p, p')$  reaction does not purely represent electromagnetic excitation strength. In this regard,  $\gamma$ -ray beams are obviously the best probe of investigating the electromagnetic property of nuclei.

The nuclear resonance fluorescence (NRF) is a good probe of both PDR and M1 resonance below neutron threshold [63]. The NRF experiment which is limited below neutron threshold naturally favors a choice of even-even nuclei because of high neutron threshold and the  $0^+$  nature of the ground state which simplify the data analysis though it is not limited to those nuclei. Although NRF experiments with  $\gamma$ -ray beams having nearly 100% linear polarization can separate resolved E1 and M1 resonances with peak structure, there remain some uncertainties in the determination unresolved components because of a model-dependence of the data analysis.

Experimental data of E1 and M1 resonances above neutron threshold are very scarce. Recently, an attempt was made of separating E1 and M1 photoexcitations above neutron threshold in  $^{207}\text{Pb}$  and  $^{208}\text{Pb}$  by measuring anisotropies of neutron emission to separate  $s$ - and  $p$ -wave neutrons with slow neutron detectors of long-counter type [83]. Although this measurement has successfully identified the total strength of PDR above neutron threshold, it lacked great energy resolution.

Nuclei around neutron magic numbers are important experimental objectives. One can find many cases for  $N = 50, 82, 126$  in the chart of nuclei. An example is of course  $^{208}\text{Pb}$  [82] or  $^{90}\text{Zr}$  [36] studied in  $(p, p')$  reactions. In addition, we can study PDR and M1 resonance in Zr and in Mo isotopes to see the development of their strengths as a function of neutron number. Furthermore, the Nd and Sm isotopes are interesting to investigate how PDR and M1 resonance develop with neutron numbers in deformed nuclei starting from  $N$ -magic ( $^{142}\text{Nd}$  and  $^{144}\text{Sm}$ ).

Special emphasis is placed on odd- $N$  nuclei with neutron thresholds as low as 6 MeV. Nearly full strengths of PDR and spin-flip M1 resonance are expected to emerge above neutron threshold for odd- $N$  nuclei. The present investigation of PDR and M1 resonance with emphasis on odd- $N$  nuclei above neutron threshold is

complementary to the investigation with the NRF technique with emphasis on even-even nuclei below neutron threshold.

Figure 9 depicts neutron decays of PDR and M1 resonance. The excitation energy of interest is expected not to exceed the two neutron separation energy ( $S_{2n}$ ). When photoexcitation does not exceed the first excited state in a residual nucleus ( $E_\gamma < S_n + E_x^{1st}$ ), neutron decay of DPR and M1 resonance takes place to the ground state as in the case of the threshold neutron experiment. However, when it exceeds, neutron decays to excited states can take place in competition with the ground state decay. From the point of view of the experimental technique, all possible neutron decays (and their branching ratios) may not be identified solely by neutron detection. Instead, they can be thoroughly investigated by neutron–gamma coincidences measurements.

We propose to detect neutron decays of PDR and spin-flip M1 resonance with  ${}^6\text{Li}$  glass scintillation detectors and liquid scintillation detectors. We use  $\text{LaBr}_3:\text{Ce}$  and  $\text{CeBr}_3$  detectors to detect  $\gamma$ -rays emitted following neutron decays. Neutron energies are determined with the time-of flight technique and neutron angular distributions are measured to identify E1 and M1 resonances. The  ${}^6\text{Li}$  glass scintillator is suited to detection of low-energy neutrons because of the large reaction Q-value (4.78 MeV) of the  ${}^6\text{Li}(n,\alpha){}^3\text{H}$  reaction, while the liquid scintillation detector with relatively low light output against recoil protons in the  $n + p$  scattering is suited to detection of high-energy neutrons. The energy boundary in the detection of neutrons with  ${}^6\text{Li}$  glass and liquid scintillation detectors is set around 1 MeV. Details of the neutron detection are discussed in the Technical Proposal.

The PDR and M1 resonance experiment above neutron threshold is very challenging and may not be considered as a *Day 1* experiment.

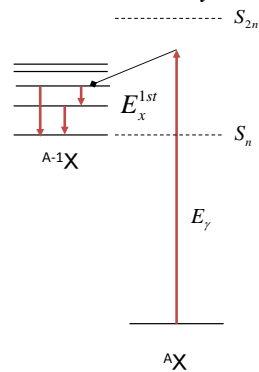


Fig. 9 - Excitation and neutron decays of PDR and M1 resonance.

### 3. TECHNICAL PROPOSAL

As already mentioned in Section 2, all the physics cases which are discussed in this TDR are related to the excitation of collective states at energy higher than the target particle binding energy. As the  $\gamma$  beam energy will be larger than 6 – 8 MeV, neutrons and high-energy  $\gamma$ -rays will be produced in every experiment and have to be measured.

The emitted neutrons can be detected either after a thermalization stage in polyethylene or directly arriving from the target (in this case their kinetic energy and angular distribution could also be measured). The measurement of the  $\gamma$  radiation, directly arriving from the target, requires a highly efficient and fast detector array. The multiplicity of the emitted gamma is in general expected to be one. In a small percentage of events the multiplicity could be two. The neutron multiplicity is no more than two because the maximum  $\gamma$ -ray energy available at ELI-NP is 19 MeV.

Two different detector setups are proposed and discussed in this TDR. The first is based on  $^3\text{He}$  tubes embedded in polyethylene for measurements of thermal neutrons (ELI-GANT-TN), the second is an array of scintillators for measurements of gamma rays and fast neutrons (ELI-GANT-GN).

Detection configurations optimum for the ELI-NP experimental conditions created by the LCS  $\gamma$ -ray beam time structure were investigated using a complex end-to-end simulation code developed using the GEANT4 toolkit for the simulation of the passage of particles through matter [85,15]. The simulation code is described in detail in Appendix B.

#### 3.1 General features of proposed detectors

In this TDR we will deal with four type of events (see Table 1), namely:

- 1) the  $\gamma$ -decay direct to the ground state;
- 2) two step  $\gamma$ -decay to the ground state;
- 3) neutron decay;
- 4) two step neutron +  $\gamma$ -decay to the ground state.

The aspects which need to be dealt in the design of the experimental apparatus concern:

- 1) the detection of high energy gamma rays;
- 2) the measurement of fast/thermal neutrons;
- 3) a design which is capable to eliminate/reduce in the best possible way the radiation ( $\gamma e^+, e^-$ ) which is produced in the target by the atomic electromagnetic interaction of the primary beam.

The atomic electromagnetic interaction of the primary beam in the target is a serious source of background which will be superimposed to the gamma decay from specific nuclear states of the target nuclei excited by the  $\gamma$ -rays of the beam. In addition, as the beam micro-bunches arrive every 16 nanoseconds for 32 times, the detector system must be able to uniquely identify the micro-shot which has generated the radiation, namely to measure and separate in each detector the events which arrives from different micro-bunch pulses.

In case it would not possible it is necessary to use only one micro-bunch every 10 ms with the consequent reduction of total beam intensity or, alternatively, one will have to treat the 32 micro-bunches as one single bunch in the estimation of the background contribution.

Table 2

The type of events which will be addressed in this TDR. In the first column an event type number is listed. In the second column the decay type is shown. In column 3 and 4 the probability to have that type of event (branching ratio) and the probability to measure that event with its entire energy deposition is listed. In the table  $\varepsilon_\gamma$  represents the absolute full energy peak efficiency of the  $\gamma$  detector system,  $\varepsilon_{th}$  and  $\varepsilon_n$  represent the detection efficiency for thermal and fast neutrons. The values of  $\varepsilon_\gamma$ ,  $\varepsilon_{th}$  and  $\varepsilon_n$  depend on the details of the detector setup.

	Decay Channels	Est. Branching ratio	Efficiency term	Comments
1	$\gamma$ decay to the G.S.	$10^{-2}$	$\varepsilon_\gamma$	
2	$\gamma'+\gamma''$ decay to the G.S.	$10^{-3}$	$\varepsilon_{\gamma'} \times \varepsilon_{\gamma''}$	
3	n decay	$\sim 1$	$\varepsilon_{th}$	Neutrons are thermalized
4	n decay	$\sim 1$	$\varepsilon_n$	
5	$n+\gamma'$ decay to the G.S.	$\sim 1$	$\varepsilon_n \times \varepsilon_{\gamma'}$	

### 3.1.1 Gamma ray measurements

As previously mentioned the  $\gamma$ -ray detectors must be fast, because of the ELI-NP beam time structure, and large enough to fully stop the shower produced by high-energy  $\gamma$ -rays. Long detectors are suited to stop Compton scattered high-energy  $\gamma$ -rays (the scattering is forward focused) while large detectors are more optimized to fully stop  $\gamma$ -rays which undergo pair production (one has to maximize the amount of sensitive material that the created 511 keV  $\gamma$ -rays must pass). Unfortunately, large and thick detectors are extremely expensive and compromises must be accepted.

We have performed GEANT4 simulations to calculate the full energy peak efficiency using detectors of different diameter and thicknesses. We have simulated LaBr<sub>3</sub>:Ce detectors, without any housing and absorbers, assumed to be placed at 25 cm from the target. The simulated trends, shown in Figure 10, will be in general valid for any type of detector; only absolute values will be different because of the different density and effective atomic number.

In the following plots we show the relative efficiency defined as the number of full energy peak events divided by the number of  $\gamma$  rays entering in the crystal. Using this observable one is almost independent from the solid angle subtended by the detector, namely from the distance detector-target.

It is obvious from the simulations that, for 10 MeV incident  $\gamma$ -rays, a diameter of 3" provides a relative efficiency which is almost twice than that a 2" crystal provides. This happens independently of the crystal thickness because, at 10 MeV, pair production dominates and therefore the crystal must be large enough to fully stop two 511 keV  $\gamma$ -rays.

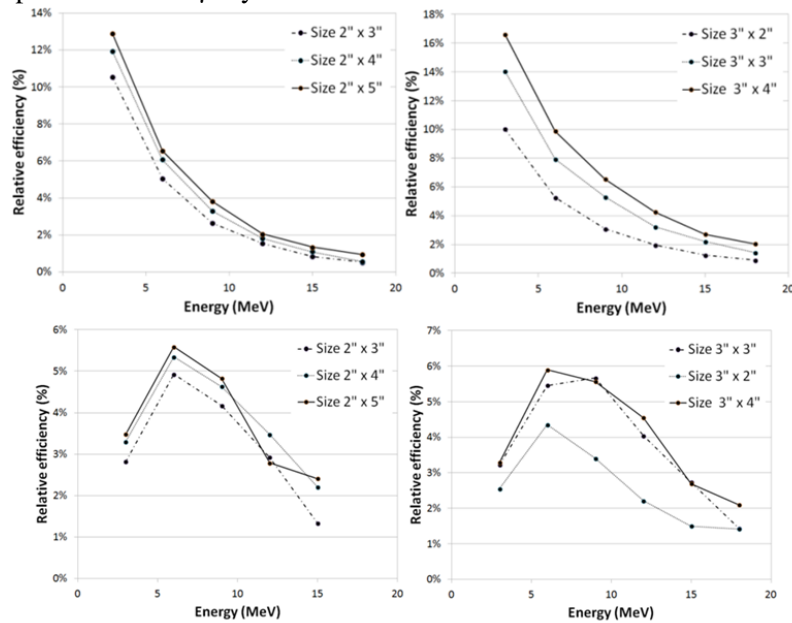


Fig. 10 – Upper plots: relative full energy peak efficiency simulated for a cylindrical LaBr<sub>3</sub>:Ce scintillator detector of different sizes. In the upper left panel the diameter is fixed at 2" (5.5 cm) while in the upper right panel the diameter is fixed at 3" (7.5 cm). Lower plots: relative first escape peak efficiency simulated for a cylindrical LaBr<sub>3</sub>:Ce scintillator detector of different sizes. In the lower left panel the detector diameter is fixed at 2" (5.5 cm) while in the lower right panel the diameter is fixed at 3" (7.5 cm).

In some situations, namely when one high energy  $\gamma$ -ray must be measured (i.e. event type 1 of Table 2, the PDR-GDR-MDR  $\gamma$ -decay to the ground state), also the events in the first escape peak can provide physical information. Figure 10 shows the first escape peak efficiency of the simulated detectors. In case of  $\gamma$ -rays with energy of 10 MeV, independently on the crystal size, the efficiency is similar. Only the  $3'' \times 2''$  LaBr<sub>3</sub>:Ce crystal shows a slightly worse efficiency.

As a general conclusion it is possible to say that the simulations shown here evidence that a cylindrical detector with a size of  $3'' \times 3''$  is expected to provide good performances in term of full and first escape peak efficiency.

As a second step it is necessary to select the crystal/detector material type which can provide the best performances in the measurement of high energy gamma rays inside the ELI-NP experimental setup. In this case the ELI-NP beam time properties will be the main factor for the choice of the detector type.

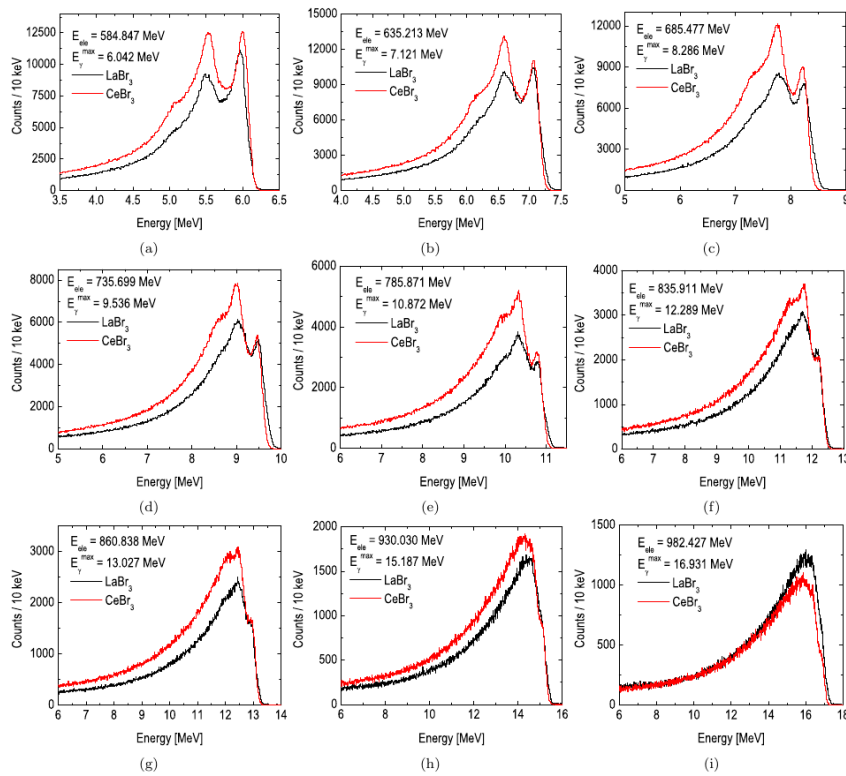


Fig. 11 - Laser Compton Scattered  $\gamma$ -ray beam spectra recorded with a  $3.5'' \times 4''$  LaBr<sub>3</sub> detector (black line) and with a  $3'' \times 3''$  CeBr<sub>3</sub> (red line). The detectors' response functions have been investigated using LCS  $\gamma$ -ray beams with maximum energies of: (a) 6.042 MeV, (b) 7.121 MeV, (c) 8.286 MeV, (d) 9.536 MeV, (e) 10.872 MeV, (f) 12.289 MeV, (g) 13.027 MeV, (h) 15.187 MeV and (i) 16.931 MeV.

A solid state large detector (HPGe) is the most natural and simple choice, particularly if one needs good energy resolution. In fact, energy resolution is excellent and a detector size of  $3'' \times 3''$  is available (although extremely expensive).

However, the choice of an array of HPGe detector is not the optimal one in connection with the beam structure. In fact, as the beam micro-bunches arrive every 16 nanoseconds for 32 times, a detector as HPGe cannot identify events from the different micro-bunches since HPGe signal line-shape depends on the interaction position of the  $\gamma$ -rays, it has a rather poor time resolution ( $\Delta T \sim 10$  ns) and a rise time of several hundred nanoseconds.

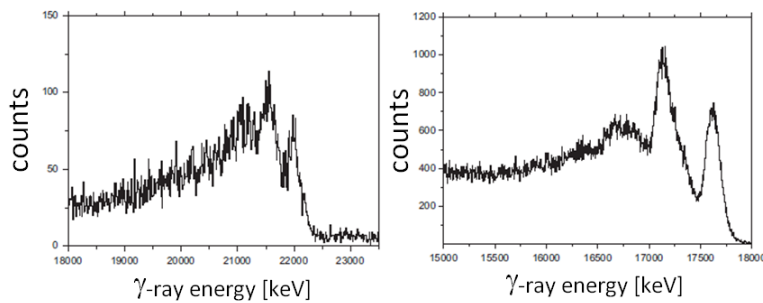


Fig. 12 - The energy spectrum measured at the ATOMKI Institute, with the S/N K628CS\_B LaBr<sub>3</sub>:Ce detector, the “LABRVD” active voltage divider and the analog electronics in case of 22.6 MeV (left panel) and 17.6 MeV (right panel) mono-chromatic  $\gamma$  rays.

The choice of HPGe implies in general that: either only one micro-bunch every 10 ns should be used (this means a reduction of the beam intensity of a factor of 32) or that no beam background radiation interacts in the detector for several hundreds of nanoseconds. This is because one background gamma ray in an HPGe detector will make it unusable for physics. Consequently, one has in both cases a drastic reduction of the count rate, in the first case because only part of the beam intensity has to be used, and in the second because a rather thin target has to be used to reduce the atomic electromagnetic background.

Except HPGe, no other large volume solid state detector type is available, the optimal choice therefore must shift on scintillators with good energy resolution and fast enough to separate events which arrive every 16 nanoseconds. In scintillators, the pulse line-shape does not change significantly with the position of the  $\gamma$ -ray interaction point and the signal rise time could be well below 50 ns.

Cerium doped Lanthanum Bromide (LaBr<sub>3</sub>:Ce) detectors are foreseen to be used for gamma ray detection in the multipurpose setup because of their good energy resolution, fast response and linear response with energy. The LaBr<sub>3</sub>:Ce material is an inorganic scintillator which presents excellent scintillation properties. It has an extremely high light yield (63 photons/keV), the best energy resolution

among scintillators (3% at 662 keV), excellent timing properties (500 ps of time resolution) and a high density (5.1 g/cm<sup>3</sup>).

But we are also interested in other types of detectors having the required working parameters. Such is the case of Cerium Bromide (CeBr<sub>3</sub>) scintillation detectors, which are known to have poorer energy resolution than the LaBr<sub>3</sub>:Ce ones, but considerably superior to other scintillation detectors such as NaI.

We report here on our comparative study between the working parameters of Cerium doped Lanthanum Bromide (LaBr<sub>3</sub>:Ce) and Cerium Bromide scintillation detectors investigated with quasimonochromatic  $\gamma$ -ray beams produced by the scattering of laser photons on relativistic electrons (LCS) at the synchrotron radiation facility NewSUBARU.

We investigated the energy resolution of two cylindrical scintillation detectors, a 3"×3" CeBr<sub>3</sub> detector from Scionix and a 3.5"×4" LaBr<sub>3</sub>:Ce detector, BrillLanCe380 89S102/3.5, Saint Gobain. High positive voltage was applied on the LaBr<sub>3</sub>:Ce (630 V) and on the CeBr<sub>3</sub> detector (555 V), the two voltage values being chosen to use the entire ADC input range for minimum gain on the amplifier. Both detectors had photomultiplier tubes dedicated to energy spectroscopy measurements. The LaBr<sub>3</sub>:Ce photomultiplier signal was sent to an Ortec preamplifier and NIM amplifier module (ORTEC 671) with 0.5  $\mu$ s shaping time. The amplifier signal was inserted into a 100 MHz 16 bit ADC digital MCA. The CeBr<sub>3</sub> detector had the TB-5 digital base from AMPTEK, containing a 14 pin photomultiplier base tube, a digital pulse processor with charge sensitive preamplifier and MCA and both (low and high voltage) power supplies.

We measured the energy spectra of LCS  $\gamma$ -ray beams for 9 energy values of the electron beam. Figure 11 shows the energy spectra recorded with both detectors for each LCS  $\gamma$ -ray beam having the maximum energy of: (a) 6.042 MeV, (b) 7.121 MeV, (c) 8.286 MeV, (d) 9.536 MeV, (e) 10.872 MeV, (f) 12.289 MeV, (g) 13.027 MeV, (h) 15.187 MeV and (i) 16.931 MeV. For each energy point we measured for the same amount of time both LCS  $\gamma$ -ray spectra and background synchrotron radiation spectra.

We can observe in the LCS  $\gamma$ -ray beam energy spectra shown in Figure 11 that the LaBr<sub>3</sub>:Ce detector has a higher full energy deposition probability than the CeBr<sub>3</sub> detector. The difference between detectors full energy peak - first escape peak ratio is because of the different crystal sizes. Also, the second escape peak is significantly higher in the CeBr<sub>3</sub> spectra because of the smaller crystal size.

The  $\gamma$ -ray beams are produced at NewSUBARU by the collision of a Nd:YVO<sub>4</sub> laser in the first harmonic and electron beams of highly precise energy. The NewSUBARU electron nominal beam energy resolution is of 0.04% and the uncertainty in the energy calibration over the energy range from 550 to 974 MeV is  $(5.5 - 9.4) \times 10^{-5}$ . Therefore the  $\gamma$ -ray beams have a precisely defined, sharp high energy front. After collimation, the  $\gamma$ -ray beam presents a low energy tail with an

small energy width of approximately 1.2 to 1.6% in FWHM values, depending on collimator thickness and aperture.

Therefore, the peak line shape is given by beam bandwidth, while the high energy front of the LCS  $\gamma$ -ray beam spectra is given entirely by the energy resolution of the detector and it is the main indicator of energy resolution differences between the  $\text{LaBr}_3\text{:Ce}$  and the  $\text{CeBr}_3$  detector. As can be seen in Figure 11, the LCS  $\gamma$ -ray beam high energy front measured with the  $\text{CeBr}_3$  detector is comparable the one recorded with the  $\text{LaBr}_3\text{:Ce}$  detector. Therefore, we have decided to use a mixed array of both  $\text{CeBr}_3$  and  $\text{LaBr}_3\text{:Ce}$  scintillation detectors.

The  $\text{LaBr}_3\text{:Ce}$  and  $\text{CeBr}_3$  (see Figure 12) are the only scintillators which are now capable to separate the first escape peak from the full energy up to gamma rays energy of 22 MeV. This feature is extremely important when the exact energy of the decay gamma radiation needs to be measured. In this case the possibility to clearly separate the first escape peak from the full energy peak almost doubles the efficiency of the detector system.

An important feature that the gamma part of the ELI-GANT-GN array should have concern the possibility to identify and separate the events coming from different micro-bunches. This capability will strongly increase the performances of the array and strongly enlarge the number of physics cases which can be addressed.

The plots in Figure 13 show, in a schematic way, two identical pulses of  $\text{LaBr}_3\text{:Ce}$  separated of 0, 16, 32, 48 ns. Namely, the plots show a  $\text{LaBr}_3\text{:Ce}$  anode signal when two events of identical amplitude (i.e. one from background and one from the decay of GDR-PDR-MDR) are generated in the same micropulse (0 ns delay) or in subsequent micro-bunches (16, 32, 48, 64 and 80 ns of delay). Even though two  $\gamma$ -rays from the same micro-bunch cannot be distinguished the fast rise-time of  $\text{LaBr}_3\text{:Ce}$  makes possible to distinguish and measure the radiation which will arrive in different micro-bunches.

A preliminary simulation has been performed to verify this capability for a  $\text{LaBr}_3\text{:Ce}$  detector. The basic assumptions for the simulation are:

- 1) The signal of the  $\text{LaBr}_3\text{:Ce}$  is the same independently of its amplitude and of the  $\gamma$ -ray's interaction point;
- 2) The electric pulse can arrive only every 16 ns for 32 times;
- 3) No more than  $K \approx 5$  gamma rays arrive in the detector within the micro-bunch;

Additionally, the results of the technique improve in case:

- 4) The background  $\gamma$ -ray events in general have energy below 1 MeV;
- 5) The signal  $\gamma$ -ray events in general have energy larger than 6 MeV.

The results of simulations lead therefore to a realistically achievable energy resolution for disentangling 6 MeV  $\gamma$ -rays having FWHM of the order of 1% which is the expected energy resolution of the scintillator.

In different laboratory there are already some pure or composite  $\text{LaBr}_3\text{:Ce}$  detector arrays. One is for example in Bucharest at IFIN and it is used for fast timing (using the centroid shift technique a sensitivity of about 50 ps has been

achieved). Its crystals however, to optimize time resolution, are small (1"×1" or 1"×1.5") and are not efficient enough for high energy gamma rays. The Darmstadt and Milano Universities have built arrays of large volume LaBr<sub>3</sub>:Ce and gained experience for their design and operation. One highly efficient array but not entirely of LaBr<sub>3</sub>:Ce which could be available in its first construction phase within 2–3 years is the PARIS array. The array consists of several clusters each composed by nine phoswich detectors. Each phoswich consists on a cubic 2"×2"×2" LaBr<sub>3</sub>:Ce optically coupled to a 2"×2"×6" NaI crystal. The light produced by the phoswich is read by one PMT.

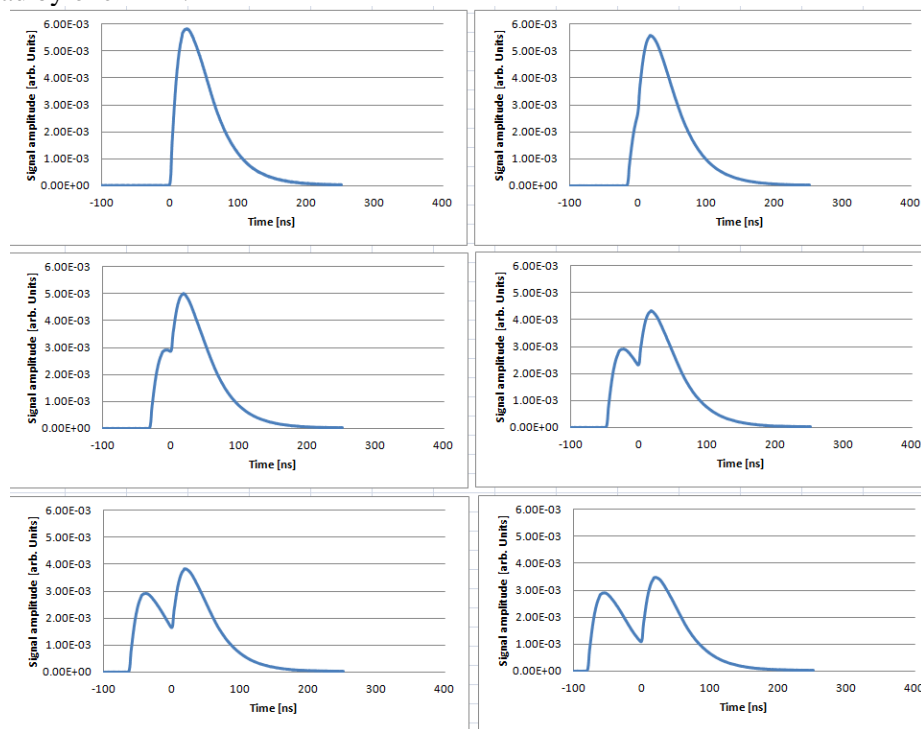


Fig. 13 - The anode LaBr<sub>3</sub>:Ce pulse in case of 'pile up' events. In the top-left panel it is shown the anode pulse when the two events are produced in the same micro-shot. The top-right panel shows the anode pulse when the two events are produced in two sequential micro-bunches (delay 16 ns). The center-left and center-right panels show the pulses when the delay between the events is 32 and 48 ns. The bottom-right and left panels shows the pulse when the events are delayed 64 and 80 ns. In these plots the events produce signals of identical amplitude.

Even though the efficiency of the array, in its final form, could be extremely high, this array could be useful only in some well-defined physics cases. The presence of NaI in the phoswich, with rise-time and time resolution intermediate between HPGe and LaBr<sub>3</sub>:Ce, makes the performances of PARIS not

optimal for a dedicated and permanently installed “all purpose” array at the ELI-NP facility. In this regard Table 3.1.2 lists the pro and cons for the use of such array. The following considerations have been taken into account in this connection.

- 1) LaBr<sub>3</sub>:Ce energy resolution at 662 keV, because of the phoswich geometry, is for PARIS of the order of 4.3 % while a standard cylindrical 3"x3" LaBr<sub>3</sub>:Ce has an energy resolution of 3%. This affects the capability to separate the first escape peak from the full energy peak.
- 2) NaI signal is very long in time and, on an event by event basis, the amount of energy shared between LaBr<sub>3</sub>:Ce and/or NaI could not be deduced. This means that the signal line-shape from the phoswich is not “a priori” known making very difficult if not impossible to separate and measure two pulses from two consecutive micro-bunches (namely separated by 16 ns).
- 3) The efficiency of PARIS clusters is based on the add-back technique. However, the cluster subtends quite a large solid angle. Therefore, the cluster could become blinded by background with very high probability.

The proposed *pulse identification and disentanglement* method is a straightforward application of the classical LMS (least mean squares) technique applied to identification of parameters within definite models of signals. Given assumptions 1) and 2), the experimental signal can be expressed as the linear superposition of  $K$  individual pulses of shape  $h(n)$  with unknown amplitude and arrival time.

In case assumption 2a) is verified, a maximum number of  $K=16$  (equivalent) pulses must be considered, whose arrival time is then a priori known (with  $N_0$  corresponding to 16 ns):

$$s(n) = \sum_{k=1}^{k=16} A_k \cdot h(n - k \cdot N_0) \quad (1)$$

This leads to the straightforward determination of a linear system that can be easily solved on-line by means of either DSP or FPGA (less than 100  $\mu$ s computation time).

In case assumption 2) is not verified, there is no more a strict limitation on the maximum number of superimposed individual pulses, so that a new assumption such as 3) must be verified in order to limit the computational load and allow for an on-line operation.

$$s(n) = \sum_{k=1}^{k=16} A_k \cdot h(n - k \cdot N) \quad (2)$$

In case assumption 3) is verified the computational effort is nonetheless considerably higher, because now two parameters (amplitude and arrival time) must be extracted for each individual pulse; moreover, the solution of the LMS problem doesn't lead anymore to linear systems and the solutions must be found

iteratively, largely increasing the computation time. However, by proper initialization of the LMS a non-linear estimator with a set of initial values for the unknown parameters (such as the average number of interactions) calculated on line by means of rough and fast techniques could still allow on-line operation, provided that the number of pulses to be taken into account is limited to e.g. 5.

This very simple identification technique, which is in principle applicable to signals coming from any kind of detectors, is particularly suited to LaBr<sub>3</sub>:Ce signals as they satisfy quite well assumption 1); moreover, being intrinsically fast in time (less than 80 ns) they are already partially time-resolved, which leads to the solution of a “better-posed” mathematical problem. On the contrary, slower signals, e.g. those of HPGe detector preamplifiers, apart from possibly not satisfying assumption 1), would be in any case much affected by a pile-up in time and thus the quality of the energy and time estimations would be definitely deteriorated.

Table 3  
Pro(+) and cons(-) for the use of a mixed array of 3"×3" LaBr<sub>3</sub>:Ce and CeBr<sub>3</sub> detectors or of the PARIS array.

	Mixed LaBr <sub>3</sub> :Ce and CeBr <sub>3</sub> 3"×3"array	PARIS array
Efficiency	+	++
Energy resolution	+++	+
Time resolution	++	++
Cost	-	++
Availability	++	-
Background Blinding	+	---
Pulse line-shape length	++	-
Background / event separation	+++	-
Complexity	+	-

### 3.1.2 Slow neutron measurements

#### 3.1.2.1 4π neutron detector consisting of <sup>3</sup>He proportional counters embedded in a polyethylene moderator

Detection of photoneutrons is of essential importance to investigate isovector giant dipole resonance (GDR) and other types of resonances. Photoneutron cross section measurements were carried out in 1950s through 1980s with neutron detectors based on the slowing down (“*thermalization*”) of neutrons followed by conversion reactions of neutrons into charged particles like protons and alpha particles etc. or neutron-capture γ rays. The slowing down of neutrons

occurs by  $n$ - $p$  scatterings in moderator materials like paraffin, polyethylene, or liquid scintillator. The conversion reaction can be  $^{10}\text{B}(n,\alpha)^7\text{Li}$ ,  $^6\text{Li}(n,\alpha)^3\text{H}$ ,  $^3\text{He}(n,p)^3\text{H}$ , or  $\text{Gd}(n,\gamma)$ . In the GDR study in the 20<sup>th</sup> century, the neutron detector of the former type consisting of  $\text{BF}_3$  proportional counters embedded in a paraffin moderator was used at the Lawrence Livermore National Laboratory (LLNL: USA) [86], while the one of the latter type, Gd-doped liquid scintillator was used at the Saclay (France) [87].

The cross section is the largest for the  $^3\text{He}(n,p)\text{T}$  reaction among the three charged-particle conversion reactions. The thermal neutron cross section for this reaction is 5330 barns, significantly higher than 3840 barns for the boron reaction, and its value also falls off with the  $1/v$  energy dependence. Therefore, a combination of high-pressure (10 atm)  $^3\text{He}$  proportional counters and high-density polyethylene moderator allows one to design a high-efficiency  $4\pi$  neutron detector. In contrast, in addition to the disadvantage in cross section, the  $\text{BF}_3$  proportional counter is not in popular use due to the fact that it can be operated at low gas pressure as well as the handling of poison  $\text{BF}_3$  gas.

Neutrons are detected at the peak energy corresponding to the reaction Q-value of the conversion reaction, which is 0.764 MeV in the  $^3\text{He}(n,p)\text{T}$  reaction, and at the continuum energy corresponding to the so-called wall effect. Note that the kinetic energy of “thermalized neutrons” is negligible when compared to the reaction Q-value. The continuum emerges because a proton or a tritium fails to deposit its full energies by hitting the counter wall before making complete stops. Thus, the continuum consists of a sum of two step-functions with threshold energies corresponding to the kinetic energies of  $^3\text{H}$  (0.191 MeV) and proton (0.573 MeV). Regardless of the wall effect, the minimum detection energy (0.191 MeV) of neutrons is, in general, sufficiently large compared to background  $\gamma$ -ray energies. As a result, the detector of Livermore type is also featured with excellent  $n$ - $\gamma$  separation capability.

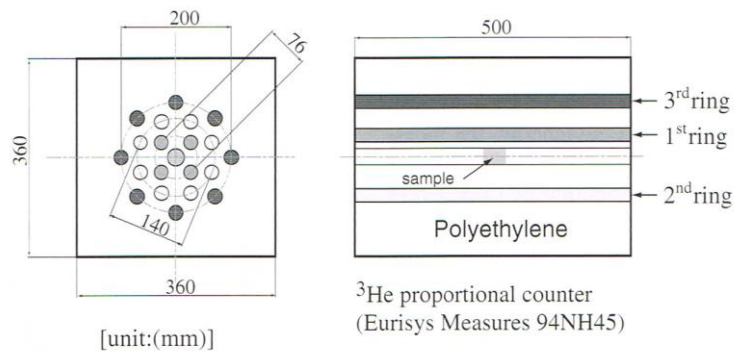


Fig. 14 -  $4\pi$  triple-ring neutron detector.

Figure 14 shows the high-efficiency  $4\pi$  neutron detector developed at the Konan University. The detector consists of 20  $^3\text{He}$  proportional counters in the configuration of three concentric rings, the inner Ring1 of 4  $^3\text{He}$  counters, the middle Ring2 of 8  $^3\text{He}$  counters, and the outer Ring3 of 8  $^3\text{He}$  counters, embedded in a polyethylene moderator. The moderator cube is fully surrounded by extra 5cm polyethylene plates with Cd sheets. The neutron detection efficiency is shown in Figure 15, where the efficiencies of Ring1, Ring2, and Ring3 as well as the total efficiency are given. The efficiencies were measured with a calibrated  $^{252}\text{Cf}$  source at the National Metrology Institute of Japan. A recent re-measurement at the same institute has assured the robustness of the detector with no degradation of the detection efficiency over the past 8 years.

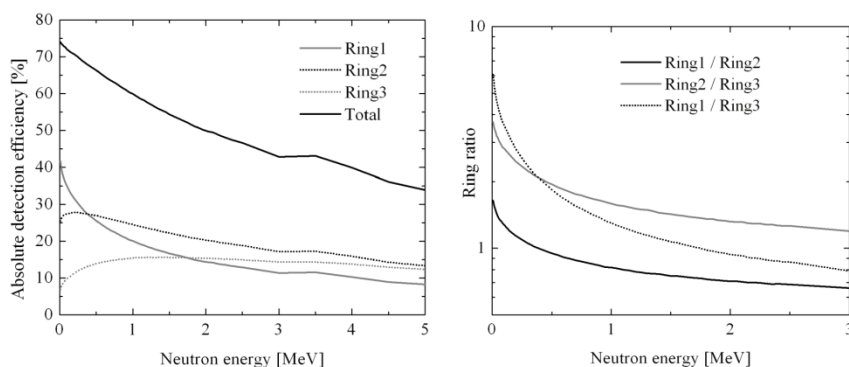


Fig. 15 - Neutron detection efficiencies of Ring1 (solid grey line), Ring2 (dotted black line) and Ring3 (dotted grey line) as well as the total efficiency (solid black line) in the left panel. In the right panel are represented the ring ratios of the  $4\pi$  triple-ring neutron detector.

Using such type of neutron detectors, neutron energies are determined not event by event but on the average with the so-called ring ratio technique developed by Berman and Fultz [46]. The ratio of the numbers of neutrons detected in two different rings of  $^3\text{He}$  proportional counters depends on the neutron energy as shown for the triple-ring neutron detector in Figure 15. As the three ring ratios in a different way depend on the original neutron energy, they can be used to determine the average neutron energy.

Using laser Compton backscattered  $\gamma$ -ray beams and the  $4\pi$  triple-ring neutron detector, photoneutron cross sections have been measured for 13 elements (D, Be, Se, Mo, Zr, Pd, Sn, La, Pr, W, Re, Os, Ta, Au, Pb) and 38 isotopes at the National Institute of Industrial Science and Technology, and for 4 elements (Ge, Nd, Sm, Dy) and 15 isotopes at the NewSUBARU synchrotron radiation facility. The measurement was however limited to  $(\gamma, n)$  cross sections near neutron threshold.

A large tank of Gd-doped liquid scintillator of Saclay type is not suited to experiments with low-frequency and extreme-intensity  $\gamma$ -ray beams like those expected at the ELI-NP facility. The tank becomes blind by a scattered- $\gamma$  flash every time the  $\gamma$ -ray beam hits a target. The operational voltage of the photomultiplier tubes must be suppressed to low enough to avoid possible damages by the intense  $\gamma$ -flash. Consequently, detection of neutron-capture  $\gamma$ -rays emitted in the  $\text{Gd}(n,\gamma)$  reaction is not necessarily straightforward.

### 3.1.2.2 Flat efficiency neutron detector for neutron multiplicity sorting

Quasi-monochromatic  $\gamma$ -ray beams produced in the positron annihilation in flight were used at the LLNL and Saclay in the photoneutron cross section measurement during 1950s through 1980s as discussed in Section 2.3. Therefore, the discrepancies in  $(\gamma, xn)$  cross section between the LLNL and Saclay data may have stemmed from the different neutron detection methods. In this regards, the ring-ratio technique may have a serious problem in neutron multiplicity sorting for the reason discussed below.

Let us consider  $(\gamma, xn)$  cross section measurements with the neutron detector of Livermore type. We limit our discussion to  $(\gamma, xn)$  cross section measurements with  $x$  taking values of 1 and 2 at the ELI-NP with the intense and monochromatic  $\gamma$ -ray beam whose maximum energy is 19 MeV. The number of single neutron (1n) and double neutron (2n) events experimentally observed,  $N_s$  and  $N_d$ , are respectively expressed by:

$$N_s = N_1 \cdot \varepsilon(E_1) + N_2 \cdot {}_2C_1 \cdot \varepsilon(E_2) \cdot (1 - \varepsilon(E_2)) \quad (3)$$

and

$$N_d = N_2 \cdot (E_2)\varepsilon^2 \quad (4)$$

where  $N_1$  and  $N_2$  are the number of neutrons emitted from the  $(\gamma, 1n)$  and  $(\gamma, 2n)$  reactions, respectively, and  $\varepsilon$  is the neutron detection efficiency. Obviously, the  $N_1$  and  $N_2$  are proportional to the reaction cross sections,  $\sigma(\gamma, 1n)$  and  $\sigma(\gamma, 2n)$ . Note that the single neutron events consists of two contributions from the  $(\gamma, 1n)$  and  $(\gamma, 2n)$  reactions.

The ring-ratio technique can be applied to the double neutron event ( $N_d$ ) to deduce the average neutron energy,  $E_2$ . However, the average neutron energy  $E_1$  for the  $(\gamma, 1n)$  channel cannot be determined by applying the technique to the single neutron event  $N_s$  because  $N_s$  consists of two contributions from the  $(\gamma, 1n)$  and  $(\gamma, 2n)$  reactions (see Eq. (3)). Namely, the detection efficiency cannot be determined separately for the  $(\gamma, 1n)$  and  $(\gamma, 2n)$  reaction channels. This is a fatal defect associated with the ring-ratio technique in the neutron multiplicity sorting

with a  $4\pi$  neutron detector whose detection efficiency strongly depends on neutron energy.

To overcome the defect of the ring-ratio technique in neutron multiplicity sorting, it is essential to develop a  $4\pi$  neutron detector of Livermore type but with flat efficiency. We remark that the East-Walton detector [88] which has excellent flatness over 0 – 5 MeV cannot be used because the intrinsic efficiency is too small (11.5%) for neutron multiplicity sorting. Obviously, even if we cover  $4\pi$  solid angle with the East-Walton detectors, the detection efficiency is 11.5% for single-neutron events and 1.3% for double neutron events.

### 3.1.3 Fast neutron measurement above 1 MeV with liquid scintillation detectors

Fast neutron measurements are carried out in two energy domains, above 1 MeV with liquid scintillation detectors and below 1 MeV with  ${}^6\text{Li}$  glass scintillation detectors. As discussed in 2.2 and 2.4, exclusive neutron decays of GDR, PDR, and M1 resonance are studied by means of fast neutron measurements. In this section, we describe fast neutron measurements above 1 MeV with liquid scintillation detectors.

Neutrons can be detected with a liquid scintillation detector based on elastic scattering of neutrons with protons. The kinetic energy of a recoil proton is expressed in the laboratory coordinate system by [89]

$$E_p = E_n \cos^2 \theta \quad (5)$$

where  $\theta$  is the laboratory scattering angle of the recoil proton. Thus, the recoil proton has kinetic energies ranging from the minimum energy 0 at  $\theta = 90^\circ$  (grazing collision) to the maximum energy  $E_n$  at  $\theta = 0^\circ$  (head-on collision).

The energy distribution of the recoil proton,  $P(E_p)$ , is expressed by [89]

$$P(E_p) = 4\sigma(\Theta)\pi/(\sigma_s \cdot E_n) \quad (6)$$

where  $\sigma(\Theta)$  represents the differential scattering cross section as a function of the scattering angle in the center-of-mass system of the recoil proton and  $\sigma_s$  is the total scattering cross section integrated over all angles. The neutron-proton scattering is a special case in which scattering takes place isotropically in the CM system,  $\sigma(\Theta) = \sigma_s/4\pi$ , leading to

$$P(E_p) = 1/E_n \quad (7)$$

The recoil proton has a rectangular energy distribution shown with a width  $E_n$  and a height  $1/E_n$  [89]. In reality, the distribution undergoes a distortion due to

three experimental factors, non-linear response of a scintillator, carbon scattering, and finite energy resolution.

The detection efficiency for neutrons depends on a discrimination level on proton energy. The efficiency drops to zero at the discrimination level and approaches the zero bias efficiency at higher neutron energies.

A small fraction of the kinetic energy deposited in a scintillator by a charged particle is converted into fluorescence energy. The rest is dissipated nonradiatively, primarily in the form of lattice vibration or heat. The fraction of the particle energy, which is converted into fluorescence light, depends on both the particle type and its energy. For liquid and plastic scintillators as well as other organic scintillators, the response to electrons is linear for energies above 125 keV [90], while the response to protons is always less for equivalent energies and nonlinear to much higher initial energies. At energies of a few hundred keV, the response to protons is smaller by a factor of 10 compared with the light yield of equivalent energy electrons.

A neutron time-of-flight multidetector, EDEN, is developed for decay studies of giant states (giant multipole resonances, high-lying single particle states, isospin modes) [90,91]. The EDEN employs BC501A liquid scintillators each with a cylindrical cell of 200 mm diameter and 50 mm height and has a typical dynamic range of 2 – 15 MeV for neutron energies. For a discrimination level of 60 keV (ee) in equivalent electron energy, which corresponds approximately to 500 keV in neutron energy, the intrinsic detection efficiency of an EDEN detector for 1 MeV neutrons is of approximately 50% [91].

A key factor in the photoneutron reaction study is to reduce the neutron discrimination level of a liquid scintillation detector as low as possible, especially in the study of pygmy dipole resonance and spin-flip M1 resonance, which are known to emerge near neutron threshold.

Let us consider at what level one can reduce the neutron discrimination energy. We discuss this issue in terms of the electron energy keVee, keeping it in mind that the scintillation response to protons is a factor of 10 lower than to electrons. Namely, the relation between the proton energy  $E_p$  and the equivalent electron energy  $E_{ee}$  is  $E_p \approx 10 \cdot E_{ee}$ . For the liquid scintillator NE102A, the total light yield of 10000 photons/MeVee is reported in the measurement using a photodiode with broad spectral response [92]. It is 1.7 photons/keVee for the BC501A according to the measurement using a BURLE-8575 photo-multiplier tube (PMT) with the wavelength of maximum emission 400 nm [93]. Here we take the latter value determined by the PMT output in the present evaluation.

In single photoelectron counting, a PMT with a gain  $2 \times 10^6$  produces output peak current 60  $\mu$ A in a 5 ns pulse and an amplifier with input impedance 50  $\Omega$  produces a 3 mV signal.

Single photoelectron counting would be possible if a noise level could be suppressed below 3 mV. In this case, the minimum number of scintillation photons  $N_{\min}$  is determined by  $N_{\min}\varepsilon_1\varepsilon_2\varepsilon_3=1$ , where  $\varepsilon$  is the collection efficiency of scintillation light,  $\varepsilon_2$  is the quantum efficiency of the photocathode, and  $\varepsilon_3$  is the collection efficiency of photoelectrons. Taking  $\varepsilon_1=0.7$ ,  $\varepsilon_2=0.25$  for an ordinary Bi-alkali photocathode, and  $\varepsilon_3=0.8$  for a PMT of head-on type, one finds  $N_{\min} \approx 7$ . Assuming the light yield 1.7 photons/keV, the minimum detectable energy is 4.2 keV, which corresponds to  $N_p \approx 42$  keV. This means that 80 keV neutrons could be detected with about 50% efficiency in the case of single photoelectron counting with a PMT.

Table 4  
Counting parameters in the single photoelectron counting with a PMT and energy discrimination levels for electrons, protons, and neutrons.

PMT gain	$2 \times 10^6$
PMT output peak current	60 $\mu$ A (pulse width 5ns)
Amplifier output peak voltage	3mV (input impedance 50 $\Omega$ ) <input type="checkbox"/>
$\varepsilon_1$ – scintillation light collection efficiency	0.7
$\varepsilon_2$ – quantum efficiency	0.25
$\varepsilon_3$ – photoelectron collection efficiency	0.8
$N_{\min}$ - minimum number of scintillation photons	7
Energy discrimination levels for electrons, protons and neutrons	4.2 keV, $E_p \approx 42$ keV, $E_n \approx 80$ keV (50% efficiency)

The result of the above consideration based on single photoelectron counting with a PMT is summarized in Table 4.

The velocity ( $v$ ) of a neutron with a kinetic energy ( $T$ ) is expressed in the relativistic kinematics by [94]

$$v = \beta c = \frac{pc^2}{E} = \frac{\sqrt{T(T+2mc^2)}c}{T+mc^2} \quad (8)$$

where  $p$  is the momentum,  $m$  is the rest mass, and  $E$  is the total energy of the neutron. The flight time for the flight path length  $L$  is given by

$$t = \frac{L}{v} = \frac{L(T+mc^2)}{\sqrt{T(T+2mc^2)}c} \quad (9)$$

Thus, the kinetic energy  $T$  is determined from the flight time  $t$  by

$$T = mc^2 \left( \frac{1}{\sqrt{1-(L/ct)^2}} - 1 \right) \quad (10)$$

The energy resolution is determined by two factors, the thickness of a liquid scintillator and the time resolution of electronics origin. The former gives the uncertainty of  $L(\delta L)$ , while the latter gives the uncertainty of  $t(\delta t)$ . From the error propagation, the uncertainty of the kinetic energy  $\Delta T$  is given by

$$\Delta T = \frac{mc^2}{(ct)^2} \frac{L}{[1-(L/ct)^2]^{3/2}} \sqrt{(\delta L)^2 + \left(\frac{L}{t}\right)^2 (\delta t)^2} \quad (11)$$

The TOF measurement requires a time range of 512 ns which is achieved by thinning micro-bunches of a  $\gamma$ -ray beam with 16 ns interval so that a 100 Hz macro-bunch contains only one micro-bunch.

The uncertainty  $\Delta T$  is dominated by the thickness of the liquid scintillator. Obviously, the energy resolution  $\Delta T/T$  is sensitive to the flight path length  $L$ . For  $L = 1.5$  m, the  $\Delta T/T$  ranges from 6.7 – 7.8% over photoneutron kinetic energies  $T = 0.1 - 5.0$  MeV.

As discussed above, a lowest possible discrimination level can be achieved by single photoelectron counting. For the single photoelectron counting, thermal electron emissions from the photocathode need to be suppressed by applying a time gate of 512 ns in the TOF measurement every macro-bunch of a  $\gamma$ -ray beam at 100 Hz.

Decomposition of the total photoneutron cross section into partial cross sections for  $s$ - and  $p$ -wave neutrons is equivalent to characterizing the electromagnetic property by E1 and M1 multipoles. Photoneutron measurements along this line of research play a complementary role to measurements of the gamma decay of pygmy E1 dipole resonance (PDR) and spin-flip M1 resonance below neutron threshold. The pygmy dipole and M1 resonances emerge not only below but also above neutron threshold ( $S_n$ ). Indeed, rich peak structure is detected above neutron threshold in  $^{53}\text{Cr}$ ,  $^{57}\text{Fe}$ ,  $^{207,208}\text{Pb}$  above  $S_n$  [95,14].

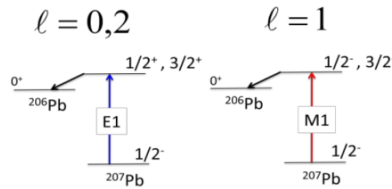


Fig. 16 - E1 and M1 photoexcitations of  $^{207}\text{Pb}$  followed by  $s$ -,  $d$ - and  $p$ - wave neutrons.

Figure 16 depicts E1 and M1 photoexcitations of  $^{207}\text{Pb}$ . The selection rule of spin and parity tells that the E1 excitation of the  $^{207}\text{Pb}$  in the ground state ( $1/2^-$ ) to the  $1/2^+$  and  $3/2^+$  states is followed by  $s$ - and  $d$ -wave neutron decay to the ground state in  $^{206}\text{Pb}$ , while the M1 excitation to  $1/2^-$  and  $3/2^-$  states is by  $p$ -wave neutron decay. In the photoexcitation near neutron threshold, the  $d$ -wave neutron emission is strongly suppressed by the centrifugal potential compared to the  $s$ -wave neutron emission. One can find the same correlation of E1 (M1) photoexcitation with the  $s$ -wave ( $p$ -wave) neutron emission for  $^{208}\text{Pb}$ .

Obviously  $s$ -wave neutrons are emitted isotropically. In contrast, when the photoexcitation is induced by linearly-polarized gamma rays, the  $p$ -wave neutron emission is characterized by the angular distribution,

$$W(\theta, \varphi) = 3 [\sin^2 \theta (1 + \cos 2\varphi)]/8\pi \quad (12)$$

Here,  $\theta$  is the polar angle with respect to the  $z$ -axis chosen along incident direction of the  $\gamma$ -ray beam and  $\varphi$  is the azimuthal angle with respect to the  $x$ -axis chosen along the electric field (linear polarization).

When limited to a separation of  $s$ - and  $p$ -wave neutrons, an anisotropy measurement of neutron emissions may suffice. However, for an unambiguous separation of  $s$ -,  $p$ -, and higher partial-waves, an angular distribution measurement is required. The angular distribution measurement can be done with an array of liquid scintillation detectors and/or  $^6\text{Li}$  glass scintillation detectors with the time of flight technique.

#### 3.1.4 Fast neutron measurements below 1 MeV with $^6\text{Li}$ glass scintillation detectors

The energy region from neutron threshold up to 1 MeV is a rich field where PDR and M1 resonance manifest themselves [38].  $^6\text{Li}$  glass scintillator is known to be sensitive to neutrons in this low-energy region.

The detection principle is discussed in Sec. 3.1.2.1. Neutrons are converted into charged particles by the  $^6\text{Li}(n,\alpha)^3\text{H}$  reaction with a large  $Q$ -value of 4.78 MeV. The reaction cross section is 0.25 b at 1 MeV, 3.5 b at the peak of the 245 keV resonance, 0.7 barn at 100 keV and increases following the  $1/v$  law with decreasing energy below 100 keV. In principle, low-energy neutrons down to thermal neutrons can be measured with a  $^6\text{Li}$  glass scintillation detector.  $^6\text{Li}$  glass scintillators are available with high concentrations up to 7.7 wt %, relatively fast response time, and large areas and thicknesses that can easily be fabricated. These scintillators are in popular use in low-energy neutron spectrometry and in applications to neutron time-of-flight spectroscopy.

### 3.2 The thermal neutron detection system

In this section, we propose detection systems for studies of the  $p$ -process nucleosynthesis and the neutron decay of GDR based on neutron-multiplicity sorting. We propose to use a high-efficiency  $4\pi$  neutron detector (ELIGANT-TNH) to measure  $(\gamma, n)$  cross sections near neutron threshold for the former study, while we propose to use a flat-efficiency neutron detector (ELIGANT-TNF) to measure  $(\gamma, xn)$  ( $x=1,2$ ) cross sections for the latter study. The experimental principle of the neutron multiplicity sorting is described in 3.1.2.

#### 3.2.1 High efficiency $4\pi$ neutron detector

A *Day 1* experiment focuses on the  $^{180}\text{Ta}(\gamma, n)^{179}\text{Ta}$  and  $^{138}\text{La}(\gamma, n)^{137}\text{La}$  reactions by  $4\pi$  measurements of single neutron emission. Due to the high intensity of the  $\gamma$ -ray beam and the high efficiency of the neutron detector, the  $(\gamma, n)$  destruction cross section measurements are feasible with low amounts of samples of approximately  $1 \text{ mg/cm}^2$ . This is a great feature for measuring reactions induced on rare  $p$ -process nuclei.

##### 3.2.1.1 Geometry and active detection elements

We propose to use a high-efficiency  $4\pi$  triple-ring detector (ELIGANT-TNH) based on the detection principle described in 3.1.2.1, where  $H$  stands for high efficiency.  $^3\text{He}$  proportional counters with the highest neutron detection efficiency per volume are the best choice in view of the rare isotope measurement and the space constraints imposed by the dimensions of the E8 experimental hall.

Table 5

A summary of the ring configuration and detector elements of the ELIGANT-TNH. The polyethylene moderator is a cube of  $36 \times 36 \times 50 \text{ cm}^3$ .

Configuration	$^3\text{He}$ counters	Distance [cm]
Ring1	4	3.8
Ring2	8	7.0
Ring3	8	10.0
Total	20	

The active detection elements are 20 cylindrical proportional counters, each containing 10 bars of  $^3\text{He}$ . The  $^3\text{He}$  proportional counters are embedded in a neutron moderator, with the target placed at the center of the moderator.

Each  $^3\text{He}$  proportional counter is of cylindrical shape, with 2.5 cm diameter and 49.5 cm length. The sensitive length is of 45 cm. The proportional counters are placed equally spaced in three concentric rings, named Ring1, Ring2 and Ring3, of 80, 140 and 200 mm diameter respectively. Ring1 contains 4 detectors, while Rings 2 and 3 contain 8 detectors each. The neutron moderator is a cube of  $36 \times 36 \times 50 \text{ cm}^3$  made of polyethylene. The moderator is covered by additional 5-cm-thick polyethylene plates with 1-mm-thick cadmium metal for background neutron suppression. The geometrical configuration of detector elements of the ELIGAN-TNH is summarized in Table 5.

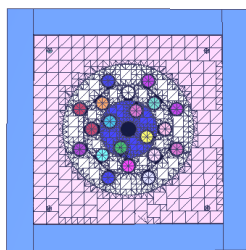


Fig. 17 - Transversal section of the neutron detector.

Figure 17 shows a transversal section of the neutron detector. A similar neutron detector is in use at the gamma beam line GACKO (Gamma Collaboration Hutch of Konan University) of the synchrotron radiation facility NewSUBARU [97]. A picture of it, involving the moderator and also the inserted proportional counter, is shown in Fig. 18. The detector which is in active use at GACKO has high efficiencies for neutron detection. Neutrons emitted in  $(\gamma, n)$  reaction near neutron threshold have the average kinetic energies below 1 MeV [50,51]. The detector has 60 – 74% efficiencies for neutrons with energies below 1 MeV as shown in Fig. 15. The average neutron energy is determined with the ring-ratio technique as discussed in Sec. 3.1.2.1. The detector is highly sensitive to the average neutron energy (see Fig. 15).

A target material irradiated with a  $\gamma$ -ray beam is a source of neutrons. During the experiments, the neutron-emitting source is located inside the detector cavity, at the center of the moderator. The moderator is designed to have a cavity on the beam axis, so that the beam can pass through the detector without intercepting moderator material.

In addition to the high detection efficiency, the  $^3\text{He}$  proportional counter has an excellent capability of gamma–neutron discrimination. Figure 19 shows a

typical energy spectrum of a  $^3\text{He}$  proportional counter. The energy peak corresponds to the Q value of the reaction, namely the events when both of the reaction products are stopped in the  $^3\text{He}$  gas. At lower energies we have a wide flat energy range for the events when either the tritium or the proton is stopped in the detector's wall, energy area called the "wall effect" plateau.



Fig. 18 - Neutron detectors installed at the gamma beam line GACKO.

Gamma events are clearly separated from neutron events, as their pulse height is much lower than that of neutrons which is amplified by the reaction Q-value. Therefore the gamma-neutron discrimination can be easily achieved by applying pulse-height discrimination.

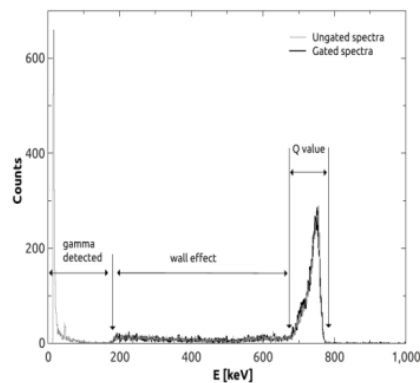


Fig. 19 - Energy spectra of a  $^3\text{He}$  proportional counter obtained with a  $^{252}\text{Cf}$  source placed at the center of the polyethylene moderator. One can observe a clear distinction between the gamma and neutron events.

Figure 19 shows the raw spectra with no threshold in grey line and the gated spectra in black line. The threshold level is applied just below the “wall effect” plateau.

### 3.2.1.2 Dependence of the detection efficiency on $p$ -wave neutrons

The ELIGANT-TNH (high-efficiency  $4\pi$  neutron detector) is featured with high efficiencies for  $s$ -wave (isotropic) neutrons as shown in Fig. 15. As discussed in Sec. 3.1.3,  $s$ -,  $p$ -, and higher partial-wave neutrons are expected to be emitted in the photoexcitation of nuclei with E1, M1, and higher-multipolarities induced by linearly polarized  $\gamma$ -rays. Neutrons emitted from an irradiation sample are detected with the ELIGANT-TNH after being moderated in the polyethylene. Therefore, the angular distribution of neutrons would be smeared out to large extent at the time of their arrivals at the  $^3\text{He}$  proportional counters.

We have examined the dependence of the detection efficiency on the angular distribution of  $p$ -wave neutrons by the GEANT4 simulation. Neutrons are generated in the GEANT code following the  $p$ -wave angular distribution given by Equation 12, shown in Figure 20.

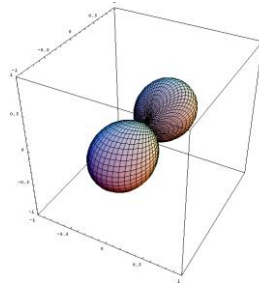


Fig. 20 - Angular distribution of  $p$ -wave neutrons. The polarization axis of  $\gamma$ -rays with 100% linear polarization lies in the horizontal plane.

Figure 21 shows detection efficiencies of the Ring1, Ring2, and Ring3 (Fig. 17) for 4.5 MeV  $p$ -wave (anisotropic) neutrons obtained by the GEANT4 simulation in comparison with those for 4.5 MeV  $s$ -wave (isotropic) neutrons obtained by the MCNPX simulation, which are the same result as the one shown in Fig. 15. As seen in the figure, the efficiencies of the three rings after summing neutrons detected by 4, 8, and 8  $^3\text{He}$  counters, respectively, remain the same for  $s$ - and  $p$ -wave neutrons, indicating a strong smearing effect of the polyethylene moderator.

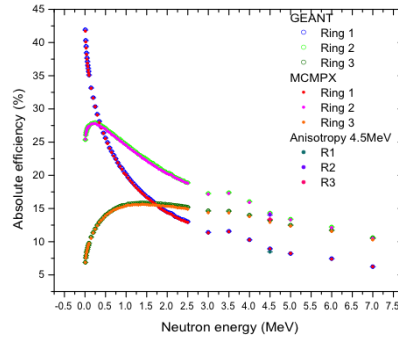


Fig. 21 - Detection efficiencies of the Ring1, Ring2, and Ring3 for 4.5 MeV *s*- and *p*-wave neutrons.

Figure 22 shows neutron energy spectra for the middle ring of 8  $^3\text{He}$  counters (Fig. 17) and the number of neutrons detected by two counters in the horizontal plane, 2 counters in the vertical plane and 4 counters mounted at  $45^\circ$ .

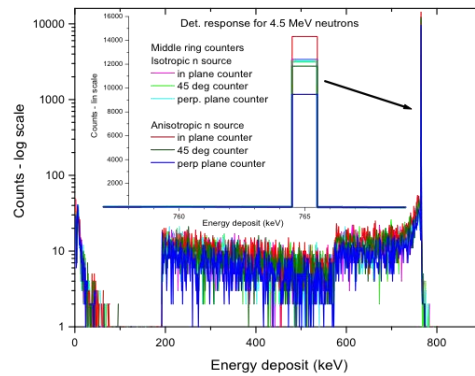


Fig. 22 - Neutron energy spectra of the Ring2 for 4.5 MeV *s*- and *p*-wave neutrons. A small angular distribution effect is seen when looking at individual  $^3\text{He}$  counters.

One can see that a very small angular distribution effect survives from the smearing by polyethylene when looking at the neutron events of individual  $^3\text{He}$  counters belonging to the same ring. By summing neutron events, the differences in counting efficiency among the individual counters are cancelled out, giving the same detection efficiency independent of *s*- and *p*-wave neutrons. Thus, we reach a conclusion that the angular distribution effect of neutrons on the total detection

efficiency of the ELIGANT-TNH is negligible, thanks to the moderation effect. A typical experimental condition for the *Day 1* experiment on the  $^{180}\text{Ta}(\gamma, n)^{179}\text{Ta}$  reaction is given in Table 6.

Table 6

A typical experimental condition for the *Day 1* experiment on the  $^{180}\text{Ta}(\gamma, n)^{179}\text{Ta}$  reaction.

Target	$^{180}\text{Ta}$ : 1mg/cm <sup>2</sup>
$\gamma$ -ray Beam	$8 \times 10^8$ cps $\Delta E/E = 0.5\%$ $8 \times 10^6$ per macro-bunch (100 Hz) $2.5 \times 10^5$ (32 micro-bunches, 16ns)
Cross section	20 mb
Detection efficiency	60%
Count rate	32 cps $10^{-2}$ counts/micro-bunch 0.32 counts/macro-bunch

### 3.2.2 Flat-efficiency $4\pi$ neutron detector (ELIGANT-TNF)

The ELIGANT-TNF is a flat efficiency  $4\pi$  neutron detector consisting of the same detector elements as those of the ELIGANT-TNH, but with a different configuration of  $^3\text{He}$  proportional counters in a polyethylene moderator. The configuration which ensures a flat efficiency was searched by Monte Carlo simulations with the GEANT4 code [15,85]. Figure 23 depicts a front view of a best possible configuration consisting of three rings of 4, 9, and 18  $^3\text{He}$  counters that are located at the distances of 5.5 cm, 13 cm and 16 cm from the  $\gamma$ -ray beam axis, respectively. The dimension of the polyethylene moderator is 56 cm (horizontally)  $\times$  56 cm (vertically)  $\times$  50 cm (along the beam axis). The moderator is shielded by additional 5 cm polyethylene plates with cadmium for background neutron suppression.

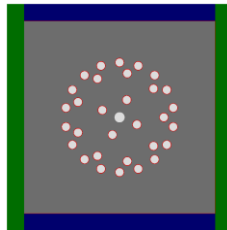


Fig. 23 - Cross sectional view of the geometrical configuration of the ELIGANT-TNF.

Figure 24 shows the total neutron detection efficiency along with efficiencies of the three rings. The total efficiency is 40 – 37.5% over a neutron energy range 0 – 4 MeV and 40 – 35% over 0 – 5 MeV. The flatness is achieved by compensating the strong energy dependence of the efficiency of Ring 1 (inner ring), which rapidly decreases with increasing neutron energy, by those of Ring 2 (middle ring) and Ring 3 (outer ring), which increases with increasing energy. It is important to point out that the total efficiency of the ELIGANT-TNF is sufficiently high for neutron multiplicity sorting. It is about 40% for single-neutron detection, about 16% for double-neutron detection, and about 6.4% for triple-neutron detection though the sorting is limited to double-neutron detection at ELI-NP. Such a flat- and high-efficiency neutron detector has never been developed before.

The geometrical configuration of detector elements of the ELIGANT-TNF is summarized in Table 7.

The moderation of neutrons in polyethylene takes time of the order of 100  $\mu\text{s}$  in the moderation time constant ( $\tau$ ) defined in  $e^{-t/\tau}$  [98]. Therefore, we use a  $\gamma$ -ray beam with 100 Hz macro-bunches each containing only one micro-bunch. In other words, only one micro-bunch out of 32 micro-bunches is picked up by a thinning technique. The neutron multiplicity sorting can be done by measuring neutrons with a multi-stop TDC, for example, in a time range 800  $\mu\text{s}$  [99].

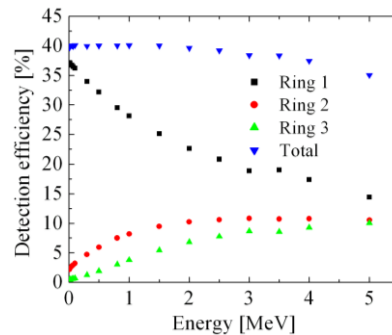


Fig. 24 - Total neutron detection efficiency along with efficiencies of Ring1, Ring2, and Ring3 of the ELIGANT-TNF.

The count rate for single-neutron and double-neutron events are estimated from Eqs. (3) and (4), namely,  $N_s = N_1 \cdot \varepsilon + N_2 \cdot 2C_1 \cdot \varepsilon \cdot (1 - \varepsilon)$  and  $N_d = N_2 \cdot \varepsilon^2$ , respectively. Here  $N_1$  is given by  $N_1 = N_\gamma N_t \sigma_{1n}$  with the number of gamma rays  $N_\gamma$ , the number of target nuclei  $N_t$ , and the 1n cross section  $\sigma_{1n}$ , while  $N_2$  by  $N_2 = 2N_\gamma N_t \sigma_{2n}$  with the 2n cross section  $\sigma_{2n}$ . The  $\varepsilon$  is the total detection efficiency of the ELIGANT-TNF,  $\varepsilon \approx 0.4$ .

Table 7

A summary of the ring configuration and detector elements of the ELIGANT-TNF. The polyethylene moderator is a cube of  $56 \times 56 \times 50$  cm<sup>3</sup>.

Configuration	<sup>3</sup> He counters	Distance [cm]
Ring 1	4	5.5
Ring 2	10	13.0
Ring 3	18	16.0
Total	32	

A typical experimental condition for the *Day 1* experiment on the <sup>159</sup>Tb( $\gamma$ ,xn) reaction is given in Table 8. A detailed study of background gamma and electron events of target origin performed using Monte Carlo simulations is presented further below.

Table 8

A typical experimental condition for the *Day 1* experiment on the <sup>159</sup>Tb( $\gamma$ ,xn) reaction.

Target	<sup>180</sup> Ta: 100 mg/cm <sup>2</sup>
$\gamma$ -ray Beam	10 <sup>6</sup> cps $\Delta E/E = 0.2$ % 10 <sup>4</sup> /macro-bunch (100 Hz) 1 micro-bunch/macro-bunch
Cross section	$\sigma_{1n} = 50$ mb $\sigma_{2n} = 50$ mb
Detection efficiency	$\epsilon \approx 40\%$
Count rate	$N_s$ (single neutron events): 25 cps $N_d$ (double neutron events): 6 cps

### 3.3 The gamma detector system (ELI-GANT-GN)

As already discussed in this TDR, the today optimal choice for the  $\gamma$ -ray detectors consist in a mixed array composed by LaBr<sub>3</sub>:Ce and CeBr<sub>3</sub> cylindrical 3"  $\times$  3" crystals, namely with a diameter of 7.5 cm and a thickness of 7.5 cm.

The array should be placed in a backward position relative to the beam direction and should cover a solid angle of  $1\pi$ . In fact, in the forward  $2\pi$  the background is too strong and should be left as free of material as possible. The remaining  $1\pi$  backward solid angle should be covered by the liquid scintillator detectors for fast neutrons measurement.

Two different designs can be arranged, in the first setup  $1\pi$  will be used for  $\gamma$ -ray detectors only while the other  $1\pi$  will be used for liquid scintillators only, a schematic view can be seen in Figure 25.

In the second setup both the two detector types are placed in the backward  $2\pi$ . In fact,  $\gamma$ -ray detectors should be placed at 25–30 cm from the target while liquid scintillators at 0.5–1.5 m, therefore it should be possible to design a mechanical frame with alternated rings of the two detector types. This type of geometry could be more efficient but requires a much more difficult and accurate mechanical design of the frame.

The choice between the two geometries depends on the cost and feasibility of the mechanical frame. In this document we assume that the mechanical design is that of the first solution with 17  $\text{LaBr}_3\text{:Ce}$  and 17  $\text{CeBr}_3$  detectors  $3'' \times 3''$  placed at 30 cm from the target. However, no major differences are expected if the second mechanical setup will be used.

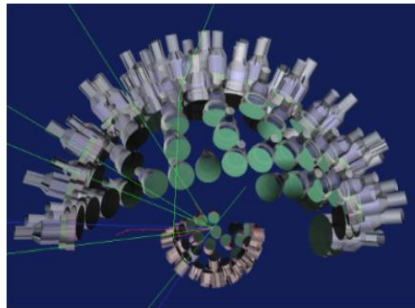


Fig. 25 - A schematic view of the ELI-GANT-GN setup. The  $\gamma$  radiation detectors are placed at 30 cm from the target (in the lower part of the drawing) and the liquid scintillators are placed at 150 cm from the target (in the upper part of the drawing).

### 3.3.1 Detector technical design

Each crystal should be placed in an aluminum housing. The front surface should be shielded by an absorber of 1 mm of lead 0.5 mm of Cu and 0.5 mm of Cd to stop low energy gamma rays and to reduce the energy of fast electrons/positrons. Around the detector one additional shield of 3 mm of Pb (to reduce the gamma side scattering) and some borated wax (to stop thermal neutrons) should be additionally placed.

As  $\text{LaBr}_3:\text{Ce}$  and  $\text{CeBr}_3$  are highly hygroscopic, it is possible to buy either a complete detector system (where the crystal is glued to the PMT and the housing air-sealed) or an encapsulated capsule (which should be placed in an external housing and coupled to a PMT). In the first case there is, in average, a gain of 0.1 - 0.2% in energy resolution but it is not possible to act on the detector. Whatever is the problem the detector could have (crystal, PMT, mechanics) it should be sent to the manufacturing company for maintenance. In the second case everything is accessible. If it is important an in-house maintenance the best choice would be to buy separately the encapsulated crystal and the PMT so that the complete assembly of the detector can be performed inside the ELI-NP facility.

The today best choice for good energy resolution for 3"×3"  $\text{LaBr}_3:\text{Ce}/\text{CeBr}_3$  crystals is the PMT produced by Hamamatsu R6233-100 or R10233-100. These PMTs have a superbialkali (SBA) photocathode. In addition, a selection on quantum efficiency, gain and linearity in the response could be required. The optical grease for the coupling is BC-630 from St. Gobain. The passive voltage divider designed by Hamamatsu for R6233-100 PMT (model E1198-26) is not the best choice in terms of cost and performance. An active voltage divider especially designed for linearity is the solution which should be followed. A possible choice is the one discussed in reference [100].

Each bromide detector should be powered with about 500 – 1000 V. An important issue is the fact that the provided high voltage should be extremely stable as a drift of less than 1 V in the voltage will degrade the energy resolution.

A possible today choice is the A1588 board from CAEN (which provides 2 kV max voltage with a guaranteed stability of 0.1 V) inserted in a system as for example SY4527 (which can allocate 10 or 16 boards). This solution for the HV can also be used for liquid scintillators using, therefore, a common SY4527 system. In addition, it should also be possible to read and write in the DAQ the values of the measured voltages so that one could correct the gain in the offline sorting process.

Because of the ELI-NP beam structure, the most straightforward choice is to digitize the bromide detectors anode signals so that energy, time, pulse separation and pile up rejection algorithms can be applied in the offline sorting and, if fast enough, also in the online spy code.

As the duty-cycle of ELI-NP machine is 10 ms the simplest solution is to provide to bromide DAQ an external trigger (given by the accelerator) and to digitize continuously during the 32 micro-shots of the beam ( $32 \times 16 = 516$  ns). Namely, the DAQ should digitize the detector anode signals from each detector for 1  $\mu\text{s}$  after the external trigger arrival. With this solution the data acquisition rate is the same of the ELI-NP duty-cycle, namely 100 Hz.

Using, for example, the V1730 board (14 bits and 500 MS/s) we expect to have in one second 100 events which consists of 32 vectors of 500 points each with

14 bits precision. Namely a data flow of  $100 \times 32 \times 500 \times 14 = 22$  Mbits/s. It is a rate that, even today, can be easily managed by data acquisitions.

This solution requires a VME crate and 32 channels of digitizers. As an example, we would need two CAEN V1730 digitizers board (each with 16 channels) and an optical fiber to connect the boards to a PC for control and data storage. The connection between the bromide detectors and digitizer is provided by MCX coaxial connectors. In addition to the boards, energy, time, pulse separation and pile up rejection algorithms should be written and implemented either on the machine where pulses are stored or on a dedicated PC for the on/off-line analysis. In Figure 26 there is a drawing of the electronic chain and at the end of the section there is a list of the equipment which we think is needed for the setup.

Even though all the operations (included the monitor of the signal line-shape) could be performed using this digital experimental setup, it is useful to provide a simpler and robust system to quickly monitor and check detector performances. In this case some additional electronics is required. In particular the  $\text{LaBr}_3:\text{Ce}/\text{CeBr}_3$  anode signals need to be splitted into three branches:

- 1<sup>st</sup> Branch: detector pulses are sent to digitizers as previously explained;
- 2<sup>nd</sup> Branch: free for an inspection (i.e. from an oscilloscope);
- 3<sup>rd</sup> Branch: detector pulses are sent to the analog electronic chain.

The analog electronic chain is designed to provide the count rate of every bromide crystal, an independent measurement of the deposited energy and, if necessary, a fast vs slow information to discriminate between the alpha particles from internal radiation and gamma rays. In addition, it can provide a high level trigger and the visualization of the measured in-beam energy and time spectra. This system is practically ready as it could use units and modules already available now and can provide a working DAQ which can be implemented since the very beginning of the construction of the array and does not need any particular maintenance.

The scheme in Figure 26 shows the electronic chain if only digitizers are used while Figure 27 presents the setup with, in addition, the analog electronic chain just discussed.

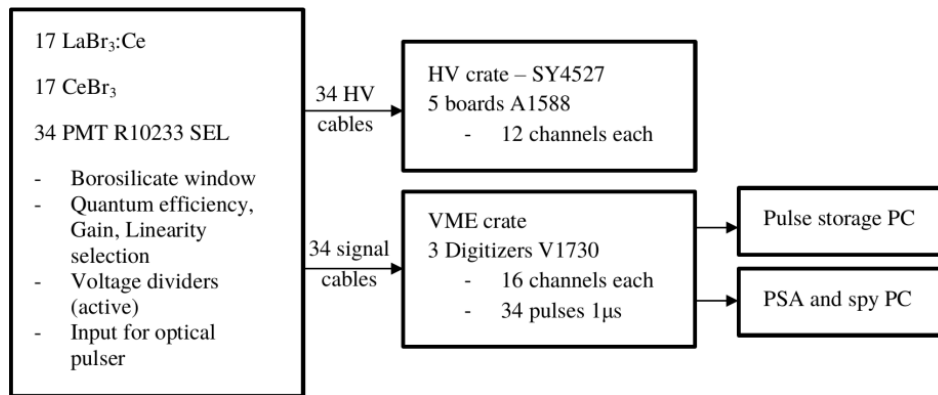


Fig. 26 - A scheme of the electronic chain in only digitizers are expected to be used.

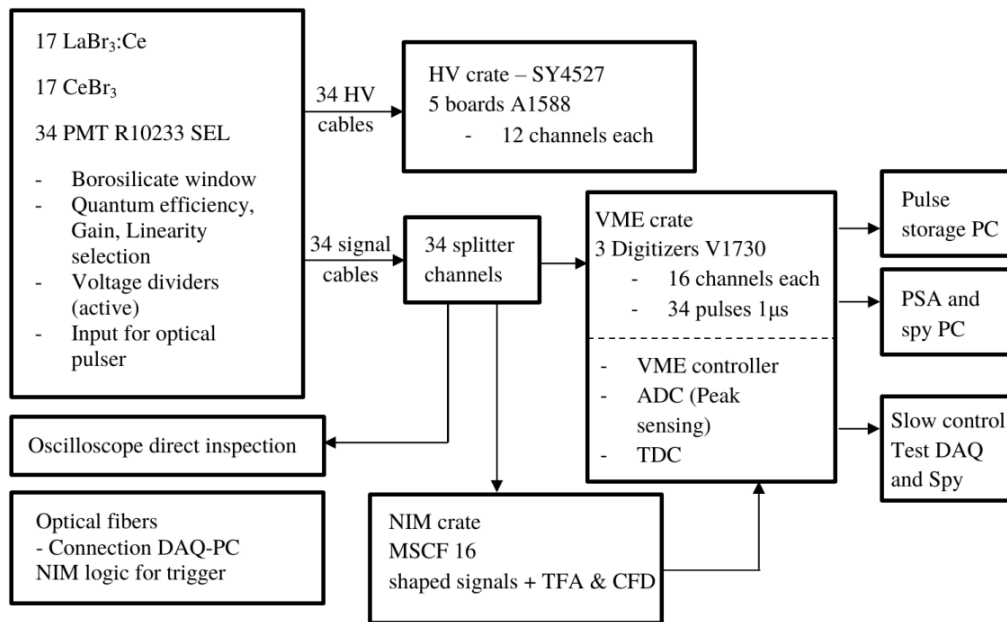


Fig. 27 - A scheme of the electronic chain if both the analog and digital electronic chain are expected to be used.

Thus, we propose to use the following detectors with associated accessories: 17 crystals of LaBr<sub>3</sub>:Ce, 17 crystals of CeBr<sub>3</sub>, 34 PMT R6233-100 having selected gain and linearity, 34 voltage dividers, 34 aluminum housings, 34 Pb-Cu-Cd absorbers and 34 side absorbers.

The high voltage supply section will involve the procurement of 34 SHV HV cables, one Mainframe SY4527 and 5 Boards A1588 (each board being able to power 12 detectors).

The digital part of the DAQ will consist in one VME Crate, 3 V1730 boards (14 bits and 500 MS/s) each with 16 channels, optical connection fiber, 34 MCX coaxial cables and a PC with the proper PCIe board to acquire and store digitized data.

For the purpose of online monitoring while performing the experiment we propose to use an additional analog chain consisting from: one NIM Crate, 34 channels of splitter (with three outputs), 34 channels of PARIS-pro like modules, 34 channels of scalers, 2 peak sensitive ADCs, 2 peak sensitive TDCs, one VME controller and on PC for slow control and on-line visualization.

Of course, GANT group will also need the usual laboratory equipment used in nuclear physics experiments: oscilloscope, multi-meter, tool cart, shielding, aligning instruments, etc.

### 3.4 The neutron detection system

Exclusive measurements of neutron decays of GDR, PDR, and MDR would require a wide energy range, high-resolution measurement of neutron energies, and a measurement of the neutron angular distribution. The requirements are fulfilled by an array of appropriate neutron detectors covering large energy and angular ranges and the TOF technique of measuring neutron energies with sufficient resolution.

The neutron energy range below 1 MeV is a rich field of observing PDR and MDR as shown in the measurement with the threshold neutron technique [71,14]. In contrast, the neutron energy may be several MeV in pre-equilibrium neutron decays of GDR on the high-energy side. Therefore, we need two kinds of detector elements for the ELIGANT-GN, BC501A (equivalently NE213) liquid scintillation detectors for high-energy neutrons above 1 MeV [90,91] and GS20 (equivalently NE905)  ${}^6\text{Li}$  glass scintillation detectors for low-energy neutron spectrometry below 1 MeV [101].

The scintillation properties of BC501A and GS20 are listed in Tables 9 and 10, respectively.

Since the liquid scintillation detector is widely used in nuclear science as discussed in Sec. 3.1.3, here we further comments on the property of the  ${}^6\text{Li}$  glass scintillator. In contrast to the pulse shape discrimination of neutrons and gammas by the liquid scintillator, the  ${}^6\text{Li}$  glass scintillator can distinguish neutrons and gammas simply by pulse height because of the large reaction Q-value (4.78 MeV) of the  ${}^6\text{Li}(n,\alpha){}^3\text{H}$  reaction. The low light output of GS20 relative to that of BC501A is compensated by the large reaction Q-value. Figure 28 shows a pulse-

height spectrum of a GS20 [102] for neutrons produced from the  ${}^7\text{Li}(p,n)$  reaction. The component in the 700 – 1400 channels is formed by neutrons, while the low pulse-height component is by gamma rays. The maximum energy of neutrons is 550 keV. But the spectrum includes thermal neutrons that were produced in passing through a 2 cm polyethylene plate placed immediately after the neutron source.

Table 9  
BC501A (liquid scintillator).

Light output % Anthracene	78
$\lambda$ of maximum emission [nm]	425
Decay times of first three components	3.2, 32.3, 270 ns
H/C atomic ratio	1.212

Table 10  
GS20 ( ${}^6\text{Li}$  glass scintillator).

Light output % Anthracene	20 – 30
$\lambda$ of maximum emission [nm]	395
Decay times, neutron excitation	18.57, 98 ns
Content of Li	6.6 wt %
${}^6\text{Li}$ enrichment	95%
Density [ $\text{g}/\text{cm}^3$ ]	2.5
Refractive index	1.55

We require essentially the same time resolution in the TOF measurement and solid-angle coverage per detector for both liquid and  ${}^6\text{Li}$  glass scintillation detectors. We design the BC501A scintillation detectors with 20 cm diameter and 5m thickness. Because the GS20 scintillation detectors will be used for lower energy neutron detection, they can be placed closed to the target than the BC501A scintillation ones. Therefore, we require smaller diameter for the GS20 scintillation detectors, of only 10 cm. Also, in order to maintain the same time resolution in the TOF measurement at smaller distances from the target, we restrict the thickness of GS20 detectors to 2 cm. We can use the same PMTs for both BC501A and GS20 because of the wavelength of maximum emission is close to each other. A schematic image of one detector is displayed in Fig. 29.

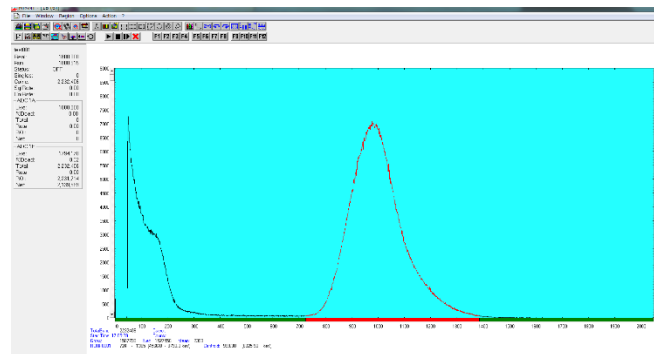


Fig. 28 - A pulse-height spectrum of a GS20 scintillation detector.

The detection efficiency can be calculated with the reaction cross section. For GS20 with 6.6 wt % in  ${}^6\text{Li}$ , the intrinsic efficiency is 2.0%, 28% and 5.6% for neutrons at 1 MeV, 245 keV (resonance), and 100 keV, respectively. These efficiencies are to be compared with the efficiency 30 – 60% of the liquid scintillation detector over 0.5 – 5 MeV.

In the neutron TOF spectroscopy, neutron capture reactions which take place inside the  ${}^6\text{Li}$  glass scintillator may be a source of background  $\gamma$ -rays that cannot be separated by TOF. However, these background  $\gamma$ -rays can be safely neglected because the neutron capture cross section for a primary glass element Si is 0.11 – 0.18 barns for  ${}^{28,29,30}\text{Si}$  even at the thermal energy which is by four orders of magnitude smaller than the  ${}^6\text{Li}(n,\alpha){}^3\text{H}$  reaction cross section.

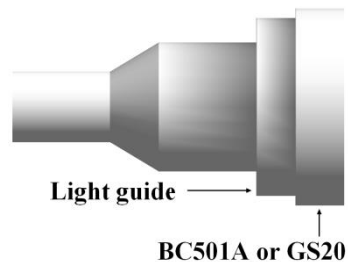


Fig. 29 - A schematic image of the BC501A and GS20 neutron detectors.

As discussed in Sec. 3.1.3, the E1 and M1 excitations populating PDR, MDR, and GDR are identified by detecting  $s$ -,  $p$ -,  $d$ - and  $f$ -wave neutrons. Figure 30 depicts the angular distributions of  $s$ -wave and  $p$ -wave neutrons. Obviously  $s$ -wave neutrons are emitted isotropically, while  $p$ -wave neutrons are emitted preferentially along the linear polarization of the  $\gamma$ -ray beam. Although  $s$ - and  $p$ -

wave neutrons can be separated by measuring the anisotropy of neutron emission [83], a complete separation of neutrons with higher partial waves requires a measurement of the neutron angular distribution. We propose to measure the angular distribution with the BC501A and GS20 scintillation detectors with the TOF technique of measuring neutrons with sufficient energy resolution.

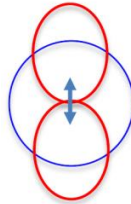


Fig. 30 - Angular distribution of *s*- (blue) and *p*-wave (red) neutrons. The arrow indicates the linear polarization of a  $\gamma$ -ray beam which is defined by the direction in which the electric field oscillates.

Figures 31 and 32 show schematic images of the ELIGANT-GN. The images show a complex array of  $\text{LaBr}_3\text{:Ce}$ , BC501A, and GS20 scintillation detectors. The sphere radius is 1.0 meters, the distance between the target and BC501A (gray) and GS20 (green) detectors. The  $\text{LaBr}_3\text{:Ce}$  detectors are shown in red. The energy resolution is discussed in relativistic kinematics in Sec. 3.1.3. The resolution for low-energy neutrons is 10% and 6.7% for the flight path of 1.0 m and 1.5 m, respectively.

The geometrical configurations of BC501A, GS29, and  $\text{LaBr}_3\text{:Ce}$  scintillation detectors are summarized in supplementary web material [84] (Tables 1, 2 and 3, respectively). The configuration is given by a Cartesian coordinate which is defined with the *z*-axis chosen along the beam direction, the *y*-axis chosen vertically and the *x*-axis horizontally. The number of detectors is 33 for BC501A, 29 for GS20, 17 for  $\text{LaBr}_3\text{:Ce}$  and 17 for  $\text{CeBr}_3$ .

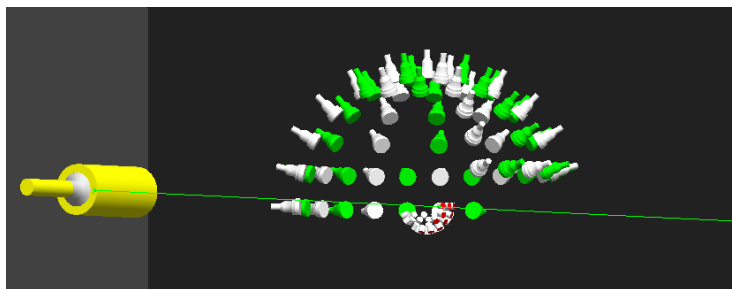


Fig. 31 - A side view of the ELIGANT-GN. The BC501A (liquid) scintillation detectors are shown in gray. The GS20 ( $^6\text{Li}$  glass) scintillation detectors are shown in green.

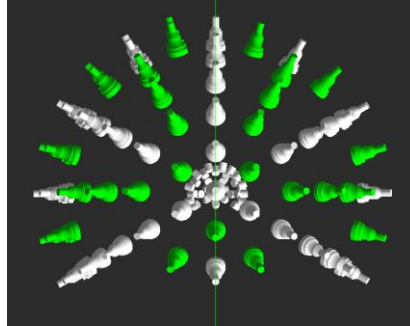


Fig. 32 - A top view of the ELIGANT-GN. The BC501A (liquid) scintillation detectors are shown in gray. The GS20 ( $^6\text{Li}$  glass) scintillation detectors are shown in green.

In neutron measurements with the ELIGANT-GN, we use the best monochromatic  $\gamma$ -ray beam with 0.2% energy spread in  $1\sigma$  (0.5% in FWHM) at a reduced intensity  $10^6$  cps consisting of 100Hz macro-bunches of  $\gamma$ -rays. The thinning operation of the linear accelerator is employed to pick up only the first micro-bunch out of 32 micro-bunches each in 16 ns apart that constitute a macro-bunch. A typical experimental condition for a study of PDR and MDR with the BC501A detector is given in Table 11. The count rate of experiments with the GS20 detector for low-energy neutrons is roughly smaller by one order of magnitude than that with the BC501A detector.

Table 11

A typical experimental condition for a study of PDR and MDR with the BC501A detector.

Target	$^{207}\text{Pb}$ : 1 g/cm $^2$
$\gamma$ -ray Beam	$10^6$ cps $\Delta E/E = 0.2\%$ $10^4$ per macro-bunch (100 Hz) 1 micro-bunch/macro-bunch
Cross section	$d\sigma/d\Omega = 10$ mb/sr [14]
BC501A	Flight path: 1m $\Delta\Omega = 0.0315$ sr
Intrinsic detection efficiency	$\epsilon \approx 50\%$
Count rate	0.45 cps/detector

It is noted that the energy resolution of the TOF measurement is comparable to that of the  $\gamma$ -ray beam. For example, in the case of irradiations of a nucleus having a neutron threshold 7.5 MeV with the best monochromatic  $\gamma$ -ray

beam of 8 MeV, PDR is excited in an energy-bin 40 keV in FWHM. The 500 keV neutron is measured by the TOF with energy resolution 50 keV (34 keV) for a flight path 1 m (1.5 m). This means that we can scan PDR and MDR with the TOF technique by using a  $\gamma$ -ray beam with a larger energy spread.

## 4. FEASIBILITY STUDY

### 4.1 Background radiation study

Simulations of a high energy  $\gamma$ -ray beam hitting a target have been performed by D. Filipescu (in Bucharest) and F. Rossi (in Milano) using GEANT4 libraries. The typical beam intensities are the ones given in [84].

Before discussing the background induced by the beam we want to remind that the typical time structure of the gamma beam in ELI-NP will be substantially different from that of NewSUBARU or HI $\gamma$ S as the following table shows:

Table 12

Comparison between ELI-NP, HI $\gamma$ S and NewSUBARU facilities in terms of intensity, bandwidth and time structure.

	ELI-NP	HI $\gamma$ S	NewSUBARU
Gamma rays per second	$8 \cdot 10^8$	$10^7$	$10^5 - 10^6$
Bandwidth (sigma)	< 0.5%	%	1 – 2%
Gamma rays per microshot	$< 2.6 \cdot 10^5$	1 – 3	2 · 10 <sup>-3</sup> per bunch (full bunch) 0.2 per bunch (single bunch) (5 – 1 per macroshot)
Distance between shots	16 ns	200 ns	2 ns – 396 ns (tunable)
Macrostructure	Yes	No	Yes
Macrostructure Time Structure	10 ms	-	50 $\mu$ s – 10 $\mu$ s

Practically, in ELI-NP it will be possible to have a shot of  $2.6 \cdot 10^5$  gamma rays (hitting the target within few ps) every 16 ns while in HI $\gamma$ S there are 1 – 3  $\gamma$ -rays every 200 ns. In the NewSUBARU facility, there are 198 electron beam bunches per circumference of the storage ring, 30 ps width, 2 ns apart at 500 MHz. Filling pattern can be changed from single bunch to full bunches. Macroscopic time structure can be made from 20 kHz to 100 kHz by laser operation.

In this discussion we assume that the beam dump does not emit any significant radiation which can be measured by the detectors around the target and that the beam has a well-defined energy and time structure.

The expected background which a detector array could measure can have two very different origins, one is the ELI-NP  $\gamma$ -ray beam hitting the target (we call it “beam-correlated background”), the second is not correlated with the beam or has lost any correlation with it (we call it “uncorrelated background”).

The “*beam-correlated background (atomic background)*” consists of the radiation ( $\gamma$ -rays, electrons, positrons) produced inside the target by the atomic electromagnetic interaction of the primary beam. It is mainly generated by Compton scattering or pair production mechanisms (which have cross sections orders of magnitude larger than the nuclear ones) of the primary beam  $\gamma$ -rays. Such kind of radiation cannot be separated or recognized from the one produced by the de-excitation of the nuclear collective states (which we are interested to measure in our physics cases) and blinds the detector in which it interacts. This is the major source of background in an ELI-NP measurement. The intensity of such background must be small enough not to blind any detector in each micro-shot.

This background must be understood and quantified using simulations and commissioning experiments. It implies also an accurate design of the detector setup and, in some cases, even a reduction of the beam intensity. In the next sections we accurately discuss the results of the simulations of this “beam-correlated background”.

There are, in addition, some experimental solutions and techniques which must be validated with simulations (not always discussed in this TDR) and tests that can be used to reduce its intensity, for example:

- 1) Placing an array of small, cheap scintillators with high efficiency and good timing properties in the forward part of the experimental setup might permit to identify and reject the 511 keV gamma rays produced by pair production inside the target;
- 2) A condition on the measured fold-sum energy selects only the events where a nuclear collective state is excited and then decays;
- 3) A well designed absorber (0 – 2 mm thick) attenuates the contribution of low energy gamma rays and reduces the energy of electrons and positrons;
- 4) A lateral shielding of the crystals prevents the scattering of gamma rays between detectors.

The “*beam-correlated background (neutrons)*” consists of the neutron radiation produced inside the target which, depending on the detectors, physics cases and beam structure, might be measured using Time of Flight or constitute background.

In some recent measurements the response of LaBr<sub>3</sub>:Ce large volume crystals to monochromatic neutrons of 14.1 MeV was measured and simulated [103]. It is clear from [103] that even though one could foresee some neutron induced background in the low energy part of the energy spectrum, there is a probability of  $10^{-5}$  (which should be scaled by an additional large factor because of

the time gate) for a neutron to produce background at high energy. Therefore, when not measured, neutron background is expected to be practically negligible.

The “*uncorrelated background*” consists on the radiation which is not correlated with the beam (as for example: cosmic rays, natural/internal radiation, etc.) or radiation which has lost any correlation with the beam (as for example: thermal or low energy neutrons, wall scattered gamma rays, etc.).

If the detectors have good time properties ( $\Delta T < 1$  ns) such kind of radiation can be effectively identified and rejected using the Time of Flight (TOF) technique. We do not expect any major contribution in the measured energy spectra as the uncorrelated background events can be acquired only as a random coincidence. There are, in fact 3200, beam micro-shots every second, a coincidence condition of 1 ns with the beam reduces the intensity of such background (which is expected to be rather constant in time) of a factor of approximately  $3 \cdot 10^5$ . In addition, what remains could simply be subtracted from the measured energy spectra. Therefore, also this source of background is practically negligible.

In the following sub-sections the results of the simulations that were performed to understand the “*beam correlated background (atomic background)*” is discussed for the  $\text{LaBr}_3:\text{Ce}$  array and count rate estimation for the ground state decay of the GDR-PDR-MDR is reported.

As shown, the  $\gamma$ -rays detectors might partially or totally be blinded by the background radiations. However we do not think, for the proposed target thicknesses, that this kind of background seriously affect the neutron detectors in fact:

- 1)  $^3\text{He}$  detectors of the ELI-GANT-TN have very low sensitivity to gamma rays and are able to easily discriminate gamma rays by pulse height. We use a minimum amount of target materials,  $1 \text{ mg/cm}^2$ , taking advantage of the full intensity of the  $\gamma$ -ray beam in the  $p$ -process study. As a result, no serious pile up due to gamma background is foreseen;
- 2) Liquid and  $^6\text{Li}$  glass scintillators of the ELI-GANT-GN can easily identify and reject prompt gammas because of their excellent time properties in the TOF measurement. Neutron events are identified by the pulse shape analysis and their arrival times which are much later than those of  $\gamma$ -rays. In addition, only the first micro-bunch of the macro-bunch is used in the TOF measurement. Therefore, no pile up due to gamma background is foreseen.

A detailed study of optimum experimental conditions including background gammas and electrons of target origin for thermal and fast neutron detection is however underway by Monte Carlo simulations.

In the first sub-section of the chapter we therefore present the interactions of the beam inside the target, calculations have been performed for different targets and the results are reported. In this sub-section we discuss the energy, angular distribution and the nature of the emitted radiations. In the second sub-section we discuss the background energy spectra and we present the spectra that detectors

placed at different angles are expected to measure. An optimal design for the  $\gamma$ -rays detector setup and of beam intensity is also discussed.

#### 4.1.1 Beam correlated background (atomic background) – emission from target

The simulated beam spot on target is circular with 2 mm diameter (see left panel of Figure 33) and the target has the shape of a parallelepiped with  $x$  and  $y$  sides of 2 cm and thickness  $d$  (see right panel of Figure 33). No target holder or scattering chamber have been inserted in the calculations. The simulations have been performed using 9 MeV gamma rays, different target thicknesses and materials. In particular we discuss targets of Pb, Ni and Sn. Table 13 summarizes, for the Pb case, the relation between the thicknesses expressed in  $\text{g}/\text{cm}^2$  and those expressed in micrometers.

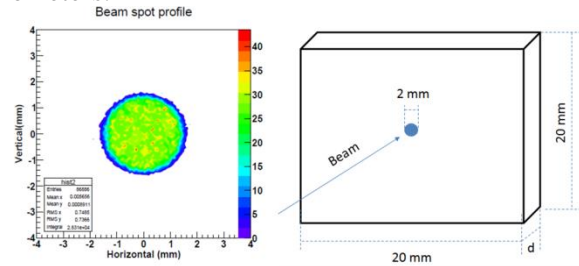


Fig. 33 - Beam spot profile used in the simulations(left panel). Drawing of the target and beam spot used in the simulations (right panel).

Table 13

The thicknesses of a Pb target expressed in  $\text{g}/\text{cm}^2$  and in micrometers are listed in column one and two, respectively.

Thickness ( $\text{g}/\text{cm}^2$ )	Thickness ( $\mu\text{m}$ )
0.05	44.1
0.1	88.2
0.3	264.6
1.0	881.8

As previously mentioned, the primary gamma beam of ELI-NP interacts with the atoms of the target mainly through Compton Scattering and Pair Production. The probability that one  $\gamma$ -ray of ELI-NP beam interacts electromagnetically with one atom of the target linearly increase with the target thicknesses and linearly scales with the atomic number of the target material (see Table 14 and Figure 34). It is possible to have a simple parameterization of such

probability with the target thickness  $d$  in  $\text{g}/\text{cm}^2$  and atomic number  $Z$  using the relation  $P(\%) = d \cdot (z \cdot 0.316 + 2.2)$ .

In the case of the Pb target there is approximately 5% probability per  $\text{g}/\text{cm}^2$  thickness for a 9 MeV gamma ray to interact with the atoms inside the target. In other words, in a micro-shot of  $2.6 \cdot 10^5$  gamma rays, arriving within few ps on a  $1 \text{ g}/\text{cm}^2$  Pb target, approximately 13000 gamma rays interact producing background. Alternatively, all the gamma rays of the beam micro-shot interact with the atoms in a target of  $20 \text{ g}/\text{cm}^2$  (i.e. in approximately 2 cm of lead). In section 4.2 the expected rate of  $\gamma$ -rays coming from the decay of GDR-PDR-MDR are calculated.

Table 14

The probability of interaction (%) for a 9 MeV  $\gamma$ -ray with the atoms of different target materials. Column one lists the target thickness while the second to fourth columns list the probability for Pb, Sn and Ni target, respectively.

Thickness ( $\text{g}/\text{cm}^2$ )	Pb	Sn	Ni
0.05	0.22	0.19	0.16
0.1	0.48	0.38	0.32
0.3	1.43	1.13	0.94
1.0	4.7	3.72	3.11

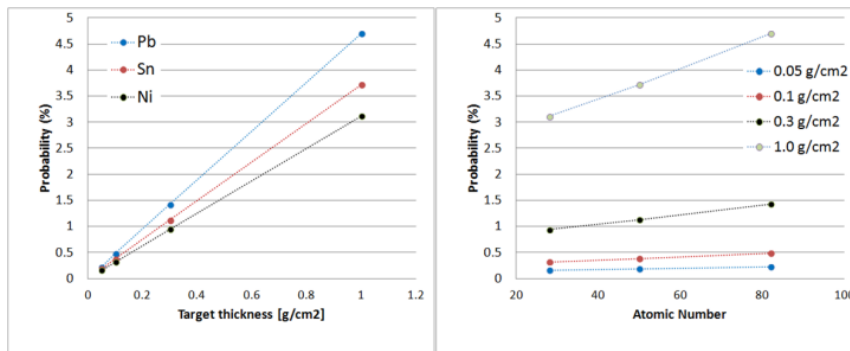


Fig. 34 - The dependence of the probability of electromagnetic interaction of one 9 MeV gamma rays with the atoms of the target. The values are plotted vs. the target thickness (left panel) and vs. the target atomic number (right panel).

As expected from general arguments, the most probable interaction mechanism is pair production (72%) while Compton scattering accounts for 27% of the interactions (see Table 18). Approximately 1% of the gamma rays undergo Rayleigh scattering which, however, neither deposits energy inside the target nor significantly changes the incident  $\gamma$ -ray direction. These values do not change with the target thicknesses (see columns 1 – 3 of Table 15). One important feature to

notice (see column 4 of Table 15) is that the number of positrons emitted (expressed as a percentage of the gamma rays of ELI-NP beam which interact with the atoms of the target) decreases as the target thickness increases. This can be understood as positrons can be fully stopped (and annihilate) inside the target. In fact, in pair production, even though the linear momentum conservation makes the positron and electron forward focused, their trajectory in matter are not straight and therefore they could be stopped inside a  $2 \times 2 \times d$  cm<sup>3</sup> target. A similar behavior happens also for the electrons produced in Compton scattering, in this case, however, the energy and angular distribution is different.

Table 15

The probability for a 9 MeV  $\gamma$ -ray to undergo Pair Production (second column) or Compton interaction (third column) for different values of the target thicknesses. The column from four to six lists (relative to the number of incident gamma rays) the percentage of particles which exit from the target.

Thickness (g/cm <sup>2</sup> )	Pair production [%]	Compton [%]	Positrons [%]	Electrons [%]	Gamma rays [%]
0.05	71	27	71	101	35
0.1	72	27	70	101	41
0.3	72	27	66	96	65
1.0	72	27	48	75	135

Even though simulations show that the probability of interaction scales linearly with the target thicknesses, the trend is not anymore linear when the number of background particles emitted (electrons, positrons and gamma rays) are plotted vs the target thickness. The effect is mainly due to the fact that, as the target thickness increases, an increasing number of positrons are stopped inside the target. When they annihilate, two gamma rays of 511 keV are produced increasing in a nonlinear way the background intensity. For the estimation of the background it is therefore not correct to simply scale the results on the target thicknesses.

The simulations have shown that the beam produces a large amount of background radiation from Compton Scattering and pair production. This radiation is mainly forward focused (see Table 16). The black points of Figure 35 show the angular distribution (integrated on the angle  $\varphi$ ) of the background radiation. As expected, the forward background radiation is more than 10 times stronger than the backward one. In the plot, the minimum at 90° is produced by the shadow effect that the target finite size produces. As shown in the next session, the backward background is mainly composed by 511 keV gamma rays produced by the annihilation of positrons inside the target.

Table 16  
The Compton backscattering ( $90^\circ < \theta < 180^\circ$ ) probability for gamma rays of different energies.

$\gamma$ -ray energy	Compton backscatter probability ( $90 - 180^\circ$ )
60 keV	43%
511 keV	25%
1.4 MeV	17%
10 MeV	7%

In this section we have analyzed what happens when the ELI-NP gamma beam hits a target of various thicknesses and materials. In the next section, the nature, the energy and angular distribution of the particles arriving inside a 3"×3" detector is discussed.

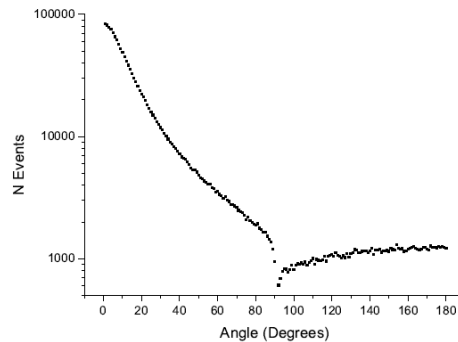


Fig. 35 - The number of target emitted background particles integrated on the angle  $\varphi$  produced by a beam of  $10^8$   $\gamma$ -rays focused on a Pb target 0.1 g/cm<sup>2</sup> thick.

#### 4.1.2 Beam correlated background (atomic background) – simulated energy spectra in ELI-GANT-GN LaBr<sub>3</sub>:Ce detectors

In this section is calculated the background energy spectrum measured in a 3"×3" LaBr<sub>3</sub>:Ce detector. This section follows the discussion of the previous section where the beam induced particles emitted from the target were calculated. Only the atomic Photoelectric, Compton and Pair Production mechanism are taken into account in the simulations. These events constitute only background and are of no interest for the physics cases.

The simulations of the gamma correlated background have been performed by D. Filipescu using GEANT4 libraries. A total of  $10^8$  monochromatic  $\gamma$ -rays have

been fired on a target of Ni, Sn or Pb of variable thicknesses. The simulated detector array consists of 32 LaBr<sub>3</sub>:Ce detectors placed at 25 cm from the target. The detectors have been arranged in 5 rings (see Table 17) in a symmetrical geometry (see Figure 36). We have decided to cover the whole solid angle to better understand the angular behavior of the beam correlated background.

Table 17

The geometry used in the simulations. The first column reports the angle of the detector rings (0 degrees is the direction of the beam). The second column reports the number of detectors in each ring.

Angle (degrees)	Number of detectors
143	4
117	8
90	8
63	8
37	4

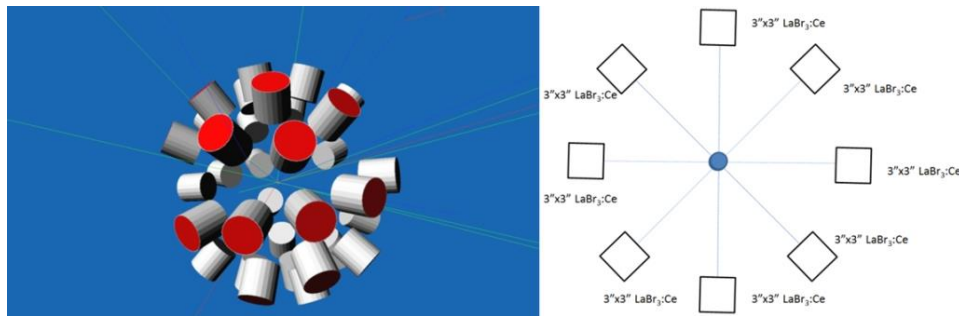


Fig. 36 - The geometry used in the simulations. Left Panel: a 3D drawing of the system. Right Panel: a cut of the 3D plot at 90°. Note that each crystal faces another identical crystal.

It is interesting to notice that, in the simulated geometry, each detector faces a second detector. Therefore the  $\gamma$ -rays backscattered in one crystal enter in the opposite detector or the two 511 keV  $\gamma$ -rays produced in the annihilation of the positron inside the target either enter in two opposite detectors or in none.

The plot shown in Figure 37 shows the background  $\gamma$ -ray spectra measured in one detector located at different angles (from 37° up to 143° degrees). The simulation has been performed using a beam of  $10^8$   $\gamma$ -rays of 9 MeV which hit a 1 mm thick Pb target. The beam pointed to  $\theta = 0^\circ$ . The spectra in Figure 38 show instead the comparison between the intensity of the measured background using 1 mm and 88  $\mu\text{m}$  thick Pb target. The simulations are relative to a micro-shot, namely using a beam of  $10^4$  gamma rays and a 3"×3" LaBr<sub>3</sub>:Ce detector placed at

117° relative to the beam direction. In this case the values in the y-axis correspond to the probability to measure that background  $\gamma$ -ray energy.

Note from Figure 37 that the background does not scale linearly with the target thickness. In average, the amount of measured background produced increases by a factor ranging from 15 to 30 (depending on the energy) when the target thickness increases from 88  $\mu\text{m}$  to 1 mm (1.000/0.088, namely a factor of approximately 12).

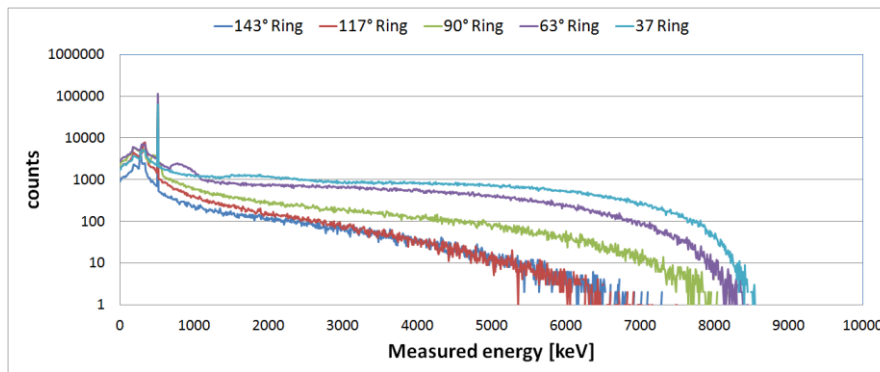


Fig. 37 - The background energy spectrum that a 3"×3" LaBr<sub>3</sub>:Ce detector would measure when a beam of  $10^8$   $\gamma$ -rays of 9 MeV hit a Pb target 1 mm thick. The detectors are encapsulated in 1 mm thick Al housing and air is present in the simulations. No absorber was used.

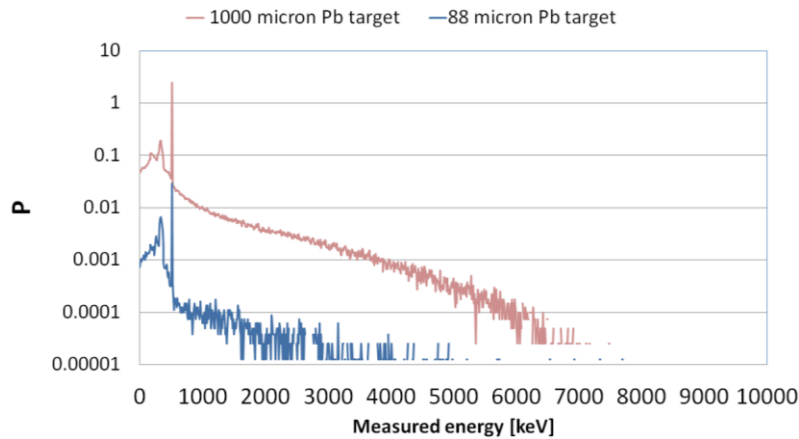


Fig. 38 - The probability  $P(E_\gamma)$  to measure a background  $\gamma$ -ray of energy  $E_\gamma$  simulated for a 3" x 3" LaBr<sub>3</sub>:Ce detector at 117° when a beam of  $10^4$   $\gamma$ -rays of 9 MeV hit a Pb target thick 1 or 0.088 mm. The detector is encapsulated in 1 mm thick Al housing and air is present in the simulations. No absorber was used.

The figures in Table 18 summarize for the different detector angles the intensity of the gamma background for different values of  $\gamma$ -rays energy or threshold. The numbers are relative of a Pb target of 88  $\mu\text{m}$ , a beam intensity of  $10^4$  gamma rays per micro-shot (approximately  $3 \cdot 10^7$   $\gamma$ -ray per second). No absorber, detector housing or scattering chamber is present in the simulations.

A thickness of the order of 0.1  $\text{g}/\text{cm}^2$  does not produce a strong gamma correlated background while a thickness of 1 mm produces a background which would blind all the detectors.

Table 18

The integral of the energy spectrum using a Pb target of 88  $\mu\text{m}$  thick and a beam intensity of  $10^4$  gamma rays per micro-shot. The first column shows the angle of the LaBr<sub>3</sub>:Ce detector while columns from 2 to 5 display the probability to measure, in a single micro-shot, a background  $\gamma$ -ray. Detectors are encapsulated in 1 mm thick Al housing and air is present in the simulations. No absorber was used.

Angle	$P(E_\gamma) > 50 \text{ keV}$	$P(E_\gamma) > 2 \text{ MeV}$	$P(E_\gamma) = 511 \text{ keV}$	$P(E_\gamma) < 511 \text{ keV}$
143°	13%	0.6%	3.0%	8%
117°	13%	0.6%	3.0%	8%
90°	24%	1.6%	5.2%	13%
63°	38%	6.5%	5.0%	12%
37°	134%	60%	6.6%	22%

The simulations show that the amount of background does not strongly depend on the energy of ELI-NP gamma beam. In fact, Figure 39 shows that for a Pb target 1 mm thick the amount of beam correlated background is concentrated at low energy and practically independent from the original beam energy. For backward angles, the highest energy deposited by background radiation is much lower than the beam energy.

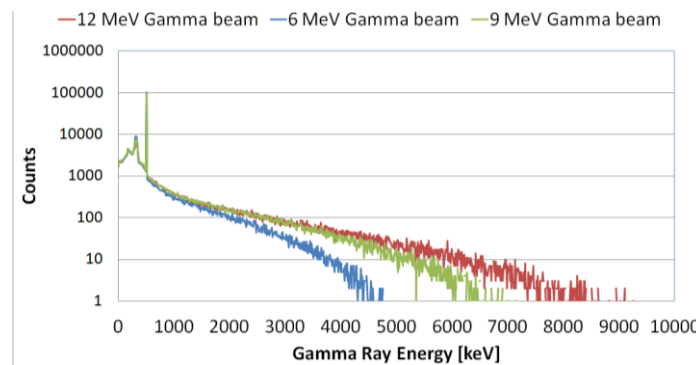


Fig. 39 - The energy spectra simulated if a beam  $10^8$   $\gamma$ -rays of 6, 9 and 12 MeV hit a 1 mm thick Pb target. Detectors are encapsulated in 1 mm thick Al housing and air is present in the simulations. No absorber was used. The detector is located at 117° relative to the beam direction.

The plots and tables previously displayed can be summarized in the following statements:

- 1) In the case of a 9 MeV beam, backward detectors and 88  $\mu\text{m}$  Pb target, no background event practically exceeds 4 MeV and there is only 13% probability that a detector is blinded from the background;
- 2) The detectors in forward positions see much more background than those located backwards;
- 3) It is possible to observe (see Figure 37) a “bump” moving from 300 keV (at  $147^\circ$ ) up to 2 MeV ( $37^\circ$ ), this is due to the Compton scattered  $\gamma$ -rays;
- 4) At backward angles the maximum energy of the background radiation energy is some MeV lower than the energy of the incident beam. This means that high energy  $\gamma$ -rays from the decay of collective nuclear states (i.e. the ground state decay of the GDR-PDR-MDR) do not have any kind of background;
- 5) The 511 keV peak is extremely strong and it is the major source of background in the case of detectors located backwards. This could help in the background reduction for backward detectors;
- 6) There is a significant contribution from the backscattered 511 keV  $\gamma$ -rays from the opposite detector;
- 7) The amount of beam correlated background does not significantly depend on the beam energy.

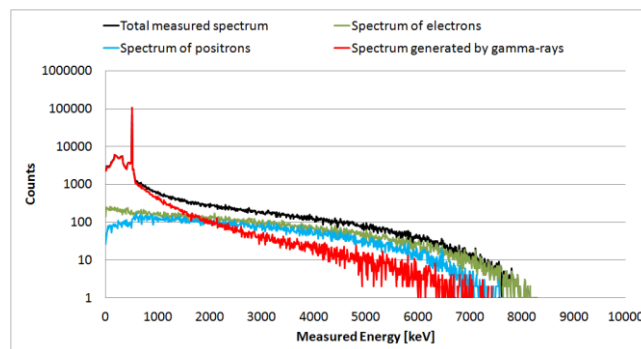


Fig. 40 - The energy spectrum deposited by  $\gamma$ -rays, electrons and positrons in a detector placed at  $90^\circ$  simulated using  $10^8$   $\gamma$ -rays of 9 MeV hitting a 1 mm thick Pb target. Detectors are encapsulated in 1 mm thick Al housing and air is present in the simulations. No absorber was used.

For a better understanding of the nature of the beam correlated background, the following simulated spectra have been additionally produced ( $10^8$   $\gamma$ -rays of 9 MeV hit a 1 mm thick Pb, LaBr<sub>3</sub>:Ce detector are placed at  $90^\circ$ ):

- 1) In Figure 40 simulations distinguish between the contribution that different particles have in the background spectrum;

- 2) In Figure 41 simulations evaluate the effect of an absorber placed in front of the detector. A multilayer absorber composed of 1 mm Pb, 0.5 mm Cd and 0.5 mm Cu thick plates was used for this study. Also the 1 mm thick Al housing was present in this simulation;
- 3) In Figure 42 simulations evaluate the background intensity for different target materials. The cases of 1 mm thick Pd, Sn and Ni targets were simulated.

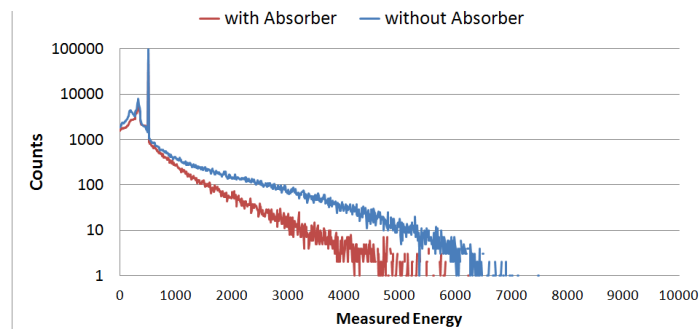


Fig. 41 - The energy spectrum with and without a 2 mm thick absorber. The spectra are relative to a detector placed at  $90^\circ$  with using  $10^8$   $\gamma$ -rays of 9 MeV hitting a Pb target 1 mm thick, Detectors are encapsulated in 1 mm thick Al housing and air is present in the simulations.

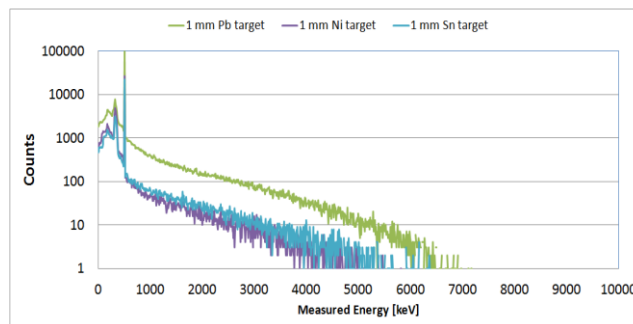


Fig. 42 - Comparison between the background energy spectrum with 1 mm thick Pb, Ni and Sn target. The spectra are relative to a detector placed at  $90^\circ$  using  $10^8$   $\gamma$ -rays of 9 MeV. Detectors are encapsulated in 1 mm thick Al housing and air is present in the simulations. No absorber was used.

From the last three plots some additional conclusion can be drawn:

- 1) The  $\gamma$ -rays mainly produce low energy background;
- 2) Electrons produce the high energy background;
- 3) Positrons have a similar but less intense spectrum as produced by pair production only;

- 4) An absorber can significantly reduce the energy of the measured electrons and positrons. A reduction of approximately 25% in the total background has been obtained in the simulations;
- 5) The total background events in first approximation scale with the product between the atomic number and the target density.

In summary, radiation coming from the atomic interaction of the beam with the target produces a beam correlated background which could completely blind a gamma detector array. The key factor to reduce such background is to use a target thickness which, for Pb, does not exceed  $0.1 \text{ g/cm}^2$ .

In addition, detector placed in a backward geometry at 25 cm from the target, frontal and lateral absorbers and an excellent time resolution will additionally reduce the importance of such background radiation.

#### 4.2 Count rate estimate for the ground state $\gamma$ -decay of the GDR-PDR-MDR

The previous sections have shown that a 9 MeV beam with the intensity of  $10^4$   $\gamma$ -rays per micro-shot ( $3.2 \cdot 10^7$   $\gamma$ -rays per second) and a Pb target of  $0.1 \text{ g/cm}^2$  do not produce a beam correlated background with energy larger than 4 MeV (as can be seen in Figure 38 and Table 21). In addition, a 1ns gate on TOF spectra eliminates most of the beam non correlated background. It is therefore possible the estimation of the count rate for an experiment focused on the measurement of the gamma ground state decay of the GDR-PDR-MDR.

The basic numbers needed to calculate the expected rate of events starts from the very conservative hypothesis to have a beam of  $10^4$  polarized gamma rays which arrive within a few ps on the target and an array of 36  $3'' \times 3''$  LaBr<sub>3</sub>:Ce detectors. Below there is a very simple estimation of count rates for ELI-NP beam energy of 10 MeV. The rates are higher for lower beam energy while background remains the same. We assume a 10 MeV maximum energy  $\gamma$ -ray beam of 0.2% rms bandwidth,  $10^4$  photons per micro-bunch and 3200 micro-bunches and a <sup>208</sup>Pb with a thickness of 88 micron namely  $0.1 \text{ g/cm}^2$ . The GDR-PDR-MDR states have a total cross section which ranges from 10 to 300 mb (between 7-12 MeV). The branching ratio is not known exactly but in literature one can find values around 2%.

Therefore one can estimate that  $3.2 \cdot 10^7$  photons will hit the target in one second, 0.29 target nuclei will be excited to a GDR collective state per micro-shot, meaning 931.2 nuclei per second. Assuming a 2% value for the  $\gamma$ -decay branching ratio, 18.6 nuclei excited to a GDR state will decay by a  $\gamma$  transition to the ground state per second. We can compute the expected count rate is for 17 LaBr<sub>3</sub> and 17 CeBr<sub>3</sub> detectors. The solid angle for one  $3'' \times 3''$  detector placed at 25 cm from the target point is of 0.58% of  $4\pi$  and the estimated detection efficiency is of 1.5% for 10 MeV  $\gamma$ -rays. Therefore we can expect a 0.27 counts/second rate of full energy detected  $\gamma$ -ray transitions to the ground state, meaning a necessary of about 0.5

hours time interval for acquiring 500 counts in the full energy peak. Therefore, the time needed to scan a 1 MeV energy window is of 10.2 hours.

There are additional points which make this type of experiment unique and feasible in a facility like ELI-NP. The only critical aspect concerns the number of detectors which provide the necessary detection efficiency.

- 1) Simulations have shown that there is no background radiation coming from the target starting from 2 MeV below beam energy. Therefore  $\gamma$  decay to the ground state is measured without such background. The critical feature is that the energy resolution of the detector must separate the full energy peak from the first escape one;
- 2) In an experiment focused to measure scattered  $\gamma$ -rays, the resolution in energy of the scan is not given by the  $\gamma$ -ray detector energy resolution (only the Full Energy Peak and the 1st Escape Peak need to be separated) but only by the beam bandwidth;
- 3) As the experiment is focused to measure scattered gamma rays, for a fixed beam energy, only their number is important and need to be measured. Therefore, only few hundred counts in the full energy peak will be sufficient. In addition, also the events present in the first escape peak could be used reducing the needed beam time;
- 4) As the experiment need to scan with high resolution (i.e. 100 keV) the energy window between 7 – 12 MeV (approximately 50 different beam energies) it must be possible to change the beam energy very rapidly (few minutes). This is a feature provided by ELI-NP beam;
- 5) In case that stable targets like  $^{208}\text{Pb}$  are needed, the intensity of the beam is not a potential issue as one can compensate using a thicker target. The limit is that the detector should not be blinded by the electromagnetic scattering of the beam on the target atoms. A small beam bandwidth is the critical issue;
- 6) As the distance between micro-shots is 16 ns one should use a  $\gamma$ -ray detector with a time resolution much smaller than 16 ns.

#### 4.2.1 Simulation of $^{208}\text{Pb}$ experiment

The numbers listed in section 4.2 have been used to simulate the outcome of approximately one minute of beam time. In the simulated experiment we have used a target of 0.1 g/cm<sup>2</sup> (88 micron thickness) of  $^{208}\text{Pb}$  and an ELI-NP beam intensity of  $10^4$   $\gamma$ -rays of 9 MeV per micro-shot. In this simulation the electromagnetic background was taken into account in a complete way, the induced neutron background was not considered but we think that (as discussed in the previous sections) it should not degrade the measured spectra because a 1 ns time gate on the time spectrum should eliminate it. It is important to evidence that, in the simulations, time information was not considered.

As the simulation requires a huge amount of CPU resources we have performed separately the simulation of the electromagnetic background and those of the gamma decay of the GDR-PDR-MDR resonance. In fact, Figure 43 consists in two spectra. The black spectrum shows the electromagnetic background recorded by all the  $\text{LaBr}_3:\text{Ce}$  detectors placed backwards. In this spectrum the energy resolution of the detectors has been considered. A huge background mainly concentrated below 1 MeV is clearly visible. No background is evident for energy larger than 3 MeV. The red spectrum is the one associate to the  $\gamma$ -decay of the GDR. In this spectrum the energy resolution was not inserted to evidence, in a clear way, the full energy peaks events.

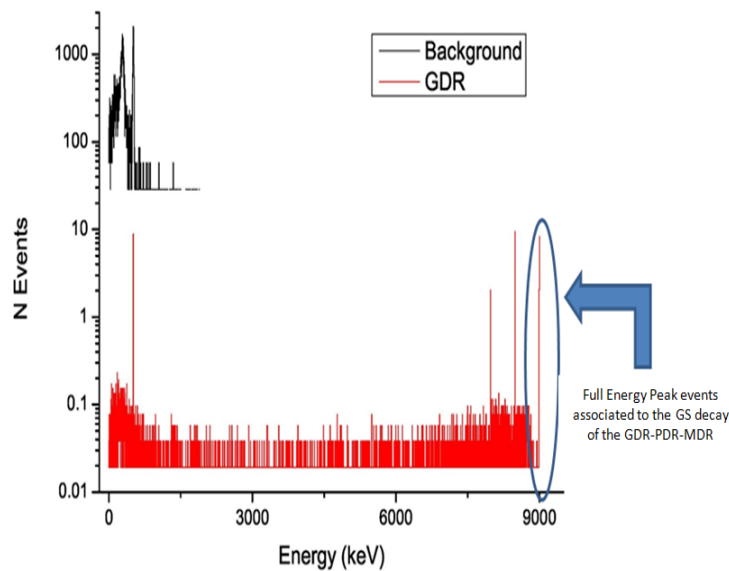


Fig. 43 - Simulation of one minute of data-taking using a beam of 9 MeV  $\gamma$ -rays on a  $0.1 \text{ g/cm}^2$  thick target of  $^{208}\text{P}$ . In black is indicated the electromagnetic background while in red the events associated to the gamma ground state decay of the Giant Dipole Resonance. The intensity of the beam is  $10^4$   $\gamma$ -rays per micro-shot.

## 5. SPECIFIC NEEDS AND UTILITIES, TRANSVERSAL NEEDS

### 5.1 Infrastructure needed from ELI-NP

When designing the GANT experimental setups and planning the experiments that are intended to be performed at the ELI-NP gamma ray source, it is essential to foresee all the needed infrastructure within ELI-NP, namely: collimators and shielding materials, electrical power of high stability, mechanics of the detector support in the beam-line, movable table allowing a remote control of the detector positioning in the beam axis, cable ducts, disk storage, fast internet transmission lines, central CPU for off-line data processing, beam-energy profile and beam-intensity information to be integrated into the DAQ, etc. Concerning vacuum beam line, we have to mention that both experiments will use the vacuum beam line of the gamma beam experiments system, thus we will have to take care of the integration of the GANT experiments into the foreseen vacuum beamline.

### 5.2 Beam flux measurement system

The experiments proposed by the GANT workgroup aim to measure absolute reaction cross sections. Therefore, a method for determining with a good degree of precision the incident number of photons on the target is crucial for the feasibility of the GANT experiments.

Presently, the beam flux measurements are performed by various methods at the existing  $\gamma$ -ray beam production facilities, depending on the beam characteristics specific to each gamma source: intensity, energy resolution, time structure. At the HI $\gamma$ S facility are being developed three independent beam flux measurement methods based on placing in beam a set of attenuators in front of a high efficiency NaI detector, on the measurement of Compton scattered gamma rays on different materials, or monitor the photoneutron CS on isotopes for which the  $(\gamma,n)$  cross section is known with a high degree of precision. At the NewSUBARU facility, the beam monitor consists of a large volume NaI detector placed directly in beam, with no additional attenuators besides the irradiated target itself.

We will make here a short presentation of two methods proposed to be used at ELI-NP.

### 5.2.1 $d(\gamma,n)$ monitor reaction

We propose an intensity and polarization monitor based on the  $d(\gamma,n)p$ . The photodisintegration of the deuteron is one of the most-studied photonuclear reactions. Significant experimental and theoretical work has been done to better understand the differential cross section and the polarization asymmetry of the outgoing neutrons when using a linearly-polarized  $\gamma$ -ray beam. This reaction is typically used as a benchmark for studies of the beam polarization and intensity for  $\gamma$ -ray beams below 20 MeV. The threshold for photodisintegration of the deuteron is 2.23 MeV. In order to have significant energies in the neutrons, this reaction can be used at energies of 2.5 MeV and above.

This technique can be reliably used at ELI-NP above 4 MeV. The only major consideration is that the count rate must be limited in order to ensure good Pulse Shape Discrimination (PSD) performance. With microbunches every 16 ns, we estimate that there should be a gap of at least 5 microbunches between detector hits for good PSD performance. A conservative estimate would be to run the detectors at an average beam-related trigger rate of approximately 200 Hz. The neutron detectors will be made of NE213-type liquid scintillator. These detectors have been well-studied and characterized at facilities around the world. They will be 12.7 cm in diameter and they will be placed at approximately 50 cm from the target.

### 5.2.2 Fission monitor reaction

A fission chamber will be used for absolute photon flux measurements in the high-energy experimental halls (E7, E8). The fission chamber is shown described in more detail in the Gamma Beam Delivery and Diagnostics TDR. The fissionable material ( $^{235}\text{U}$ ,  $^{238}\text{U}$ ,  $^{239}\text{Pu}$ ) is deposited with an active spot of 10 mm on a 0.2 mm thick, 20 mm diameter aluminum or stainless steel backing.

The count rates for  $^{235}\text{U}$ ,  $^{238}\text{U}$  and  $^{239}\text{Pu}$  have been calculated. The analytical calculations are based on 100 fissions/s recorded by the fission chamber with  $^{235}\text{U}$  at maximum cross section (330 mb at 14 MeV). The resulting actinide deposit is 200  $\mu\text{g}/\text{cm}^2$ . This rate gives a 1% uncertainty in under two minutes between 10 and 16 MeV and around 20 minutes in the remaining range. We are exploring the possibility of operating the fission chamber at higher detection rates in pulsed mode or even in current mode.

Beam intensity measurements with this device should be accurate at the 2% level since the cross sections for this reaction are very well known and the instrument efficiency is almost 100%.

### 5.3 Requirement of thinning the micro-pulses time structure of the gamma beam

As it has been discussed in Section 3, the GANT array consisting of liquid scintillation neutron detectors and  $\text{LaBr}_3\text{:Ce}$  scintillation detectors will be dedicated to the investigation of the pygmy dipole resonance and spin-flip M1 resonances involving detection of high energy gamma rays and the neutron TOF technique.

We expect to detect *s*- and *p*-wave neutrons with fast liquid scintillator detectors placed at about 1.5 m in a backward hemisphere. In such measurements, it is important to measure the angular distribution of neutrons, but in addition, if the neutron energy is measured, we could measure the angular distribution of neutrons in different energy bins.

The main issue is that under the expected time structure of the  $\gamma$ -ray beam that will be available at ELI-NP, n-TOF measurements are not feasible for the following reason: the time of flight of 1 MeV (10 keV) neutrons in 1.5 m flight path is 108 ns (1080 ns). Thus differently from gammas which travel at  $v = c$ , the neutrons TOF changes a lot depending on neutron energy. Therefore fast neutrons from late bursts arrive before slow neutrons from early bursts. This will destroy any energy measurement using TOF unless beam time structure would be changed. In other words, we need to thin out the 32 micropulses which come every 16 ns during a macropulse.

TOF technique requires at least the possibility to select only a micropulse per macropulse. In this case the total gamma beam intensity will be sacrificed of course.

The additional feature of selecting only certain micropulses in every macropulse (eg. 1<sup>st</sup>, 10<sup>th</sup>, 30<sup>th</sup>...) will provide us large flexibility in choosing the available energy range of emitted neutrons which can be correlated also with neutron energy resolution accordingly by having the possibility to adjust mechanically the distance between the neutron detectors and the interaction point. Thus, depending on the experimental conditions required by the different physics cases we will be able to achieve the optimum gamma beam intensity.

#### **5.4 Requirement of circular polarization and of switching the plane of linear polarization of the gamma beam**

As it is already foreseen, the gamma beam that will be provided at ELI-NP facility is expected to be almost 100% plane polarized. This is a very important feature that will allow us to perform experiments in which the behavior of nuclear force at space inversion is tested.

In such experiments, for example, the electric or magnetic character of the gamma rays emitted by certain excited states of a nucleus will allow the measurement of parities or to check the parity violation. Thus, due to the characteristic angular distribution of magnetic or electric dipolar transitions, corresponding gamma photons will be preferentially emitted within the polarization plane or in the plane perpendicular to the polarization plane (see Figure 54). Also, the emission of  $p$ -wave neutrons is strongly correlated with the plane of linear polarization (see Figure 49 from Ref. [84]).

As it was already presented, such measurements are foreseen to be performed with the ELIGANT-GN detection system. These sensitive measurements have to be performed with high caution, and prior to any measurement, the detection system has to be carefully calibrated in order to check for and to characterize any angular asymmetry, especially the azimuthal asymmetry.

We require a circular polarized gamma beam to simulate an unpolarized beam, making such calibration possible. In such experiments, one will need a certain amount of time allocated exclusively for calibration of resolving power of the detection system.

We also require having the possibility to switch the polarization plane during the experiment. This feature will be very useful especially if the switching period is much shorter than the total time needed to perform the experiment (the order of minutes). In this case, all the acquired data is useful for both calibration and physics case purposes, and in addition time dependence and stability of the calibration may be checked.

## **6. COLLABORATIONS**

Professor Franco Camera

*University of Milano, Department of Physics, Via Celoria 16, Milano 1-20133, Italy.*

*Istituto Nazionale di Fisica Nucleare (INFN), section of Milano, Via Celoria 16, Milano 20133, Italy.*

There are a number of LaBr<sub>3</sub>:Ce detectors of different sizes (for example in Milano we have 10 detectors of 3.5"×8" and others of 3"×3" size are at various places) that could be used with the ELI detector systems if specific experimental campaigns are proposed and then arranged.

Since we have the experience to have used LaBr<sub>3</sub> detectors to study collective modes in different experimental campaigns and collaborations (see e.g. GSI and RIKEN) we expect to perform similar types of campaigns also at ELI-NP. The availability of a good number of detectors belonging to a permanent set up at ELI will attract other users for experiments and in some cases to make the detection system more powerful, although for a limited amount of time. The presence of a well-built set up at ELI including a good number of detectors (representing the core of detection system) will act surely as catalyzer.

Concerning manpower, from his role of co-convener F. Camera will be engaged in contributing to the project together with the electronics workshop of Milano. In addition, it is expected to have an undergraduate or a graduate student working on the ELIGANT project, depending on the flow of students in Milano in this field. Furthermore there is an application ongoing to have one post-doctoral fellowship on this project focusing on the physics case, simulations, and R&D on detectors.

Professor Hiroaki Utsunomiya

*Department of Physics, Konan University, 8-9-1, Okamoto, Higashinada, Kobe 658-85-1, Japan.*

*The Center for Nuclear Study, University of Tokyo, 2-1 Hirosawa, Wako, Saitama 351-0198, Japan.*

Professor Vladimir Varlamov

*Lomonosov Moscow State University, Skobeltsyn Institute of Nuclear Physics, Leninskie gory, 1(2), 119991, Moscow, Russia.*

Regarding photoneutron cross section measurements with moderator-based 4 $\pi$  neutron detectors in the ELI-NP project, it is foreseen a solid collaboration with the Konan University based on the MoUs signed by IFIN-HH, Konan University and Lomonosov Moscow State University. Some extra <sup>3</sup>He counters with the same specification proposed in this TDR may be temporarily available for specific experiments to be setup within the collaboration.

The collaboration with the Konan University and the Lomonosov Moscow State University (MSU) was initiated with the aim of neutron multiplicity sorting with a flat-efficiency detector proposed in the TDR for the ELI-NP project. A beam

time for  $^{209}\text{Bi}(\gamma, xn)$  cross section measurements with  $x = 1 - 3$  was scheduled in July 2015 at the NewSUBARU facility. Ioana Gheorghe of the ELI-NP and Sergey Belyshev of the MSU will joined the experiment at the NewSUBARU. Ioana Gheorghe stayed in Kobe (Japan) as a visiting researcher of the Konan University for three months to prepare and perform the experiment, which will be devoted to her PhD thesis.

Regarding the neutron detection with liquid scintillation (BC501) detectors, a possible collaboration with RCNP, Osaka University is envisaged, where a detector system similar to the EDEN has been developed by Prof. Mamoru Fujiwara. However, the availability of the extra BC501 detectors from such collaboration depends on the detector conditions, which need to be carefully checked beforehand.

Professor Mihaela Sin

*Nuclear Physics Department, University of Bucharest, Post Office Box MG-11, 077125 Bucharest-Magurele, Romania.*

A strong collaboration with the University of Bucharest is foreseen concerning theoretical calculations of photon induced reaction cross sections, both photoneutron reactions and photon scattering reactions above the neutron emission threshold. ELI-NP will collaborate with the University of Bucharest for finding the appropriate gamma ray strength functions and level densities parametrizations required for reaction rate estimations. For all these calculations, the statistical model code EMPIRE will be used, Prof. Mihaela Sin being one of the code's developers.

**Acknowledgments.** The authors acknowledge financial support from the Extreme Light Infrastructure Nuclear Physics (ELI-NP) Phase I project, a project co-financed by the European Union through the European Regional Development Fund. H. Utsunomiya acknowledges support from the Memorandum of Scientific Cooperation on the Implementation of the ELI-NP between IFIN-HH and Konan University. V. Varlamov acknowledges the support of the Russian Foundation for Basic Research. F. Camera thanks Oliver Wieland, Gianluca Colo, Simone Ceruti, Stefano Riboldi and Filippo Rossi for their help in the TDR definition.

#### REFERENCES

1. G.C. Baldwin, G.S. Klaiber, *Phys. Rev.* **71**, 3 (1947). And *ibid.* 73, 1156 (1948).
2. O. Wieland *et al.*, *Phys. Rev. Lett.* **97**, 012501 (2006).
3. A. Shiller, M. Thoennessen, *Atomic Data and Nuclear Data Tables* **93**, 549 (2007).
4. B.L. Bermand, S.C. Fultz, *Rev. Mod. Phys.* **47**, 3 (1975).
5. Handbook on photonuclear data for applications. Cross-sections and spectra, Final report of a coordinated research project 1996 – 1999. IAEA-TECDOC-1178, 2000.
6. V.V. Varlamov, B.S. Ishkhanov, INDC(CCP)-432 (2002).

7. V.V. Varlamov, private communications.
8. N. Paar, D. Vretenar, E. Khan, G. Colò, Rep. Prog. Phys. **70**, 691 (2007).
9. A. Carbone *et al.*, Phys. Rev. **C81**, 041301(R) (2010).
10. H. Utsunomiya *et al.*, Phys. Rev. **C81**, 035801 (2010).
11. H. Utsunomiya *et al.*, Phys. Rev. **C82**, 064610 (2010).
12. M. Arnould, S. Goriely, Phys. Rep. **384**, 1 (2003).
13. H. Utsunomiya, P. Mohr, A. Zilges, M. Rayet, Nucl. Phys. **A777**, 459 (2006).
14. R.J. Baglan, C.D. Bowman, B.L. Berman, Phys. Rev. **C3**, 2475 (1971).
15. S. Agostinelli *et al.*, Nucl. Inst. Meth. **A506**, 250 (2003).
16. S.E. Woosley, W.M. Howard, Astrophys. J. Suppl. **36**, 285 (1978).
17. M. Rayet, M. Arnould, M. Hashimoto, N. Prantzos, K. Nomoto, Astron. Astrophys. **298**, 517 (1995).
18. T. Rauscher, A. Hefer, R.D. Hoffman, S.E. Woosley, Astrophys. J. **576**, 323 (2002).
19. <http://www.tunl.duke.edu/facilities/>
20. <http://www.lasti.u-hyogo.ac.jp/NS-en/>
21. H. Utsunomiya *et al.*, Phys. Rev. **C67**, 015807 (2003).
22. H. Utsunomyia, M.S. Smith, T. Kajino, in: M. Arnould, et al. (Eds.), Tours Symposium on Nuclear Physics IV, AIP Conference Proceedings **561**, AIP, New York, 2001, p. 159.
23. S. Goko, H. Utsunomiya *et al.*, Phys. Rev. Lett. **96**, 192501 (2006).
24. K. Wisshak, F. Voss, C. Arlandi *et al.*, Phys. Rev. Lett. **87**, 251102 (2001).
25. H. Utsunomiya *et al.*, Phys. Rev. **C74**, 025806 (2006).
26. F.G.A. Quarati *et al.*, Nucl. Instr. Meth. **A683**, 46 (2012).
27. A. Giaz *et al.*, Conference record of IEEE-NSS 2014
28. J. Audouze, Astron. Astrophys. **8**, 436 (1970).
29. K.L. Hainebach, D.N. Schramm, J.B. Blake, Astrophys. J. **205**, 920 (1976).
30. S.E. Woosley, D.H. Hartmann, R.D. Homan, W.C. Haxton, Astrophys. J. **356**, 272 (1990).
31. S. Goriely, M. Arnould, I. Borzov, M. Rayet, Astron. Astrophys. **375**, L35 (2001).
32. P. Heckman *et al.*, Physics Letters **B555**, 43–48 (2003).
33. A. Tamii *et al.*, Phys. Rev. Lett. **107**, 062502 (2011).
34. D. Savran *et al.*, Phys. Rev. Lett. **97**, 172502 (2006).
35. D. Savran *et al.*, Phys. Rev. Lett. **100**, 232501 (2008).
36. C. Iwamoto, H. Utsunomiya, A. Tamii *et al.*, Phys. Rev. Lett. **108**, 262501 (2012).
37. P. Adrich *et al.*, Phys. Rev. Lett. **95**, 132501 (2005).
38. S. Goriely, Phys. Lett. **B436**, 10 (1998).
39. S. Goriely, E. Khan, M. Samyn, Nucl. Phys. **A739**, 331 (2004).
40. M. Brenna, G. Colò, P.F. Bortignon, Phys. Rev **C85**, 014305 (2012).
41. J.R. Beene *et al.*, Phys. Rev. **C41**, 920 (1990).
42. Y. Kalmykov *et al.*, Phys. Rev. Lett. **96**, 012502 (2006).
43. A. Shevchenko *et al.*, Phys. Rev. Lett. **93**, 122501 (2004).
44. V.V. Varlamov *et al.*, Atlas of Giant Dipole Resonance, INDC(NDS)-394 (1999).
45. S.S. Dietrich, B.L. Berman, Atomic Data and Nuclear Data Tables **38**, 199 (1988).
46. B. L. Berman, S. C. Fultz, Rev. Mod. Phys. **47**, 713 (1975).
47. V.V. Varlamov *et al.*, Vop. At.Nauki i Tekhn.,Ser.Yadernye Konstanty, Vol.1993, Issue.1, p.52 (1993), Russia
48. V.V. Varlamov *et al.*, INDC(CCP)-440, IAEA NDS, 37 (2004).
49. V.V. Varlamov *et al.*, Bull. Rus. Acad. Sci. Phys. **74**, 842 (2010).
50. D.M. Filipescu *et al.*, Phys. Rev. **C90**, 064616 (2014).
51. H.-T. Nyhus *et al.*, Phys. Rev. **C91**, 015808 (2015).
52. B.S. Ishkhanov *et al.*, MSU SINP Preprint 2013-1/884.
53. V.V. Varlamov *et al.*, Bull. Rus. Acad. Sci. Phys. **74**, 833 (2010).
54. A. Lepretre *et al.*, Nucl. Phys. **A219**, 39 (1974).
55. S.C. Fultz *et al.*, Phys. Rec. **186**, 1255 (1969).

56. H. Utsunomiya *et al.*, Phys. Rev. **C84**, 055805 (2011).
57. B.S. Ishkhanov *et al.*, *Are Quasimonoenergetic Annihilation Photons Really Monoenergetic Enough?*, International Conference on Nuclear Data for Science and Technology, September 26 - October 1, 2004, Santa Fe, New Mexico, USA, Abstracts, Los Alamos National Laboratory, 2004, p. 109.
58. S. Volz *et al.*, Nucl. Phys. **A779**, 1 (2006); references therein.
59. R. Schwengner *et al.*, Phys. Rev. **C78**, 064314 (2008).
60. R. Schwengner *et al.*, Phys. Rev. **C76**, 034321 (2007).
61. R.M. Laszewski, R. Alarcon, S.D. Hoblit, Phys. Rev. Lett. **59**, 431 (1987).
62. R.M. Laszewski, R. Alarcon, D.S. Dale, S.D. Hoblit, Phys. Rev. Lett. **61**, 1710 (1988).
63. N. Pietralla *et al.*, Phys. Rev. Lett. **88**, 012502 (2002).
64. T. Shizuma *et al.*, Phys. Rev. **C78**, 061303(R) (2008).
65. K. Govaert *et al.*, Phys. Rev. **C57**, 2229 (1998).
66. N. Anantaraman *et al.*, Phys. Rev. Lett. **46**, 1318 (1981).
67. F.E. Bertrand *et al.*, Phys. Lett. **103B**, 326 (1981).
68. G.M. Crawley *et al.*, Phys. Rev. **C26**, 87 (1982).
69. S.K. Nanda *et al.*, Phys. Rev. Lett. **51**, 1526 (1983).
70. C. Djalali *et al.*, Nucl. Phys. **A388**, 1 (1982).
71. C.D. Bowman, R.J. Baglan, B.L. Berman, T.W. Phillips, Phys. Rev. Lett. **25**, 1302 (1970).
72. H. Utsunomiya *et al.*, Phys. Rev. Lett. **100**, 162502 (2008).
73. U. Agvaanluvsan *et al.*, Phys. Rev. Lett. **102**, 162504 (2009).
74. D.M. Brink, Ph.D Thesis, Oxford University (1955).
75. H. Utsunomiya *et al.*, Phys. Rev. **C80**, 055806 (2009).
76. A. Avdeyenkova, S. Goriely, S. Kamedzhiev, G. Tertychny, AIP Conf. Ser. **1090**, 149 (2009).
77. J. Endres *et al.*, Phys. Rev. Lett. **105**, 212503 (2010).
78. E. Litvinova, P. Ring, V. Tselyaev, Phys. Rev. **C78**, 014312 (2008).
79. V. G. Soloviev, *Theory of Atomic Nuclei: Quasiparticles and Phonons* (Inst. of Physics, Bristol, 1992).
80. V. Derya *et al.*, Phys. Rev. Lett. **97**, 172502 (2006).
81. D. Savran, T. Aumann, A. Zilges, Prog. Par. Nucl. Phys. **70**, 210 (2013).
82. A. Tamii *et al.*, Nucl. Instr. Meth. **A605** 326–338 (2009)
83. T. Kondo, H. Utsunomiya *et al.*, Phys. Rev. **C86**, 014316 (2012).
84. \*\*\*Supplementary Web Materials.
85. J. Allison *et al.*, Geant4 developments and applications, IEEE Trans. Nucl. Sci. **53**, 270 (2006).
86. S.C. Fultz, R.L. Bramblett, J.T. Caldwell, N.A. Kerr, Phys. Rev. **127**, 1273 (1962).
87. H. Beil, R. Bergère, A. Veysseyre, Nucl. Instrum. Meth. **67**, 293 (1969).
88. L.V. East, R.B. Walton, Nucl. Instr. Meth. **72**, 161 (1969).
89. G.F. Knoll, *Radiation Detection and Measurement, Second Edition*, John Wiley & Sons (New York, 1979).p.530.
90. E. Brannon, G.L. Olde, Radiaat. Res. **16**, 1(1962).
91. H. Laurent *et al.*, Nucl. Instrum. Meth. **A326**, 517 (1993).
92. M. Cavallaro *et al.*, Nucl. Inst. Meth. **A700**, 65 (2013).
93. I. Holl, E. Lorentz, G. Mageras, IEEE Trans. Nucl. Sci. **35**(1), 105 (1988).
94. F.T. Kuchnir, F.J. Lynch, IEEE Trans. Nucl. Sci. **NS-15**(3), 107 (1968).
95. K. Nakanishi, Master thesis, RCNP, Osaka University (2003).
96. C.D. Berman *et al.*, Phys. Rev. Lett. **25**, 1302 (1970).
97. S. Amano *et al.*, Nucl. Inst. Meth. **A602**, 337 (2009).
98. H. Utsunomiya *et al.*, Phys. Rev. **63**, 018801 (2001).
99. <http://www.caen.it/csite/CaenProd.jsp?idmod=67&parent=11>.
100. A. Giaz, Nucl. Instr. Meth. **A729**, 910–921 (2013).
101. <http://www.crystals.saint-gobain.com/uploadedFiles/SG-Crystals/Documents/GlassScintillators.pdf>

- 
102. Dr. M. Igashira of the Tokyo Institute of Technology, private communications.
  103. C. Cazzaniga *et al.*, Nucl. Inst. Meth. **A778**, 20 (2015).
  104. W. H. McMaster, Polarization and the Stokes Parameters, American Jour. Phys. **22**, 351 (1954).
  105. C. Sun, Characterizations and Diagnostics of Compton Light Source. PhD thesis, Department of Physics, Duke University, 2009.